EXPLORATION OF MESOSPHERIC METAL LAYERS FROM

CHATANIKA, ALASKA

By

Cameron M. Martus

RECOMMENDED:

Nicole Mölders

Kenneth Sassen

Richard L. Collins, Advisory Committee Chair

Uma S. Bhatt
Chair, Department of Atmospheric Science

APPROVED:

Paul W. Layer
Dean, College of Natural Science and Mathematics

John C. Eichelberger
Dean of the Graduate School

8/20/2013

Date

EXPLORATION OF MESOSPHERIC METAL LAYERS FROM CHATANIKA, ALASKA

A

THESIS

Presented to the Faculty

of the University of Alaska Fairbanks

in Partial Fulfillment of the Requirements

for the Degree of

MASTER OF SCIENCE

By

Cameron M. Martus, B.S.

Fairbanks, Alaska

August 2013

Abstract

Layers of free metal atoms exist in the mesopause region of the atmosphere, generally between 80 and 100 km altitude. Resonance fluorescence lidar provides the best way to measure the structure and dynamics of these metal layers. Resonance lidar observations using tunable dye lasers are conducted at the Lidar Research Laboratory (LRL) of Poker Flat Research Range (PFRR), Chatanika, Alaska (65°N, 147°W). In this thesis, we present three fundamental aspects of mesospheric resonance lidar studies: lidar system commissioning and operation, analysis of temporal variations in the metal layers based on observations, and observations of the nickel layer. An excimer-pumped dye laser system has been used in the past for observations at LRL-PFRR, and we report on the alignment and testing of this system as well as the deployment of a new Nd:YAG-pumped dye laser system. Both of these systems are tested with observations of the sodium layer at 589 nm. Through an analysis of simultaneous observations of the sodium and iron layers taken in the past at LRL-PFRR, we study the common motion of the two layers and suggest an external forcing mechanism for the motions. We find that the motion of the layers is, in most of the observations, consistent with downward propagating gravity waves. Based on elemental abundances in meteors, the most likely source of mesospheric metal layers, we expect to find a nickel layer, yet such a layer has not been reported. We attempt to detect the layer using resonance lidar at the 337 nm nickel absorption line. We make several likely detections of the layer and present an initial estimate of the nickel profile. Signals received in the nickel measurements are as expected from a simulation based on signals received in past observations of sodium and iron.

Table of Contents

Page

Page

List of Figures

Page

Page

Page

Page

List of Tables

Page

Acknowledgements

First and foremost, I would like to thank my advisor, Richard Collins, for guiding and directing my research throughout my M.S. studies in the Department of Atmospheric Sciences (DAS). This research is ultimately a result of his initiative, and he has arranged all my support during my time in the DAS. I am thankful for all the knowledge he has imparted to me, and for all the projects in which he has allowed me to have a part. I would also extend thanks to my other committee members, Ken Sassen and Nicole Mölders, for their input to my research.

Barbara Day, the DAS administrative assistant, has been essential in navigating the administrative aspects of my studies. Many thanks to her for all her patient support and guidance. I would like to thank eLearning and Distance Education (formerly Center for Distance Education) for providing funding support for three semesters of my graduate career, and for supporting the distance class that I was able to participate in designing and teaching. I thank the National Science Foundation and the National Aeronautics and Space Administration for providing support for our lidar studies at Poker Flat Research Range (PFRR), and for the staff at PFRR for providing the facilities and support for the Lidar Research Laboratory. Thanks to the Coupling Energetics and Dynamics of Atmospheric Regions (CEDAR) for funding my attendance at the 2012 workshop in Santa Fe, NM.

I would like to thank former students in the lidar group for providing examples for me to follow, especially Agatha Light and Brita Irving. Thanks to my fellow members of the lidar group that participated in the long winter nights of observation and helped with the laser setup and maintenance: Matthew Titus, Robin Wing, and Zachary Krehlik. Special thanks to Ketsiri

Leelasakultum for helping with the distance class that we both taught and for many interesting and enjoyable conversations.

Personally, I would like to thank Tom and Kathy Murray for their help facilitating my arrival in Alaska and helping me get settled here. I thank Mike Fairchild, Denny Dougherty, Mike Albert, and Doug Duffet for their encouragement, counsel, and fellowship, as well as my many friends for making my life here in Alaska sweet. Finally and most importantly, I would like to express my gratitude towards my parents, Michael and Laura Martus, for raising me into the man I am today and for instilling in me a love for learning that has driven my studies thus far. Above all, I give all the glory, honor, and praise for my accomplishments to God, the Lord Jesus Christ, who has blessed me abundantly above measure and directed my paths through life.

1. Introduction

In the tenuous middle atmosphere (altitude ~10 – 110 km; pressure 280 – 1.0 × 10^{-4} hPa) [Brasseur and Solomon, 1986; COESA, 1966], there exists an altitude region (70-110 km) where layers of neutral metal atoms are found (see review articles by Plane [1991] and Plane et al. [1999]). Resonance fluorescence lidar (*li*ght *d*etection *a*nd *r*anging, also known as laser radar) is used to detect these elements and observe their abundances and distribution. Our research in lidar studies is based on observations conducted at the Lidar Research Laboratory (LRL) located at the Poker Flat Research Range (PFRR). PFRR is a rocket range in Chatanika, Alaska (65°N, 147°W) that is owned by the University of Alaska Fairbanks (UAF) and operated by the Geophysical Institute (GI). Observations of the polar middle atmosphere at LRL-PFRR consist of both resonance fluorescence and Rayleigh lidar measurements.

In this chapter, we introduce the atmospheric regions, relevant phenomena, and lidar techniques relevant to this study. We summarize previous lidar work at LRL-PFRR. Finally, we provide an overview of the entire thesis.

1.1. Structure of the atmosphere

The structure of the Earth's atmosphere is conventionally defined based on the vertical temperature profile as a distinctly layered structure, with several different regions or "spheres" dividing the atmosphere in altitude (Figure 1.1). The boundaries between these spheres are local maxima and minima in the temperature profile and are called "pauses." The lowest region of the atmosphere – the one in which life exists, where sensible weather occurs, and within which all topography is contained – is called the

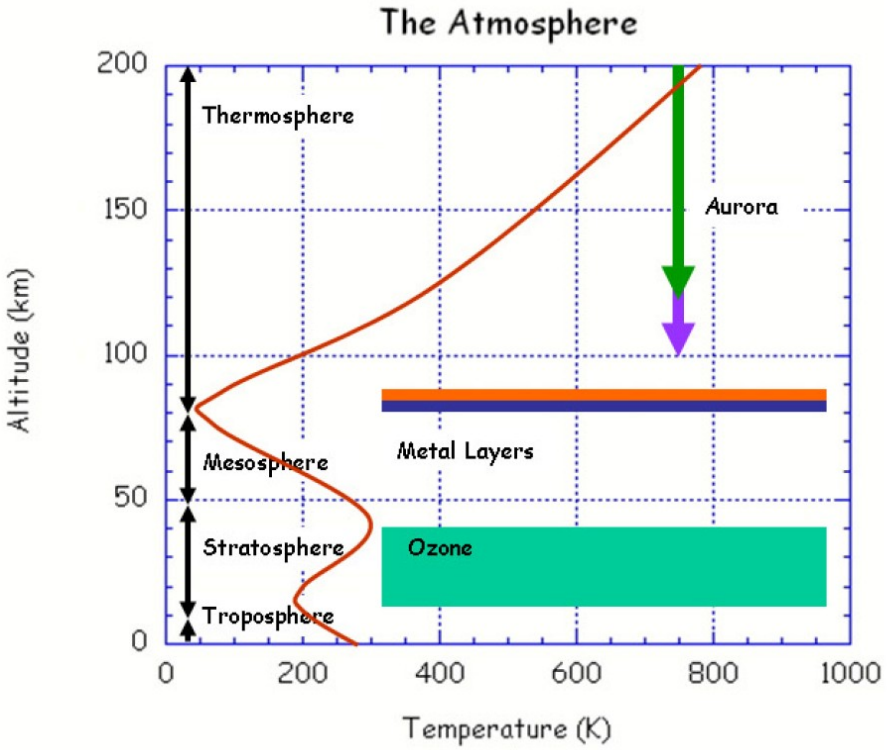

Figure 1.1 Annotated profile of atmospheric temperature with altitude showing the conventional divisions as well as several features of interest in the middle and upper atmosphere. Courtesy of COESA [1966]; Light [2009].

troposphere. This layer of the atmosphere contains 80% of all the molecules in the atmosphere, and varies in height from about 17 km in the tropics to 10 km near the poles [Wallace and Hobbs, 2006]. In the troposphere, the temperature typically decreases with altitude, as the distance from the warming influence of the sunlight-heated Earth's surface increases.

The top of the troposphere is defined by a local temperature minimum called the tropopause. Above the tropopause the temperature increases with altitude yielding a layer with a temperature inversion. This resulting layer is called the stratosphere. In the stratosphere, sunlight interacts with oxygen molecules to form the Earth's ozone layer. Ozone strongly absorbs ultraviolet radiation (UV) from the Sun and acts to prevent harmful forms of UV from reaching the surface where their high energy would damage living organisms. Absorption of this UV in the production of ozone causes the

temperature to increase with altitude in the stratosphere. The stratosphere extends to a local temperature maximum, called the stratopause, at about 50 km. Above the stratopause the temperature decreases with altitude, as the atmosphere cools radiatively with no significant source of heat.

This layer is called the mesosphere, our primary region of interest. The mesosphere extends to the mesopause, a local temperature minimum at about 80 km. The mesopause is the coolest point in Earth's atmosphere with temperatures around 180 K. In this mesopause region, several unique phenomena occur, including noctilucent clouds (NLCs) and mesospheric metal layers. NLCs (or polar mesospheric clouds) form by deposition of the miniscule amounts of water vapor that exist in the mesosphere into small ice particles during the summer, when the mesosphere is coldest (for recent research on noctilucent clouds, see the special issue of the Journal of Atmospheric and Solar-Terrestrial Physics edited by Collins et al. [2009]). Because they are too faint to be seen against a bright sunlit sky, noctilucent clouds can only be seen at night when the Sun is at the proper altitude below the horizon to illuminate the clouds but not the lower parts of the atmosphere. Also in the mesosphere are layers of free metal atoms that originate from the vaporization of meteors as they enter the Earth's atmosphere (for recent research on meteors in the atmosphere, see Murad and Williams [2002]). Mesospheric metal layers are the subject of the research presented in this thesis and are further discussed in the next section.

Above the mesopause, temperature increases with height in the thermosphere until the atmosphere becomes so tenuous that temperatures cannot be well-defined. The thermosphere consists of mostly ionized atoms and molecules due to absorption of the Sun's intense short-wavelength

radiation. Low collisional frequencies in the sparse thermosphere prevent these ions from neutralizing [Wayne, 2000].

Alternatively, the atmosphere can be described in terms of either ionization or composition. The ionized region of the atmosphere is known as the ionosphere, and found in the thermosphere and upper mesosphere [Baumjohann and Treumann, 1997]. At lower altitudes, the atmosphere consists almost entirely of neutral species. In terms of composition, the bulk of the atmosphere consists of nitrogen (78%), oxygen (21%), and 1% various other trace gases, of which carbon dioxide and argon are principle components. At altitudes up to about 105 km these gases are well mixed; this part of the atmosphere is called the homosphere. Above the homopause the atmosphere is thin enough that vertical mixing is not sufficient to maintain an constant distribution of all molecules, and the abundances decay with height according to their molecular weights. Thus the heavier elements, such as oxygen and nitrogen, become scarcer at higher altitudes than the lighter ones, such as hydrogen and helium [Brasseur and Solomon, 1986].

1.2. Mesospheric metal layers

Many rocky bodies can be found traveling through interplanetary space, ranging in size from micrometers to kilometers [Murad and Williams, 2002]. These objects, called meteoroids, occasionally intercept the Earth in its orbit and are captured by its gravitational field, causing them to fall through the atmosphere toward the surface. About 4×10^7 kg of meteoric material falls into the atmosphere every year. Meteoroids include both comet and asteroid fragments as well as cosmic dust from the solar system and interstellar space. The size of meteoroids ranges from tiny dust particles to larger particles that form the more familiar shooting stars, and finally the rare large meteorites that reach the Earth's surface. Most meteoric mass

influx consists of particles with mass 10^{-6} to 10^{-3} g and size 50 to 500 μm [Plane, 1991].

As meteoroids enter the atmosphere at supersonic speeds (> 10 km/s), the surfaces of these objects heat up to a point where they begin to ablate and glow; at this point they are called meteors [Murad and Williams, 2002]. The atmosphere becomes sufficiently dense for this heating to occur around 90 km (pressure ~1×10^{-3} hPa; COESA [1966]). The metal atoms ablated from meteors thus tend to reach their highest concentration around this altitude [Plane, 1991]. Most of the mesospheric metals are concentrated between 80-100 km; above this range the atmosphere is too tenuous to provoke sufficient heating and vaporization, and below this range the path length between molecules is short enough that free metal atoms are oxidized to form compounds.

The most common types of meteorites, chondrites, contain significant amounts of sodium (Na), iron (Fe), magnesium (Mg), calcium (Ca), nickel (Ni), and aluminum (Al) [Plane, 1991]. By mass, the fractional composition of chondrites as determined by laboratory analysis is as follows: Na, 0.6%; Fe, 11.5%; Mg, 12.5%; Ca, 1.0%; Ni, 1.5%; Al, 1.7%. Although most of these species have been detected in the mesosphere with resonance lidar, Ni and Al have not. It is one primary goal of this study to make the first detection of the mesospheric Ni layer.

In situ measurements of the mesosphere are not practical due to its density, which is too tenuous for aerodynamic flight or balloons and too dense for orbiting satellites [Abo, 2005; Chu and Papen, 2005]. The only possible way to sample the region directly is via sounding rocket. However, rockets cannot be launched frequently enough to conduct continuous measurements over a long time period or on a regular basis. Therefore, remote sensing provides the only consistent way to explore components of the mesosphere.

Resonance scattering lidar is a perfect match for mesospheric observation, since the species of interest, free metal atoms, have strong resonant transitions in the UV, visible, or IR portions of the spectrum. Furthermore, at these high altitudes the path length between atoms and molecules is long enough that collisional deexcitation does not quench the resonance scattering, as it would at lower altitudes.

The first lidar observations of a mesospheric metal layer were of Na, obtained by Bowman et al. [1969]. Although Na is not the most abundant meteoric metal, it is the most reflective target for resonance lidar due to the large scattering cross-section in the Na D line at 589 nm. Because this line is in the visible portion of the spectrum the operator can see the laser beam, making setup and operation of the lidar system straightforward. Consequently, Na has been the most extensively measured of the meteoric metals. Lidar measurements have also been made of Fe, Ca, K, and lithium (Li) [Chu and Papen, 2005; Gardner, 1989].

1.3. Resonance Lidar

Lidar is an active remote sensing method that uses a laser to send light toward a target. The resulting backscatter off the target is collected by a telescope pointed in the same direction as the laser beam. Since the backscatter is not reflected directly back toward the laser, but instead distributed over a wide angular range, the telescope only intercepts a small portion of the backscattered light. A spectral filter is used to reject all but the wavelength emitted by the laser, thus removing background light and increasing the signal-to-noise ratio. Light collected by the telescope is detected by an electronic detector, such as a photomultiplier tube (PMT). The laser beam is emitted in pulses (or shots), and the timing of the pulse emission is synchronized with the detector. Thus the time between the pulse

emission and detection indicates the altitude from which the backscatter originated. Signals below a certain altitude may be suppressed by electronically blanking the signal in the PMT for a defined time interval after the pulse. This suppression prevents saturating the detector with too much signal from the dense lower atmosphere. After detection, signals from the PMT are assimilated by a multichannel scalar (MCS) unit and sent to a computer. The data acquisition program that controls the acquisition process displays the data and saves it in a file on the computer hard drive. Lidar is similar to radar, the primary difference being the much higher frequency, or shorter wavelength, of electromagnetic radiation that is used in lidar. Although "light" typically refers to visible light, lidar systems may also operate in the ultraviolet and infrared. A sketch of the basic elements of a typical lidar system used at LRL-PFRR is shown in Figure 1.2.

The most basic type of lidar relies entirely on backscatter from the target object. In the atmosphere, where the optically thin medium allows the

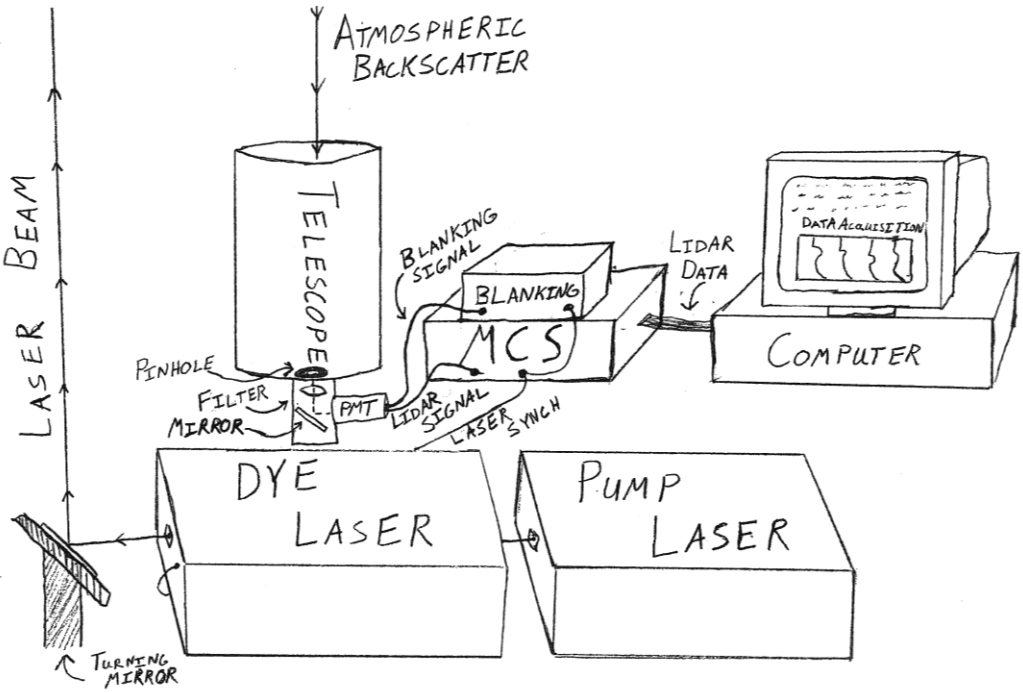

Figure 1.2 Sketch of the basic elements of our resonance lidar system at LRL-PFRR.

beam to penetrate with only a small amount of light being backscattered, targets are in the form of atoms, molecules, and/or small particles. Scattering by particles that is described by electromagnetic theory is classified as either Mie or Rayleigh scatter. Mie scattering describes scattering from particles larger than the wavelength of light, such as aerosols. Rayleigh scattering describes scattering by particles smaller than the wavelength of light, such as air molecules. Since aerosols are mostly limited to the troposphere and lower stratosphere, Mie scattering is uncommon in the middle atmosphere where our studies are focused. The Rayleigh scattered signal will be proportional to the number density of air molecules in the beam path, which scales as atmospheric pressure and thus decreases exponentially with height. However, Rayleigh lidar cannot distinguish the types of molecules or atoms and their abundances.

Resonance scatter is described in terms of the quantum mechanical interaction of photons and energy levels in atoms and molecules. Resonance florescence lidar relies on the unique absorption spectrum of each atom or molecule to target specific elements or compounds. The laser light is tuned to emit light of a specific wavelength matching that of a strong absorption line in the target. When the light hits the desired species, it is absorbed, exciting the atom to a higher, unstable energy state. However, the target rapidly decays to its ground state, reemitting a photon at the same wavelength. Other atoms and molecules besides the target are only responsive to the particular wavelength of light by Rayleigh scatter, so the resonance from the target appears as an enhanced signal in addition to the Rayleigh signal. Resonance lidar can thus be used to measure the number density of the target species.

Since resonance lidar requires that the laser light be precisely tuned to match a particular absorption line, and most lasers only emit at one

particular wavelength, one must use a tunable laser for resonance lidar studies. Tunable dye lasers are routinely used in resonance lidar systems. The dye laser requires a pumping source – usually flashlamps or another laser – to energize a small quantity of laser dye which fluoresces over a certain wavelength range. A grating is used in the laser oscillator to select which precise wavelength the emitted laser beam will be, and this beam is sent out and intensified by the amplifier. The wavelength of the laser beam can be changed within the range of the dye's capability by adjusting the tilt of the grating [Silfvast, 1996].

Figure 1.3 displays the signal from a resonance lidar operating at 589 nm. The lidar was operated by the author during the course of this study. The profile clearly shows the Na layer between 80 and 110 km. Echoes from individual laser shots are gathered by the data acquisition system into raw profiles. These raw profiles are the basic unit of the saved lidar data, with 1000 shots per profile in this case. The profiles are acquired in a sequence,

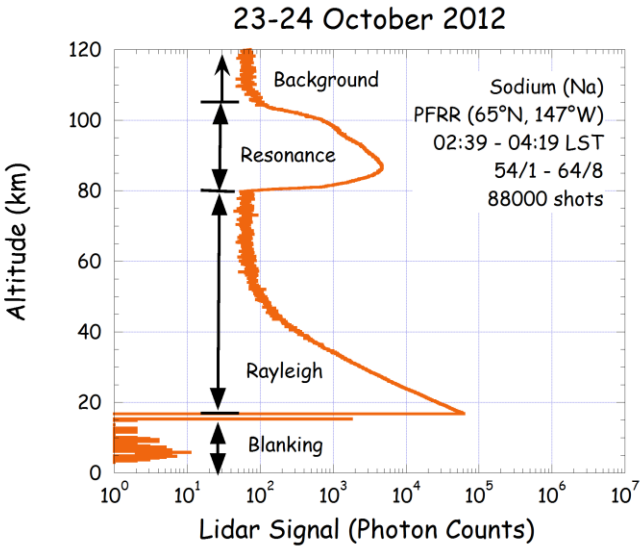

Figure 1.3 Sample Na resonance lidar profile taken at LRL-PFRR.

with eight profiles per set. Each set is then stored as an individual file. This method of making lidar measurements allows the operator to monitor the measurements in real-time and make adjustments to the lidar system at the end of a set, resuming data acquisition in the next set. The profile in Figure 1.3 is the integration of 88 raw profiles representing the sum of 88,000 laser shots taken over 1.7 h, in sets 54 to 64 on the night of 23-24 October 2012. Below 17 km, the gain of the receiver PMT is suppressed to reduce the signal and to avoid saturating the detector with high Rayleigh and Mie signals from lower altitudes, so only noise is present in this range. Above 17 km, the integrated profile consists of three parts: the Rayleigh profile, extending up to about 60 km where it fades to background levels; the resonance profile, showing the Na layer from 80 to 110 km; and the background light, including all data above the resonance profile. The shape of the Na layer is typically asymmetric, with a steep bottomside below the peak and a shallower topside above the peak.

1.4. Lidar observations at Poker Flat Research Range

Resonance lidar observations began at LRL-PFRR in 1994 with a flashlamp-pumped dye laser used for Na observations. This laser, a Candela LFDL-1 (Candela Laser Corporation, Bedford, MA), was donated to UAF by Chester Gardner at the University of Illinois where it had been used since the 1980s. This robust dye laser had been used in locations around the world for Na density measurements before being deployed in Alaska [Collins et al., 1992; Collins et al., 1993; Collins et al., 1996; Gelinas et al., 2005; Senft et al., 1989]. As a broadband laser with low tuning stability, this laser required constant monitoring and tuning during observations to ensure that the laser wavelength matched that of the Na resonance line. This laser did not possess the spectral resolution necessary to make Doppler wind and temperature

measurements, but was used solely for density measurements of the Na layer at 589 nm. Observations were taken with the Candela laser through 2003, when it was decommissioned due to catastrophic failure.

Through collaboration between the GI and the National Institute of Information and Communications Technology (NICT) in Japan, a Rayleigh lidar system was installed at LRL-PFRR in 1997. This system consists of a Continuum Powerlite 8020 solid-state Neodymium: Yttrium Aluminum Garnet (Nd:YAG) laser (Continuum Laser Corporation, Santa Clara, CA), which produces a high-energy 532 nm beam. Measurements of atmospheric density fluctuations and temperature are routinely made with this system to the present in collaboration with Kohei Mizutani of NICT [Thurairajah et al., 2010a; 2010b]. Additionally, a similar laser, the Continuum Powerlite 9030, was installed in 2005. This laser has three times the power of the 8020 and has been used to conduct measurements of noctilucent clouds in late summer 2012. Currently, it is being assessed for extending the range of current Rayleigh measurements at LRL-PFRR [Irving, 2012].

In April of 1999, an excimer-pumped dye laser was installed at LRL-PFRR for resonance lidar observations. This system, by Lambda Physik (Lambda Physik, Gottingen, Germany), consists of an LPX220i® xenon-chloride (XeCl) excimer (gas-phase) laser, which produces an ultraviolet beam at 308 nm; this beam is then channeled through a series of mirrors into the oscillator cavity of the Scanmate2® dye laser, where it energizes the dye molecules. In previous studies at LRL-PFRR, this laser has been used for observations of Na at 589 nm and Fe at 372 nm, as well as several attempts to measure other species such as molecular nitrogen ions (N_2^+) at 390 nm [Light, 2009; Su, 2007]. In 2012-2013 we measured the mesospheric Ni layer at 337 nm, after testing with Na observations.

For the lidar receiver, there are currently two reflecting telescopes at LRL-PFRR: a 24-inch (62 cm) Newtonian telescope and a 41-inch (104 cm) Cassegrain telescope. Both of these telescopes use a PMT for detection of the light. We used the 41-inch telescope for the resonance lidar observations taken during the course of this work, while we used the 24-inch telescope for concurrent Rayleigh observations with the 8020 Nd:YAG laser.

As part of this work during the summer of 2012, we installed a new resonance lidar system at LRL-PFRR, consisting of a dye laser (Continuum ND62) pumped by a Nd:YAG laser (Continuum NY81c-10). The laser was donated to the lidar program by Brenton Watkins at UAF. This new laser system is used exclusively for Na measurements at 589 nm. A major portion of this study was directed to the setup of this laser, followed by integration into an operational Na resonance lidar system, and commissioning and testing with several nights of Na observations.

1.5. Scope of this study

The research delineated in this thesis consists of three related resonance lidar studies:

1. the development and deployment of a resonance lidar system,
2. the analysis and interpretation of measurements of Na and Fe layer,
3. the design, execution, and analysis of resonance lidar measurements of the Ni layer.

In Chapter 2 we describe the alignment and testing of two different types of dye lasers at LRL-PFRR, and the subsequent observation of the Na layer, the most accessible resonance target. In chapter 3, we investigate concurrent observations of Fe and Na that were made between 2000 and 2003. We consider the use of these metal layers as a tracer for wave motions in the mesopause region. In chapter 4, we present our efforts to detect the Ni

layer with resonance lidar. To the best of our knowledge, the Ni layer has yet to be observed. However, we expect that it should be present, as Ni makes up a appreciable fraction of meteoric composition. We highlight the challenges of detecting this species in the face of low signal, and present a first estimate of the Ni profile. Finally, in Chapter 5 we summarize our discussions and present conclusions as to the implications of our work and the direction of future studies.

2. Resonance Lidar Principles and Performance

A fundamental part of lidar operations is the laser used as a transmitter. As such, much of the work in lidar studies involves laser setup, alignment, and testing. This chapter details the operation of two dye laser systems used for the resonance lidar observations presented in this thesis. But before describing the details of laser mechanics, we first give a summary of the theoretical framework for understanding lidar signals and their interaction with resonant transitions in atoms. This discussion follows previous theses by members of the GI lidar group [Breese, 2001; Light, 2009; Su, 2007], as well as the description given in Chu and Papen [2005]. In this discussion of the lidar equation, we illustrate the lidar principles using operational data from observations on the night of 23-24 October 2012, which were shown in Chapter 1. Following the outline of the laser work, we present the results of five nights of Na observations taken with the two lasers.

2.1. Lidar equation

The lidar signal can be represented by the lidar equation, which takes into account all the possible sources of photons incident on the receiver. The primary component of the lidar is the laser, which transmits the light toward the target and is thus the initial source of the photons counted by the receiver. The number of photons produced by the laser, N_L, is the ratio of the energy transmitted by the laser, E_{Laser}, to the energy of an individual laser photon, E_P:

$$N_L = E_{Laser}/E_P \tag{2.1}$$

The energy of a photon is well known from quantum physics to be:

$$E_P = h\nu_L = hc/\lambda_L \tag{2.2}$$

where ν_L and λ_L are the frequency and wavelength of the laser emission. Laser light is usually characterized by wavelength, so the latter representation is preferable. The laser emits light in discrete pulses at a particular repetition rate, so the energy of the laser can be described in terms of operative parameters by:

$$E_{Laser} = E_L R_L \Delta t \tag{2.3}$$

where E_L is the energy per pulse, R_L is the number of pulses per unit time, or repetition rate, and Δt is the time interval being considered. The total photon count released by the laser is thus denoted by:

$$N_L = \frac{E_L R_L \Delta t}{hc/\lambda_L} \tag{2.4}$$

All these photons are directed into the sky toward the target from the lidar, but many of them do not return to the lidar. The probability that individual target particles absorb and reemit the incident photon is described by a scattering cross-section, $C_{eff}(\lambda_L)$. This cross-section is unique to a particular species, and is tied to the absorption spectrum of the species, so it is highly wavelength dependant. Calculation of this parameter will be discussed in detail in the next section. Many particles will intercept the laser beam; the surface density of the target consists of the number density, $\rho(z)$, which is dependent on altitude, and the altitude range bin Δz being considered. These factors multiplied together give the fraction of photons that are intercepted and scattered by target species:

$$P_{scat} = C_{eff}(\lambda_L)\rho(z)\Delta z \tag{2.5}$$

Resonance scattering, the kind of scattering of primary interest to our studies, is isotropic – that is, scattered photons may travel in any direction. As a particle travels in any random direction, it will pass through an imaginary sphere of which the receiver surface is a small part. The scattering point becomes the center of this sphere, and the radius is the altitude of the

scattering point, z. The proportion of scattered photons that land on our detector is thus the ratio of the telescope collecting surface area (A_R) to the total surface area of the imaginary sphere:

$$P_{det} = \frac{A_R}{4\pi z^2} \tag{2.6}$$

For those photons that make it back toward the receiver, however, there is yet another loss process. The atmosphere absorbs and scatters photons as they pass through, and so atmospheric transmission, T, must be accounted for twice: once on the way up and once on the way down. Once the particles have hit the receiver, some are lost due to inefficiencies in the system. Thus we must include an efficiency factor, η, that accounts for the reflectivity of the telescope mirrors and the efficiency of the electronic detector. These final efficiency terms add a factor of ηT^2 to the mix.

Combining all the factors together, we arrive at the total number of photons that are detected from the lidar system from an altitude range Δz centered at altitude z, over a time interval Δt, here arranged in the traditional order:

$$N_s(z) = [\eta T^2]\left[\frac{E_L R_L \Delta t}{hc/\lambda_L}\right][C_{eff}(\lambda_L)\rho(z)\Delta z]\left[\frac{A_R}{4\pi z^2}\right] \tag{2.7}$$

Each term in Equation 2.7 has been put in brackets for clarity. This is the lidar equation for resonance lidar.

As discussed in Chapter 1, the lidar signal below the Na layer is dominated by Rayleigh scatter. For Rayleigh scatter, the lidar equation is slightly different than for resonance scatter. The first two terms are identical, but the scattering probabilities must be modified. Instead of the resonance scattering cross-section C_{eff} dependant on the absorption spectrum, the Rayleigh backscatter cross-section is denoted by:

$$\sigma_\pi^R = 5.45\left(\frac{550}{\lambda\,(nm)}\right)^4 10^{-32}\, m^2 sr^{-1} \tag{2.8}$$

Rayleigh scatter depends solely on wavelength so long as the particle sizes are within the Rayleigh regime – it is not dependant on the specific type of particles. Rayleigh scatter occurs in the regime when the particles are smaller than the wavelength of light but still large enough to produce scattering [e.g., Petty, 2006]. Unlike resonance scatter, Rayleigh scatter is not isotropic, so the 4π in the final term of Equation 2.7 is omitted. The lidar equation for Rayleigh lidar is given by:

$$N_R(z) = [\eta T^2]\left[\frac{E_L R_L \Delta t}{hc/\lambda_L}\right][\sigma_\pi^R(\lambda_L)\rho_R(z)\Delta z]\left[\frac{A_R}{z^2}\right] \tag{2.9}$$

where $\rho_R(z)$ is the number density of all particles producing Rayleigh scatter (basically all gas particles), not just a particular target species.

In addition to the desired lidar signal $N_{S,R}(z)$, the receiving telescope also collects background light, N_B, due to the moon, stars, aurora, and light pollution. Within the electronics of the detector system noise is invariably introduced, so this provides another term N_D. Thus the total photon count $N_{TOT}(z)$ is expressed by:

$$N_{TOT}(z) = N_{S,R}(z) + N_B + N_D \tag{2.10}$$

To obtain the actual resonance signal, therefore, one must subtract the background from the total photon counts. The background is typically found by taking the average counts N_{BACK} $(= N_B + N_D)$ in an altitude range too high to receive a lidar signal (i.e., 120-125 km). The desired signal is then calculated by:

$$N_{S,R}(z) = N_{TOT}(z) - N_{BACK} \tag{2.11}$$

The density of the target species in resonance lidar data can be calculated by taking the ratio of the lidar equation for resonance scatter at the altitude of interest to that of Rayleigh scatter in the same data at a certain fixed altitude z_R, usually 30 km. The first two terms in the lidar equation are the same between the two types of scattering, so these cancel

out. The density of Rayleigh scatterers is simply the density of air, which must be found by *in situ* measurements. Radiosondes are launched every 12 h at the Fairbanks International Airport, and this data is made available through the University of Wyoming [UW-DAS, 2013]. Assuming the ideal gas law holds, atmospheric density can be calculated using the radiosonde temperature and pressure measurements, which are taken up to 30 km.

The expression for the density of the target resonance species is then given by:

$$\rho(z) = \frac{N_{TOT}(z) - N_{BACK}}{N_{TOT}(z_R) - N_{BACK}} \frac{\sigma_\pi^R(\lambda_L)}{C_{eff}(\lambda_L)} \frac{4\pi z^2}{z_R^2} \rho_R(z_R) \qquad (2.12)$$

The effective scattering cross-section remains the final parameter left undetermined and will be discussed in the next section.

2.2. Scattering cross-sections

The scattering cross-section refers to the probability that a photon incident on a target particle is absorbed and reemitted. This probability depends on the convolution of the absorption spectrum of the target particle with the spectrum of the incident laser beam. Resonance fluorescence occurs when the energy of a photon hitting an atom (or molecule) corresponds to the energy required to excite the atom to a higher energy state. This energy is related to a particular wavelength, and thus we see this wavelength as an absorption line in the atomic absorption spectrum. After a short time, the excited atom will return to the ground state and reemit the photon. Thus the effective scattering cross-section depends not only on the strength of the absorption line, but also how much of the laser beam is directed into the absorption line. By taking resonance lidar data over a range of wavelengths across the absorption line, one can map out the shape of the line and

determine the effective cross-section. Taking the expression for the density of resonant scatterers and solving for C_{eff}, we obtain:

$$C_{eff}(\lambda_L) = \frac{N_{TOT}(z) - N_{BACK}}{N_{TOT}(z_R) - N_{BACK}} \, \sigma_\pi^R(\lambda_L) \, \frac{4\pi z^2}{z_R^2} \frac{\rho_R(z_R)}{\rho(z)} \tag{2.13}$$

Assuming the density of the resonant species $\rho(z)$ remains constant over the scanning period, one can fit the lineshape to a Gaussian curve and determine the maximum C_{eff} at the peak of the line as well as the laser linewidth from the full width of the line at half maximum.

The absorption line in the target atoms can be characterized by the absorption cross-section:

$$\sigma_{abs}(\nu) = A_{21} \frac{\lambda^2}{8\pi} \frac{g_2}{g_1} \, g_A(\nu) = \sigma_0 g_A(\nu) \tag{2.14}$$

where A_{21} is the Einstein A coefficient, the probability of the transition between energy states 1 and 2, λ is the wavelength of the photons absorbed and emitted in the transition, and $g_{2,1}$ is the degeneracy of the energy state, or number of possible ways in which the state can be filled [Chu and Papen, 2005; Verdeyen, 1981]. The line-integrated absorption cross-section, σ_0 is given by:

$$\sigma_0 = A_{21} \frac{\lambda^2}{8\pi} \frac{g_2}{g_1} \tag{2.15}$$

The absorption lineshape, $g_A(\nu)$, is defined as a probability density function in frequency that integrates to unity and has a finite linewidth.

An absorption line may be broadened by several processes. The possible range of excitation lifetime results in the Lorentzian or natural linewidth, thermal motions of the atoms cause a further broadening due to the Doppler effect, and collisions with other atoms and molecules yields even further broadening. In the mesosphere and lower thermosphere, the Doppler effect dominates the broadening, and when statistically averaged, produces a Gaussian lineshape for the absorption transition given by:

$$\sigma_{abs}(\nu) = \frac{\sigma_0}{\sqrt{2\pi}\sigma_D}\exp\left(-\frac{(\nu-\nu_0)^2}{2\sigma_D^2}\right) \tag{2.16}$$

where ν_0 is the central wavelength of the transition. The RMS width of the line is given by:

$$\sigma_D = \nu_0\sqrt{\frac{k_B T}{Mc^2}} \tag{2.17}$$

where k_B is the Boltzmann constant, T is the ambient temperature, M is the mass of the atom undergoing the transition, and c is the speed of light.

The effective scattering cross-section for resonance lidar results from the convolution of the laser line with the absorption line. Approximately a Gaussian lineshape as well, a laser emission line with rms width σ_L can be represented by:

$$g_L(\nu) = \frac{1}{\sqrt{2\pi}\sigma_L}\exp\left(-\frac{(\nu-\nu_L)^2}{2\sigma_L^2}\right) \tag{2.18}$$

Integrating the laser line and the absorption line together as follows, we obtain an expression for the effective scattering cross-section as a function of laser wavelength:

$$C_{eff}(\nu_L) = \int_{-\infty}^{\infty}\sigma_{abs}(\nu)g_L(\nu)d\nu$$

$$C_{eff}(\nu_L) = \frac{\sigma_0}{\sqrt{2\pi}\sigma_{eff}}\exp\left(-\frac{(\nu_0-\nu_L)^2}{2\sigma_{eff}^2}\right) \tag{2.19}$$

where the rms width of the effective lineshape is given by:

$$\sigma_{eff} = \sqrt{\sigma_D^2+\sigma_L^2} \tag{2.20}$$

This expression for C_{eff} quantifies the strength of the resonance scatter of laser light with finite linewidth by a resonance absorption line of finite bandwidth. For an atom with hyperfine structure, such as Na, the scatter occurs due to several closely spaced absorption lines. In this case of n

hyperfine lines the effective cross-section is the summation of the individual cross-sections and calculated as follows:

$$C_{eff}(\nu_L) = \sum_{i=1}^{n} S_i \frac{\sigma_{0i}}{\sqrt{2\pi}\sigma_{effi}} \exp\left(-\frac{(\nu_{0i} - \nu_L)^2}{2\sigma_{effi}^2}\right) \quad (2.21)$$

where the rms width of the ith line is:

$$\sigma_{effi} = \sqrt{\sigma_{Di}^2 + \sigma_L^2} \quad (2.22)$$

and the relative strength of each hyperfine line is given by:

$$S_i = A_i / A_{21} \quad (2.23)$$

2.2.1. Sodium (Na)

An alkali metal with atomic number 11, Na is an element with a relatively low abundance in the upper atmosphere, and makes up a small part of meteoric composition, 0.6% by mass [Plane, 1991]. However, due to its large Einstein A coefficient and high absorptivity (Table 2.1), Na is the easiest atom to observe with resonance florescence lidar. Na has also been observed regularly in the past with the resonance lidar system at LRL-PFRR.

Na has only one valence electron, and as such its atomic spectrum can be represented mathematically without much complication. The ground-state orbital configuration of the electrons is $1s^2 2s^2 2p^6 3s^1$. The transitions of interest, together called Na D, occur as a transition of the valence electron from the $3p^1$ excited state to the $3s^1$ ground state (Figure 2.1). Due to coupling between the electron's spin and orbital angular momentum in the excited state, the transition between these two states is split into a fine structure with two possibilities: transition from 3p $^2P_{3/2}$ to 3s $^2S_{1/2}$ (D_2), or 3p $^2P_{1/2}$ to 3s $^2S_{1/2}$ (D_1) [Chu and Papen, 2005]. These transitions are the well-known D_1 and D_2 Fraunhofer lines, and in air are located close together at 589.6 nm and 589.0 nm, respectively, in air [NIST, 2012]. Further splitting

into a hyperfine structure is caused by the interaction of these possibilities with the nuclear angular momentum of the Na atom of 3/2; thus the ground state is split into two hyperfine states and the two excited states are split into 4 hyperfine for the $^2P_{3/2}$ and 2 hyperfine for the $^2P_{1/2}$. The fine structure produces the two lines, D_1 and D_2, which are about 6 Å (or 0.6 nm) apart. The hyperfine structure in the D_2 line can be accurately approximated by two lines referred to as D_{2a} and D_{2b}. Thus, the effective cross-section for resonance lidar on the Na D_2 line is given as:

$$C_{eff}(\nu_L) = \frac{\sigma_0}{\sqrt{2\pi}\sigma_{eff}}\left[S_a\, exp\left(-\frac{(\nu_a-\nu_L)^2}{2\sigma_{eff}^2}\right) + S_b\, exp\left(-\frac{(\nu_b-\nu_L)^2}{2\sigma_{eff}^2}\right)\right] \qquad (2.24)$$

with a single rms width σ_{eff} for both hyperfine lines.

Tabulated values of λ, A_{21}, g_2, and g_1 are given in the NIST Atomic Spectra Database [NIST, 2012] and are listed in Table 2.1 for the D_2 line of Na.

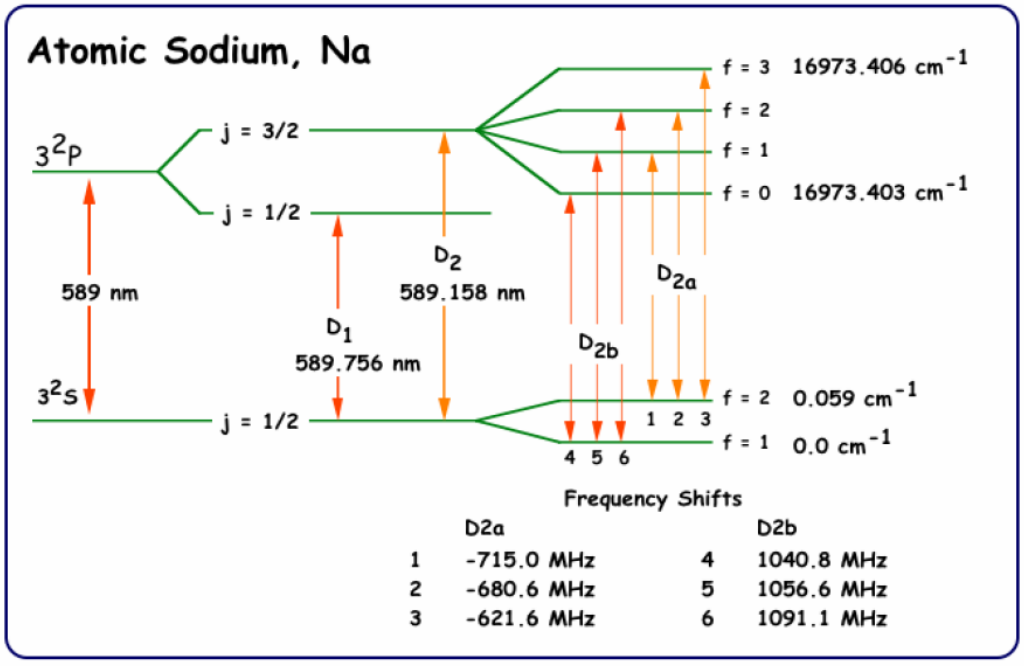

Figure 2.1 Energy levels involved in the Na D transitions. Courtesy of Su [2007].

Table 2.1 Absorption line parameters for Na and Fe

Line	λ (nm) (Air)	A_{21} (10^7 s^{-1})	g_2	g_1	σ_0 (10^{-7} m^2 Hz)
Na 589 nm (D2)	588.995	6.16	2	4	17.01
Fe 372 nm	371.993	1.62	9	11	1.09

2.2.2. Iron (Fe)

As discussed in Chapter 1, the common transition metal, Fe, with atomic number 26, is one of the most abundant metals in meteorites and therefore makes a fairly dense layer in the mesosphere. The ground state electron configuration of Fe is $1s^2 2s^2 2p^6 3s^2 3p^6 3d^6 4s^2$. Since Fe has more than one valence electron, its transition spectrum is much too complicated for analytical calculations; its transitions are best quantified by experiment in the laboratory [NIST, 2012]. Its best transition for resonance florescence lidar occurs in the UV at 372.0 nm, due to a relatively large Einstein A coefficient and low absorption by the Earth's stratospheric ozone layer. Increasingly strong absorption of UV light by ozone prevents measurement of mesospheric metals at shorter wavelengths. In the 372 nm transition, electron configuration levels go from $3d^6(^5D)4s4p(^3P°)$ to $3d^6 4s^2$. The effective cross-section for the 372 nm Fe line is simpler than for Na D_2 line because the Fe line has no hyperfine structure and can be represented as a single Gaussian line. The effective scattering cross-section is about a factor of 15 weaker than the D_2 line in Na (Table 2.1). However, its abundance (by number density) is generally about 2 to 4 times higher than Na, so the mesospheric Fe layer is not significantly more difficult to measure than the Na layer.

2.3. Lasers for resonance lidar

A laser (Light Amplification by Stimulated Emission of Radiation) is a device that produces a powerful, highly collimated, polarized, monochromatic beam of light. These properties make lasers useful for many applications, particularly for remote sensing. Because the beam has very low divergence (~1 mrad), it can be projected over vast distances. For atmospheric lidar, the monochromatic properties of lasers allow their use in laser spectroscopy of gases whose absorption-scattering properties depend strongly on wavelength. This property is particularly important in resonance lidar where the incident beam must precisely match the wavelength of an absorption line [Fujii and Fukuchi, 2005; Weitkamp, 2005].

The basic elements of a laser are a gain medium (the material within which lasing occurs) and an energy source for the gain medium [Silfvast, 1996]. These elements are housed inside a cavity with a mirror on one side and a partially transmissive mirror (or reflective window) on the other. The gain material is chosen particularly for the availability of an upper-level energy state that can be excited by pumping the medium with an energy source, such as an electrical pulse or a light source. As the excited state undergoes radiative decay back to a lower energy level, it emits a photon with an energy equal to the difference in energy between the two states. This form of unstimulated radiative decay is known as spontaneous emission, because it occurs spontaneously without any outside perturbation. Such emission is the same type that occurs in most light-producing processes, such as florescent bulbs. However, spontaneous emission has a broad spectrum and is emitted in all directions. The purpose of a laser is to concentrate all this light into one collimated beam of a single frequency.

Light emitted in the path between the two end mirrors is reflected back-and-forth through the gain medium. As they pass through the medium,

these photons have the same energy as the energy difference between the state being excited by pumping and the lower level state in the desired transition; recall that these photons were emitted from such a transition. Some of these photons will strike excited molecules and induce them to decay to the lower state before the decay occurs spontaneously. When this occurs, the emitted photon has the same energy and travels in the same direction as the original photon. This process is known as stimulated emission, and continues to occur as the emitted light travels back-and-forth between the mirrors in the cavity, amplifying the emitted light at the desired wavelength and in the desired direction. Some of the oscillating light is lost from the system through the partially reflective window at the front of the cavity, allowing the laser beam to exit the cavity. Amplification in the oscillator cavity will continue to occur until the amount of light in the exiting beam and the amount of light produced in the gain medium are in equilibrium. This cavity is known as an oscillator, since the light oscillates back and forth through the cavity, being amplified in the gain medium.

In order to produce lasing, the pumping must be sufficient to cause more of the molecules in the gain medium to be in the upper level state than in the lower state. This condition is called a population inversion, because the population distribution of molecules by energy state is usually such that most of the molecules are in the ground state, with a few excited here and there. A population inversion allows many transitions to occur at once, those photons colliding with other excited molecules as they exit the material, triggering a chain reaction of stimulated emission that continues to grow as the oscillation progresses.

Lasers used in lidar systems usually include a second stage, called an amplifier, that contains the same gain medium as the oscillator. As in the oscillator, the gain medium is pumped. Once pumped, the medium is

stimulated by the oscillator beam which is steered through the amplifier. Stimulated emission in the amplifier gain medium amplifies the oscillator beam during its single pass by orders of magnitude. A laser may contain several amplifiers if required.

The gain medium of a laser may be in any of the three states of matter: solid, liquid, or gas. Each type has its particular advantages and disadvantages. At LRL-PFRR, we have lasers of each type, and all three are used in the research presented in this thesis. Resonance lidar relies heavily on liquid-state dye lasers, because these lasers are tunable in their output wavelength. Both of the resonance lidar systems used in this research incorporate dye lasers. These two dye lasers are passive systems that require pumping by another laser beam. In our first resonance system, used for prior research and the primary system for this research, the dye laser is pumped by a gas-phase xenon chloride (XeCl) excimer laser. A new resonance system, installed and tested as part of this research, consists of a dye laser pumped by an Nd:YAG solid state laser. The Nd:YAG laser, more commonly called a Nd:YAG laser, uses the synthetic gemstone neodymium yttrium aluminum garnet, a pink ruby, as its lasing medium. Both of these systems are discussed in detail in the following sections.

2.4. Excimer-pumped dye laser system

The original resonance lidar system at LRL-PFRR consists of a Lambda Physik Scanmate2® dye layer pumped by a Lambda Physik LPX200i® XeCl excimer laser. An excimer (for *exc*ited di*mer*) is a compound of two atoms that can undergo lasing transitions. The excimer molecule serving as the gain medium in this laser is xenon chloride (XeCl). Xenon is a noble gas with a full shell of valance electrons, and as such is normally inert and does not react with other elements. However, when the atoms xenon and

chloride are excited, they may bond together to form XeCl and find a stable excited state. Of course, this excited state decays quite rapidly, and since the atoms are highly repulsive in the ground state, the molecule breaks apart. This leads to a natural population inversion, where there are more individuals of a species in an excited state than in the ground state, as in this case there are no ground state XeCl molecules; thus excimer lasers are an efficient way to produce a laser beam. The excimer laser operates by producing a high voltage discharge, which can be set at 18, 20, or 22 kV, in a gaseous mixture that contains small concentrations of xenon (Xe) and chlorine (Cl_2) in nitrogen (N_2) as a buffer gas. The high voltage excites Xe and Cl and allows formation of the excimer. In this gas-phase laser, the beam only makes a single pass each way through the cavity, so the cavity is quite long – about one meter. The XeCl excimer laser produces a beam at 308 nm, deep in the ultraviolet, allowing for uses that require UV light.

The ultraviolet beam from the excimer laser provides a pumping source for the dye laser, which produces the actual lidar beam at the desired wavelength for resonance (Figure 2.2). A dye laser uses a fluorescent dye compound dissolved in a transparent solvent as the lasing medium. The dye solution is pumped through a cuvette positioned in the excimer laser beam, so that the dye molecules are excited by the pump beam and fluoresce spontaneously over a wavelength range depending on the type of dye; different dyes can be substituted to obtain different wavelength ranges in the output beam. In the oscillator cavity, the light from the cuvette is directed into a diffraction grating where one wavelength is selected and directed back into the cuvette, causing stimulated emission at the selected wavelength. The wavelength is selected by adjusting the tilt of the grating, which is accomplished by a computer-controlled stepping motor. The highly precise motor and grating allows a minimum step in wavelength of less than a tenth

of a picometer. After the oscillator beam emerges from the oscillator cavity, it passes again through the oscillator cuvette and is amplified in what is termed a preamplifier. Thus, the oscillator cuvette in this specific dye laser supports both oscillation and preamplification. The beam is then passed through a second cuvette, the amplifier, which is also pumped by the excimer beam. The oscillator beam is aligned to strike the same point in the cuvette as the excimer beam, thus causing the emission in the amplifier to occur at the selected wavelength. When taking resonance observations, the laser is tuned to the desired absorption line in the spectrum of the target species, causing florescence. The excimer laser beam can pump dyes to emit only at wavelengths longer than that of the pump beam, in this case 308 nm; thus it is possible to produce a dye beam in the UV with this laser system. In the past, this system has been used to observe Na at 589 nm and Fe at 372 nm.

At the start of our project, this laser system had not been used for several years, so we needed to align it and test its performance before beginning our attempt to detect nickel (Ni) at 337 nm. Being in the visible range at 589 nm, it is possible to see the laser beam for Na during alignment procedures, making the process easier. Therefore, we began our project by aligning the laser on the dye used for Na, then taking some Na data to ensure

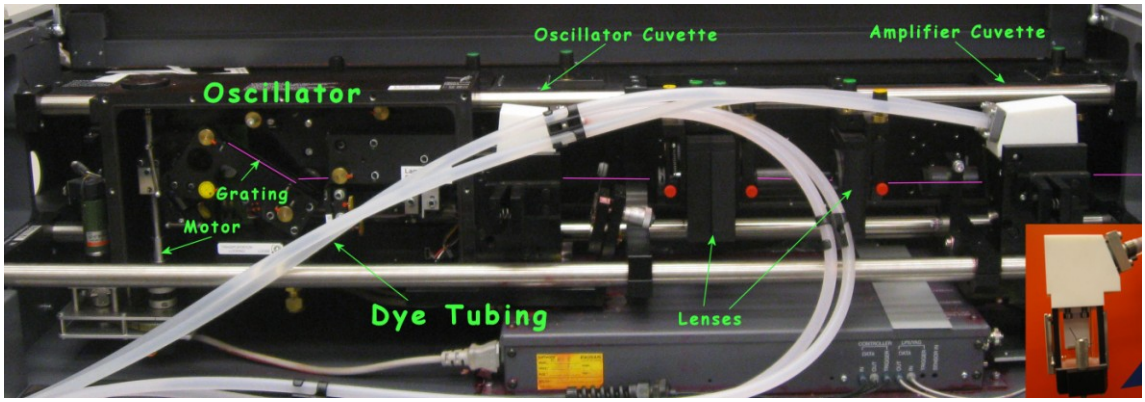

Figure 2.2 Excimer-pumped dye laser cavity. Inset shows the oscillator cuvette.

that the system operated as expected. To observe Na, we use Rhodamine 590 dye, which has a peak efficiency of 16% at 581 nm, and a range from 569-608 nm [Brackmann, 1997]. This dye is highly fluorescent and the most frequently used laser dye. It also happens to fluoresce at the wavelength of the 589 nm Na line, making it ideal for our studies. Rhodamine dissolves in methanol, a readily available solvent.

After initial alignment of the laser, we measured the spectrum of the laser light at various grating settings (Figure 2.3). The short, broad hump present in each curve is the (undesired) spontaneous emission, while the tall peaks are the (desired) stimulated emission. The effective wavelength range of this laser and dye is from 570 to 605 nm. Outside of this range, the grating setting does not effectively influence the dye florescence, and only spontaneous emission is produced (i.e., 560 nm, 565 nm, and 610 nm). A strong line of stimulated emission with minimal spontaneous emission is produced at 590 nm, very close to the wavelength of the Na line. The strong lines in this spectrum (i.e., 575 nm - 595 nm) saturate the detector. This saturation occurred because the spectrum was acquired at a light level high enough to allow detection of the weaker spontaneous and stimulated emissions. It is important note that while the amplitude of the spontaneous emission is smaller than that of the stimulated emission, the total power integrated over the entire spectral emission can be greater for the spontaneous emission than the weaker laser lines (i.e., 570 nm, 600 nm, and 605 nm).

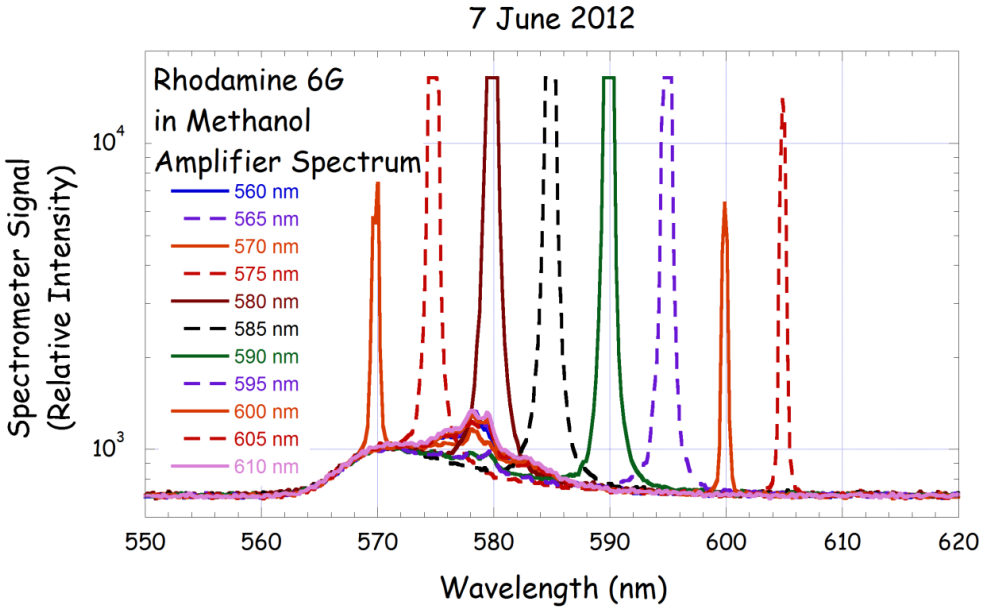

Figure 2.3 Spectra of the excimer-pumped dye laser beam with Rhodamine 6G dye at various grating settings from 560 to 610 nm.

2.5. Nd:YAG-pumped dye laser system

As discussed in Chapter 1, in the summer of 2012, our lidar group received a Nd:YAG-pumped dye laser from Brenton Watkins at UAF. This laser had been used for Na resonance lidar but had been unused for several years at the time we received it. Therefore, this system required setup, cleaning, and alignment before it could be operated. The dye laser, a Continuum ND62, operates similar to our existing excimer-pumped dye laser; a pump beam is directed into the dye cuvette, causing fluorescence, and the wavelength is selected by a grating in the oscillator (Figure 2.4). Two more cuvettes, a preamplifier and an amplifier, increase the lasing at the selected wavelength to produce the laser beam. The pump beam is provided by a Continuum NY81c-10 Nd:YAG solid-state laser, which produces a beam at 1064 nm that is frequency doubled to produce a 532 nm green beam. Nd:YAG lasers are also used for Rayleigh lidar observations at LRL-PFRR, so

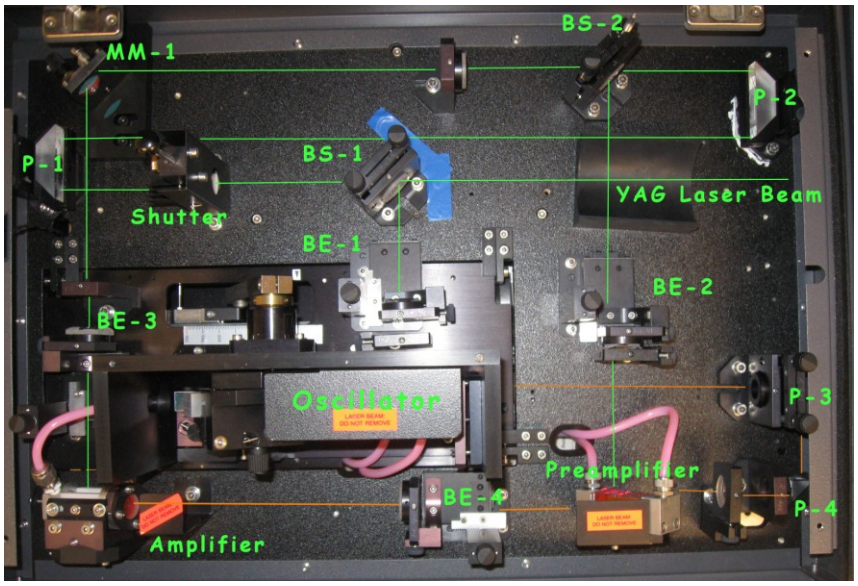

Figure 2.4 Nd:YAG-pumped dye laser cavity. MM refers to a turning mirror, P refers to a turning prism, BE refers to a beam expander, and BS refers to a beam-splitting mirror.

members of the GI lidar group have experience with their operation and maintenance.

The Nd:YAG laser operates by sending a high-voltage discharge through a flashlamp to create a light pulse [Silfvast, 1996]. These flashlamps pump the Nd:YAG rod (cylindrically shaped crystal) and populate the upper-level state of the lasing transition. A peculiarity of sold-state lasers is that the time it takes for the light in the oscillator to reach equilibrium is substantially shorter than the time for the upper-level state in the laser rod material to fully populate from pumping [Silfvast, 1996]. Thus the upper-level state is never fully filled and the lasing is not as powerful as possible based on the laser gain medium. This can be solved by reducing the oscillator Q-factor, or quality factor – basically a measure of how much emission is lost from the cavity – while pumping occurs. The cavity is thus left open, and the emitted light escapes rather than being directed back into the oscillator to excite transitions. Less transitions from the upper-level state occur during this time, allowing the upper-level state to be filled to its maximum value. At

this point, the cavity is closed and all the transitions are excited at once, producing one massive pulse. The cavity is then opened and the upper-level state is allowed to fill again, and the process is repeated. This process is called Q-switching, and is the means by which the Nd:YAG laser produces high energy pulse (~1 J).

In our Nd:YAG laser, the Q-switching is accomplished by means of an optical switch that affects the transmission of the light to the rear mirror of the oscillator. This switch is made up of a polarizer, a 1/4 wave plate, and a Pockels cell. A Pockels cell contains special birefringent crystals that change their index of refraction when an electric field is applied, rotating the polarization of the light when the field is switched on differently than when it is off. As the light passes toward the rear mirror, the 1/4 wave plate rotates the polarization of the light, and the Pockels cell causes a farther rotation depending on whether the electric field is applied. If the polarization of the light returning from the rear mirror toward the oscillator is in a different plane than that of the polarizing element, the light will not pass through to re-enter the oscillator head, and the Q-switch is said to be closed. The Q-switch is open when the Pockels cell does not effectively change the polarization of the light, and the light can freely pass from the oscillator head to the rear mirror and back.

Once the infrared laser beam leaves the oscillator it is directed into the amplifier, where lasing is again induced in a second Nd:YAG rod, amplifying the oscillator beam during a single pass. The IR beam from the amplifier is passed through a frequency doubling crystal called a second harmonic generator (SHG) to produce the 532 nm green beam. There are several adjustable factors within the laser which must be set properly for the laser to function at peak capacity. First, the optics must all be aligned so that the beam follows a straight path through the elements and no light is lost.

Second, the polarizing elements, such as those located in the Q-switch, must be set to the proper angle. Third, the timing of the flashlamps firing relative to the Q-switch opening must be optimized to allow the upper-level state of the lasing transition to fully populate.

The majority of work involved in the setup of this new Na lidar was in establishing the operation of the Nd:YAG laser. Before the laser could be operated, the coolant system had to be functional. The water that cools the laser head in this design is kept in a small reservoir tank and circulated past the laser head, where it gains heat, then on to a heat exchanger, where it dumps its heat to the chilling water. The chiller water is circulated from the heat exchanger to a chilling unit; these two water systems are kept separate. To avoid conducting any electrical current as it passes by the laser head, the circulating water must be deionized, since voltage discharges of several thousand volts occur in flashlamps that produce lasing in the Nd:YAG rods. Conduction could cause the rods to crack, destroying the laser. The circulating water passes through a deionizing filter to keep it deionized, and an indicator light warns if the resistivity of the water is above the safe limit for operation. Since the laser had not been operated for some time, and our experience has shown that these lasers fail with cracking of the laser rods if the coolant system does not operate correctly, we cleaned the circulation system before attempting to operate the laser. We flushed the circulation system with a hydrogen peroxide solution, installed a new deionizing filter, and flushed with fresh deionized water several times. After cleaning we let the circulator run for more than a day to satisfactorily deionize the water through the filter.

With the coolant system working properly, we then turned to the electro-optic operation of the Nd:YAG laser. Before firing we replaced the flashlamps, which degrade with operation and can be damaged in transit.

Initially we had difficulties with interlocks, including a failing temperature sensor on the amplifier and a cover switch wired backwards. Once we replaced the sensor and ensured that all interlock switches were properly in place, we were able to fire the laser. Power measured during the first operation of the laser was 0.2 W at 532 nm (henceforth known as green power). To produce maximum green power, the SHG crystal must be precisely aligned; the mount for the SHG is equipped with a motor enabling fine rotation, so this may be done easily. Every time the laser is operated, the SHG must be finely rotated to produce maximum power. All powers quoted in this discussion are measured after tweaking the SHG to optimum performance.

Although the laser was operational, the power measured was not sufficient to pump the dye laser, and was significantly less than what it should have been. Notes from John Pender, the first owner of the laser, written in the operator's manual show measurements taken in 1993, when the maximum power was 659 mJ per pulse, or 6.59 W for the 10 Hz laser. Thus, inefficiencies in the system – misalignment or improper settings – were causing a significant loss of power during operation.

The first system parameter we began to check was the alignment of the beam path between the various optical elements. Figure 2.5 shows the layout of the laser optical bench, with all the elements labeled that are relevant to the following discussion. We began with the rear mirror of the oscillator (MM-1), adjusting it to ensure that the oscillator beam followed a straight path through the oscillator rod. We then adjusted the beam path into the amplifier rod using two turning mirrors MM-3 and MM-4, in that order. The alignment of the beam through the amplifier rod was done with the amplifier capacitor bank disconnected, so that only the oscillator was firing and emission from the amplifier would not obscure the oscillator beam. We

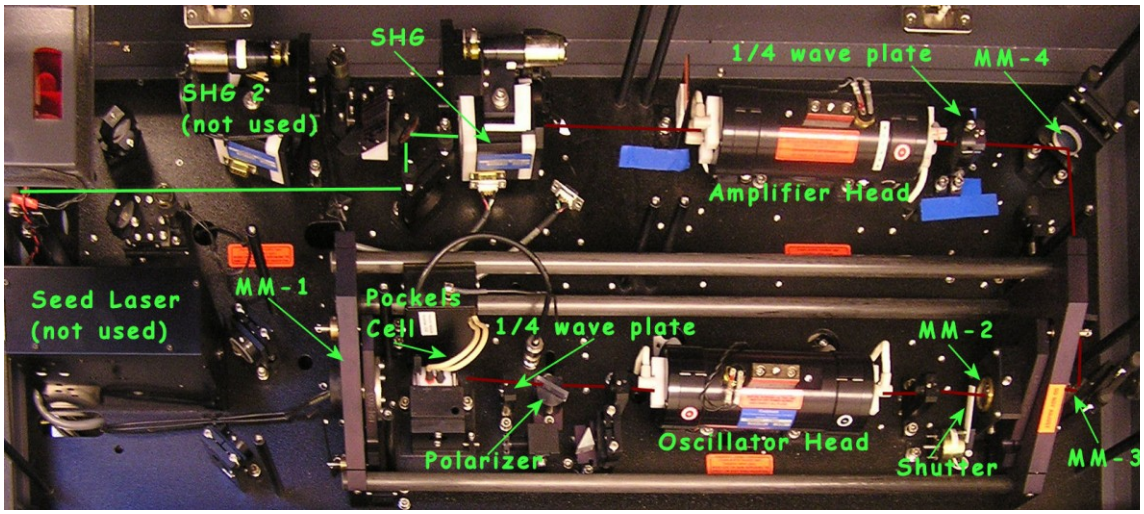

Figure 2.5 Nd:YAG laser cavity.

had to make several passes through the system, but when we eventually finished, we measured the basic laser power out of the amplifier at 1064 nm (IR power) to be 7 W. The green power was once again 0.2 W; not improved a bit.

Although the green power was lower than expected, the IR power was not too much lower than expected, and we supposed that the SHG was at fault for the conversion. The SHG model was designed to convert 30% of the incoming IR beam into green light, so we should expect to measure about 2 W of green power at this time. A spare SHG was provided with the laser by the previous owner, so we changed the SHG but found that the power dropped by a factor of 10. We attempted another SHG of the same model that we had in an old laser, but this showed no improvement over the first, and was a little less efficient. While tweaking the position of the SHG, we found that the mount was too high – that the maximum conversion could not be obtained with the SHG screwed into its proper position, but could be achieved with the screw loose allowing the SHG to be positioned slightly lower. We used spacers

to rigidly position the SHG in this lower position. In addition, we also tweaked the rotation of a 1/4 wave plate positioned just before the amplifier. These changes produced a slight increase in power, the green measuring 0.3 W – still far less than acceptable for operation of the lidar system.

Thus as far as we could determine, the SHG was working properly and the laser was aligned; the only possibility that remained for the poor performance was in the operation of the oscillator or in the laser heads. Based on advice from a laser technician, we suspected deterioration of the cladding around the rods in the laser heads, but this would be very expensive to rebuild. As a last resort, we decided to check for free-running in the oscillator. Free-running occurs when the Q-switch does not effectively block all the light and the oscillator lases when the Q-switch is closed [Continuum, 1991]. A poor-quality laser beam will then be formed and the power will be much less than designed, since the upper-level state does not become fully populated before lasing occurs. In our laser, the most common means of free-running is when the 1/4 wave plate and the Pockels cell are misaligned in their rotations, causing the linearly polarized element before the oscillator to receive circularly polarized light. Instead of blocking the light as expected, the polarizer then allows some light to leak through into the oscillator, causing lasing at a lesser efficiency by depopulating the upper level before it is filled.

We followed the procedures in the laser operator's manual to check for free-running. The beam was blocked after exiting the oscillator, and the light scattered at this block from the flashlamps firing was measured with a photodiode. Signal from the photodiode was displayed on an oscilloscope that was triggered off the capacitor bank in the laser. Q-switching was not activated, so the laser was not firing, and only flashlamp light should be seen. The flashlamp signal ideally appears as a very smooth curve rising from zero

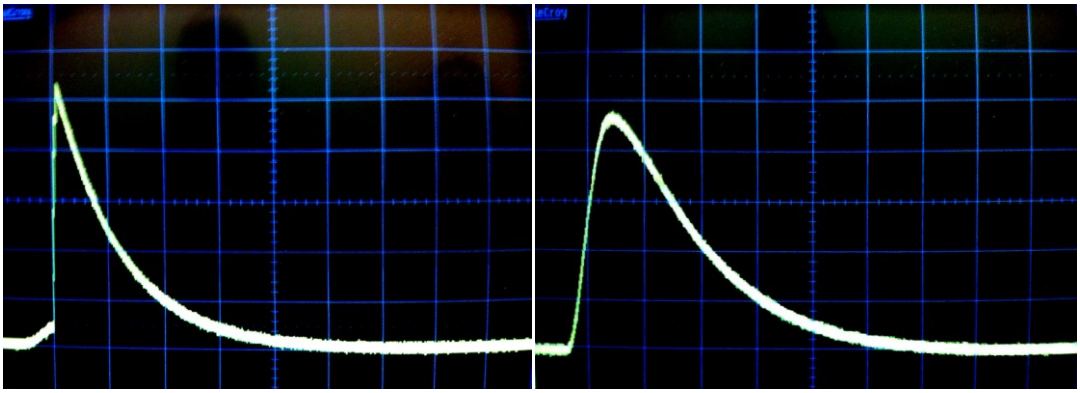

Figure 2.6 Oscilloscope display of signal from the Q-switch when free-running (left) and with free-running eliminated (right). The scales on the display are 0.2 ms in the horizontal, and in the vertical, 500 mV (left) and 50 mV (right).

to a broad maximum, then decreasing to zero again. When the shutter blocking the laser beam path out of the oscillator was opened, a sharp, jagged peak arose out of the flashlamp curve and dominated the signal; this was clear evidence of free-running (Figure 2.6). Tweaking the rotation of the 1/4 wave plate in the oscillator quickly eliminated the free-running signal. With this adjustment made, the laser, when fired, immediately produced a green power of 2.5 W, which was sufficient for our purposes. To ensure that free-running was entirely eliminated, as the manual directed we repeated the process of monitoring the flashlamp signal at a high voltage level of 1.55 kV, 100 V above the normal operating level of 1.45 kV. With free-running eliminated at the higher level, this would provide a buffer to ensure that no free-running would occur during operation.

Since we modified the position of elements in the oscillator, we tweaked the alignment of the beam path again to ensure it had not been changed. We also found that with the free-running eliminated, the repositioning of the SHG was no longer necessary. With the laser properly aligned, we measured the IR power to be 8.3 W and the green power to be

2.8 W. We deemed this power to be acceptable for operation. We ran the laser for over an hour to ensure its stability; no issues were detected.

With the Nd:YAG laser finally working properly, we were then ready to attach it as a pump beam into the dye laser. The Nd:YAG laser and the dye laser were designed to attach snuggly together so that the Nd:YAG pump beam goes directly into the proper path in the dye laser. The dye laser is entirely passive; the Nd:YAG pump beam provides all the energy for lasing, and the only electrical power needed is for the motor that moves the grating, allowing the selected dye wavelength to be changed. To optimize the dye laser, the only procedure necessary was to align the beam path using the various mirrors and lenses that direct the beam into the proper dye cuvettes. In this dye laser, there are three cuvettes: one in the oscillator, one as a preamplifier, and one as an amplifier. The Nd:YAG beam must be distorted horizontally by a set of cylindrical lenses in front of each cuvette, and both the beam shape and position must be optimized for maximum power. After going through the alignment procedure several times, we obtained what we determined to be the maximum power, 0.28 W.

For our dye in this laser, we used Rhodamine 610 with methanol as the solvent, which is specified to have a peak efficiency of 29% at 594 nm [Brackmann, 1997]. Its effective range is specified to be from 584-619 nm when pumped with an Nd:YAG 2nd harmonic as in our system. After alignment of the dye laser, we found a dye power of 0.28 W at a grating setting of 594 nm, for a pump beam power of 2.8 W. Spectra taken across the range of the dye show a well-defined, narrow lineshape, with little spontaneous emission present, indicating good performance (Figure 2.7).

Comparing the performance of this laser to the excimer-pumped dye laser as used for Na observations, we find that the Nd:YAG-pumped laser produces a much higher power beam. For the Na observations taken on 23

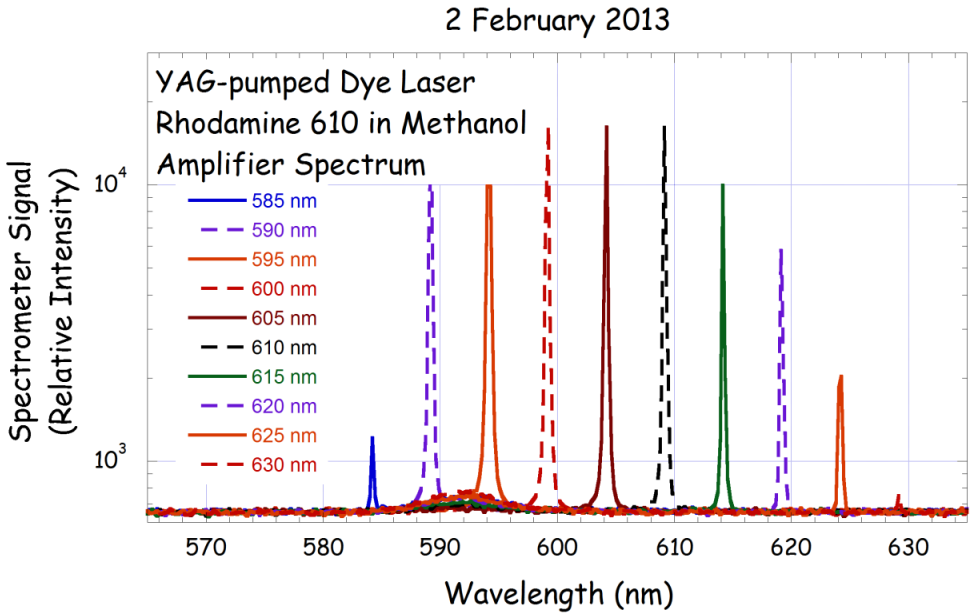

Figure 2.7 Spectra of the Nd:YAG-pumped dye laser beam with Rhodamine 610 dye at various grating settings from 585 to 630 nm.

October 2012, the excimer-pumped laser output 0.03 W of power. Taking the ratio of this with the power output of the Nd:YAG-pumped laser, we find that the Nd:YAG-pumped laser produces a factor of 9.3 more power than the excimer-pumped laser. This gain in power translates to an increase in the signal received per unit time from the Na layer, allowing us to process Na density measurements from the data at a much higher time resolution than with the previous data, and enabling the observation of atmospheric processes at higher spatial and/or temporal resolution.

2.6. Lidar operations

Lidar signals from our dye lasers are received with a 104 cm Cassegrain telescope, first used for observations in October 2008. A filter centered on the desired wavelength with a very narrow bandwidth (0.8 Å for observations at 589 nm) is used to reduce background light. Light is detected

by a photomultiplier tube (PMT) that is synchronized to the firing of the laser. Because of very high levels of Mie scatter from aerosols and ice crystals in the troposphere and lower stratosphere, the first 150 μs of the returning signal (corresponding to about 20 km) is electronically blanked in the PMT so as to avoid saturating the detector and causing pulse pileup, corrupting the signal [Irving, 2012]. After detection, signals are sent via a multichannel scalar (MCS) unit to the control computer, where the data acquisition is displayed and monitored by the operator, and the data is recorded and saved. For mesospheric lidar, signals are so low that the PMT counts individual photons rather than measuring intensity. Because of the reflectivity of the Na layer, we may get up to an average of 20 photon counts per laser shot returned to the detector; however, for the Rayleigh lidar, which operates at much higher power, a very clear night will yield 1 count per shot. Therefore, it is necessary to integrate the photon counts over many laser shots to obtain a statistically significant signal. Our dye lasers for resonance lidar operate at either 10 or 15 Hz, and we generally integrate on the order of 1000 shots in the MCS unit to form a profile, which is then collected by the computer's data acquisition program. We group a certain number (typically 8 or 16) of profiles taken at the same settings into a set. Between sets, the operator may make changes to the data acquisition or to the lidar system if necessary.

2.7. Wavelength alignment

Since the Na line is only a few picometers wide, it is reasonable to expect that the grating calibration is not so precise so as to land exactly on the line by dialing the exact laboratory wavelength [Peshave, 2004]. In addition, the grating setting of a resonance line may drift by 10's of picometers due to thermal effects. Resonance occurs due to the collision of an atom with a photon carrying the same energy as a transition between states

in the atom, causing the atom to absorb the photon and change states. A photon's energy is directly related to its frequency by Planck's constant, and frequency is related to wavelength by the speed of light. Changes in the speed of light, caused by thermal effects in the laser cavity changing the index of refraction of air, can cause differences in the laser wavelength that corresponds to the specific wavelength of the transition. In past Na measurements with this laser, the grating setting to intersect the D_2 line has varied over a range of about 50 pm, and has been as much as 60 pm longer than the measured air wavelength (Figure 2.8).

We find the position of the D_1 and D_2 lines relative to the position of the laser line by using a spectrometer into which was fed light from both a Na lamp and from the laser. The signal from the spectrometer is displayed in an oscilloscope (Figure 2.9). With the Na line in sight from the Na lamp emission, we can adjust the grating setting in the dye laser to tune the laser wavelength until it matches the position of the Na line in the spectrometer.

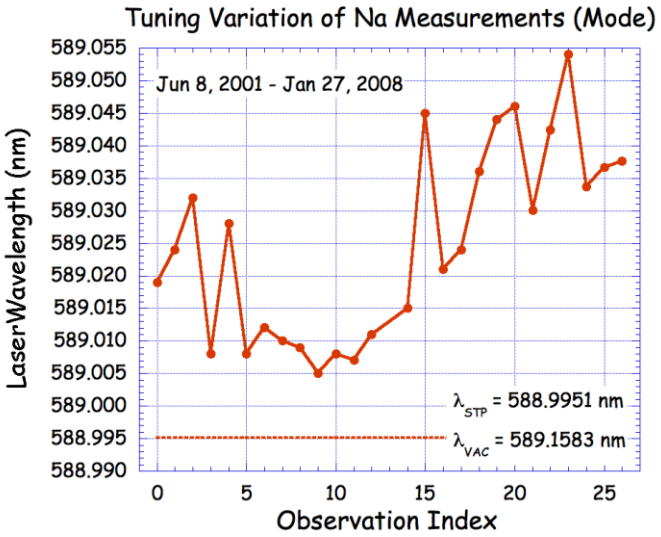

Figure 2.8 Grating settings on the excimer-pumped dye laser when tuned to the Na D_2 line for Na observations on different nights.

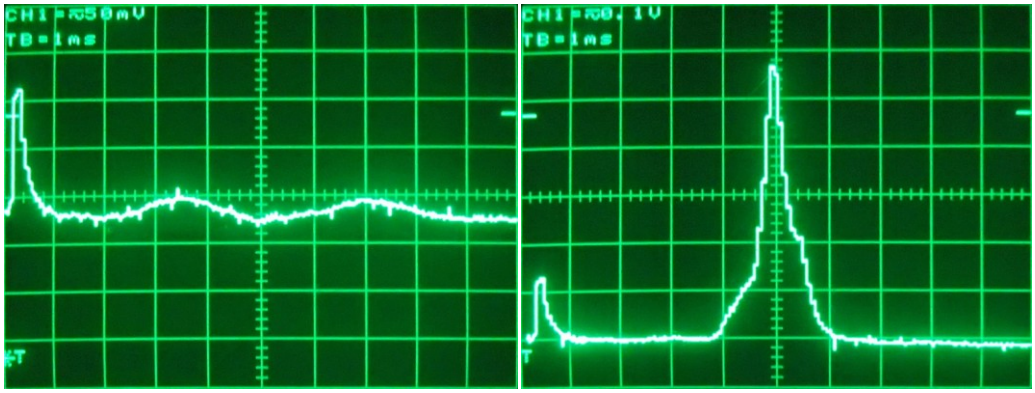

Figure 2.9 Spectra of Na emission and the dye laser beam through a high-resolution spectrometer. Na D_2 and D_1 lines from an Na lamp (left); the laser line through the same spectrometer when centered on the D_2 line (previously aligned with the center line on the oscilloscope display). The display scale in the horizontal is 1 ms on both plots and in the vertical is 50 mV (left) and 100 mV (right).

To do so, we set the D_2 line on the center line of the oscilloscope, then move the laser line until it is centered at the same point (Figure 2.9, right).

To tune the laser precisely to the Na line, we use a Na hollow cathode tube (HCT) as a reference. The HCT consists of a tube of Na vapor that is excited and caused to glow. The light from the HCT is observed by a detector and output to give a signal on an oscilloscope. By feeding the laser light into the HCT with a fiber optic cable, Na atoms will absorb the light and a larger population of atoms will be excited. The HCT becomes more conductive when the laser light is at the Na absorption wavelength, giving a larger current through the HCT and hence a larger signal on the oscilloscope. The grating control software allows for scanning through a range of wavelengths, and we thus can find the optimum wavelength when resonance is achieved and the HCT signal increases. We scan the grating over about a 20 pm range and watch the HCT signal displayed on the oscilloscope rise to a maximum (Figure 2.10). This wavelength, corresponding to the HCT maximum, becomes our initial observation wavelength. Just to ensure that we are

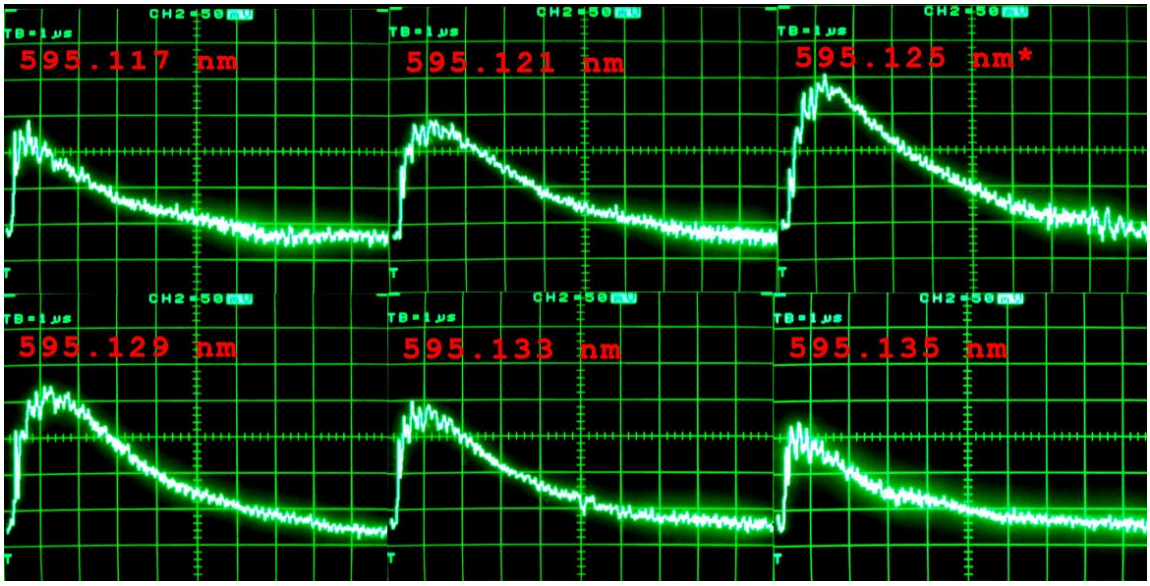

Figure 2.10 Na HCT response at various grating settings on the Nd:YAG-pumped dye laser. Peak response at 595.125 nm (upper right). The display scale in all plots is 1 μs in the horizontal and 0.1 V in the vertical.

receiving maximum signal from the Na layer, we scan the grating over several picometers once the beam is in the sky before taking data. Nevertheless, this technique gets us quite close to the line. As an example, before taking Na observations on 23 October 2012, we found using the HCT that resonance on the D_2 line was obtained at a grating setting of 589.032 nm on the excimer-pumped dye laser; by comparison, the standard air wavelength of the D_2 line is 588.995 nm, 37 pm of difference.

2.8. Na observations

A total of five nights of Na observations were taken as part of this research during the 2012-2013 observing season at LRL-PFRR (Table 2.2). The first two nights were taken in Fall 2012 with the excimer-pumped dye laser as a test of the system before using it to begin the search for Ni. After the Ni search was concluded, we took three nights of data with the Nd:YAG-pumped dye laser to test its performance. Table 2.3 summarizes the observed

Table 2.2 Na observations in this study

Date	Time (LST)	Sets	Power	Pump Laser
23-24 Oct. 2012	19:40 - 03:43	64	30 mW	Excimer
1-2 Nov. 2012	20:40 - 01:46	50	60 mW	Excimer
19 Feb. 2013	01:49 - 07:09	38	0.26 W	Nd:YAG
12-13 Mar. 2013	22:10 - 05:34	58	0.26 W	Nd:YAG
16 Mar. 2013	00:05 - 05:11	47	N/A	Nd:YAG

Table 2.3 Na layer parameters from observations in this study

	23-24 October 2012	1-2 November 2012	19 February 2013	12-13 March 2013	16 March 2013
Column Abundance (10^9 cm^{-2})	9.5	9.2	4.0	2.9	2.9
Peak (km)	86.7	88.8	88.9	92.1	89.3
Centroid Height (km)	90.1	89.2	88.7	91.7	89.2
RMS Width (km)	5.0	4.5	4.7	5.2	5.6
Peak Density (10^3 cm^{-3})	8.2	8.3	3.3	2.2	2.1
Bottomside RMS Width (km)	2.5	4.1	4.6	5.3	5.5
Topside RMS Width (km)	6.9	4.8	4.8	5.0	5.7

physical characteristics of the Na layer on these five nights. The observed layer parameters are consistent with the seasonal variations seen in past observations at LRL-PFRR, as discussed in Chapter 3. In this section, we present the data taken during these nights as it relates to the performance of the lidar system.

2.8.1. 23-24 October 2012

As the fall observing season set in, we began our observational testing of the existing resonance lidar system with a night of observations of Na. By

varying the wavelength of the laser in a small range around the peak response, one can determine the C_{eff} for each wavelength. The linewidth can then be determined by plotting these values. On the night of October 23-24, 2012, we began our observations with an excimer pump laser energy of 405 mJ per pulse at 20 kV. We operated the laser at 10 Hz for observations, resulting in an average excimer laser power of 4 W. The dye laser yielded an average power of 0.03 W, thus giving a pumping efficiency of 0.8% – much less than expected for Rhodamine 6G dye, 16% at 581 nm [Brackmann, 1997].

On our first night of observations, we made two linewidth scans. The first was taken in profiles 9/1 through 25/4, over a wavelength range decreasing from 589.0393 nm to 589.0288 nm in steps of 0.6-0.7 pm. Wavelength changes in our linewidth scans are made between sets, so that each set represents one wavelength. Figure 2.11 shows the average profiles from several different sets in the linewidth scan, demonstrating how the

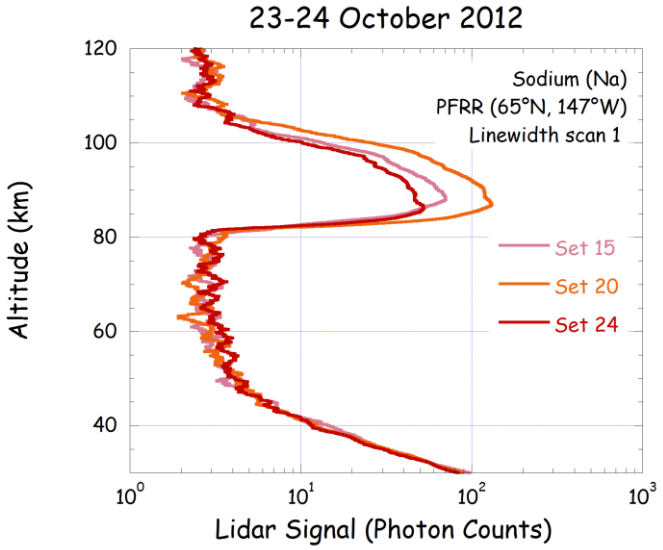

Figure 2.11 Average profiles for several sets in the first linewidth scan on 23-24 October 2012. The wavelengths of the sets are as follows: set 15, 589.0353 nm, set 20, 589.0324 nm (peak of the line), and set 24, 589.0296 nm.

response from the Na layer decreases as the laser wavelength is tuned away from the resonance line. However, the Rayleigh signal does not change, as it is not dependant on an absorption spectrum. C_{eff} for each of these sets was calculated based on Equation 2.13. The results are plotted in Figure 2.12, along with a fit to determine the peak C_{eff} and calculate the linewidth from Equations 2.24 and 2.22. The maximum value of C_{eff} was found to be 3.6×10^{-16} m^2. For the purposes of this calculation, sets with resonance signal less than 10% of the maximum value were discarded, due to excessive noise at low signal levels that may skew the results away from the true lineshape. The full width at half maximum (FWHM) linewidth was found to be 4.4 pm.

After this first scan, we changed the dye in the laser to ensure that we were getting the maximum lasing efficiency. Our second scan included profiles 36/1 to 53/4, covering the range from 589.0373 nm to 589.0267 nm in steps of 0.6-0.7 pm. Using the same methods as for the first scan, the maximum C_{eff} was found to be 3.5×10^{-16} m^2 and the FWHM linewidth was 4.5 pm, very similar to the first measurement.

The total integrated photon count profile for the data taken at a fixed wavelength of 589.0324 nm, the peak of the lineshape, is shown in Figure 2.13. This data was taken in sets 54 through 64 and is a continuous measurement for 1.67 h. The maximum resonance signal occurred at 86.9 km, with the layer spanning from 80 to 104 km. A visualization of the Na layer over time as a false color plot is shown in Figure 2.14. To produce the densities for this plot, the photon counts were integrated over 60 minutes to form a sliding window that was moved in steps of 15 minutes; this method allows more statistical confidence in the densities but recovers some of the time resolution lost by the long integration time. Unfortunately, the time over which continuous data was taken is fairly short, due to our observation time being broken up by the two linewidth scans. Thus, the amount of time

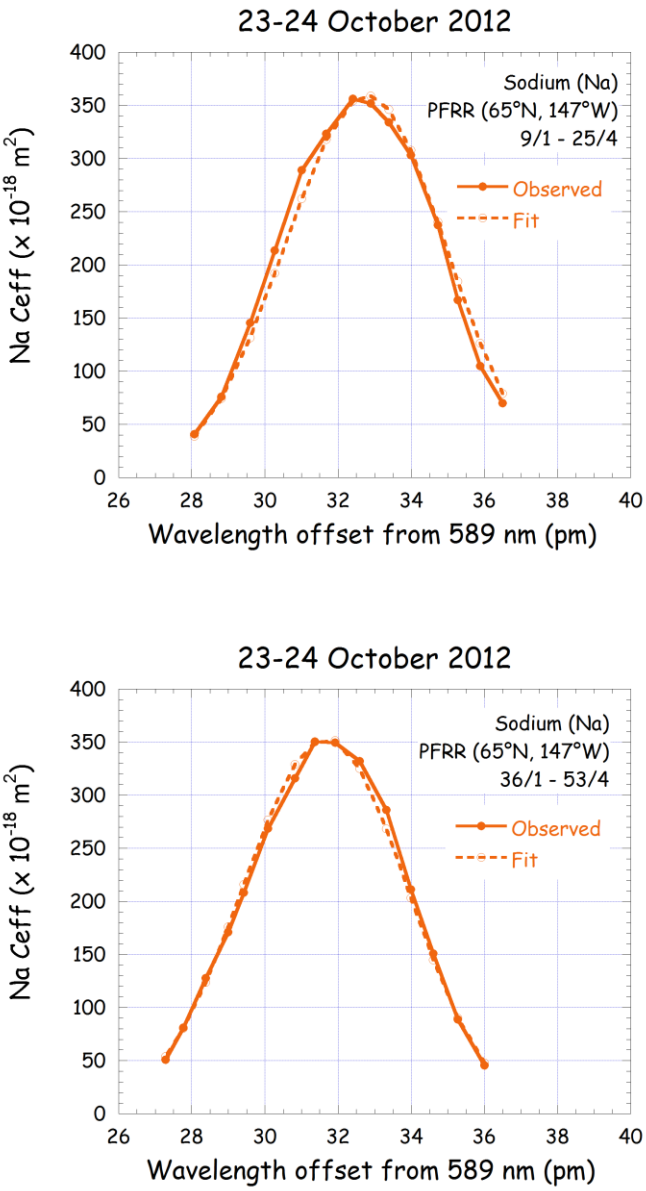

Figure 2.12 Na linewidth scans on 23-24 October 2012.

for this observation is not large compared to the resolution, so little change is seen in the layer over time, although there is a slight decrease in the peak density. Vertically, the layer looks quite smooth, with a single peak throughout the night.

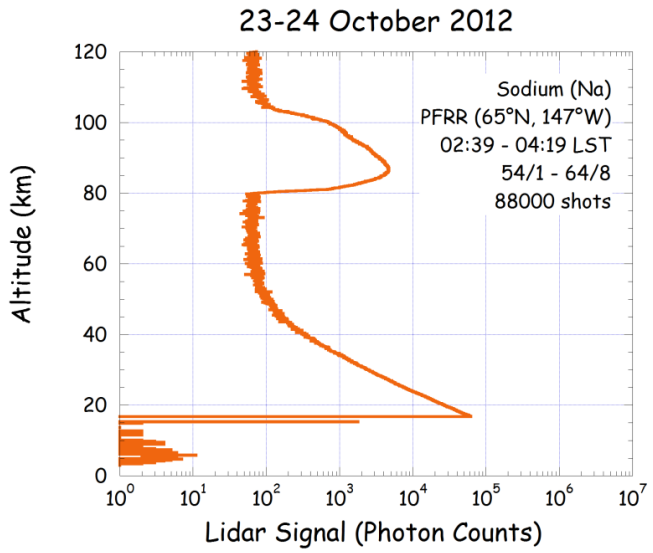

Figure 2.13 Average profile from Na observations on 23-24 October 2012.

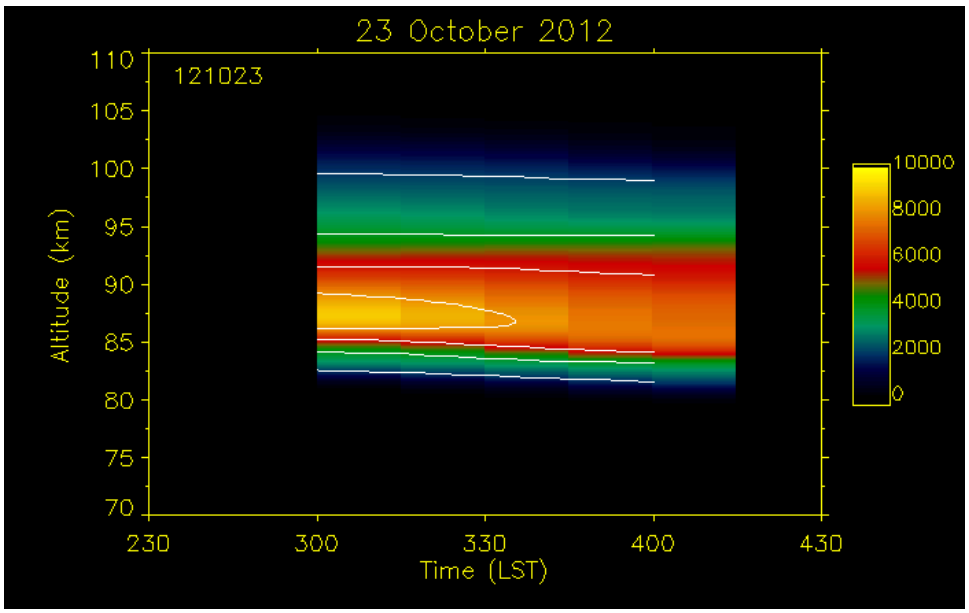

Figure 2.14 False color Na density plot from the night of 23-24 October 2012. Times are in hours on the morning of 24 October.

2.8.2. Alignment after first observations

Before taking a second night of observations, we revisited the alignment of the laser to optimize its performance. The dye laser was, in fact, not receiving the full power of the excimer beam. Spectra of the laser beam at several wavelengths throughout the dye range are shown in Figure 2.15. Note that for the wavelength nearest the Na line, 590 nm, the spontaneous emission is much smaller compared to the stimulated emission of the laser line than in spectra taken from a previous alignment.

2.8.3. 1-2 November 2012

After realignment, we took a second night of Na observations on November 1-2, 2012 to farther confirm the performance of the laser. We ran the excimer at 15 Hz, with an energy of 450 mJ per pulse at 20 kV. The data

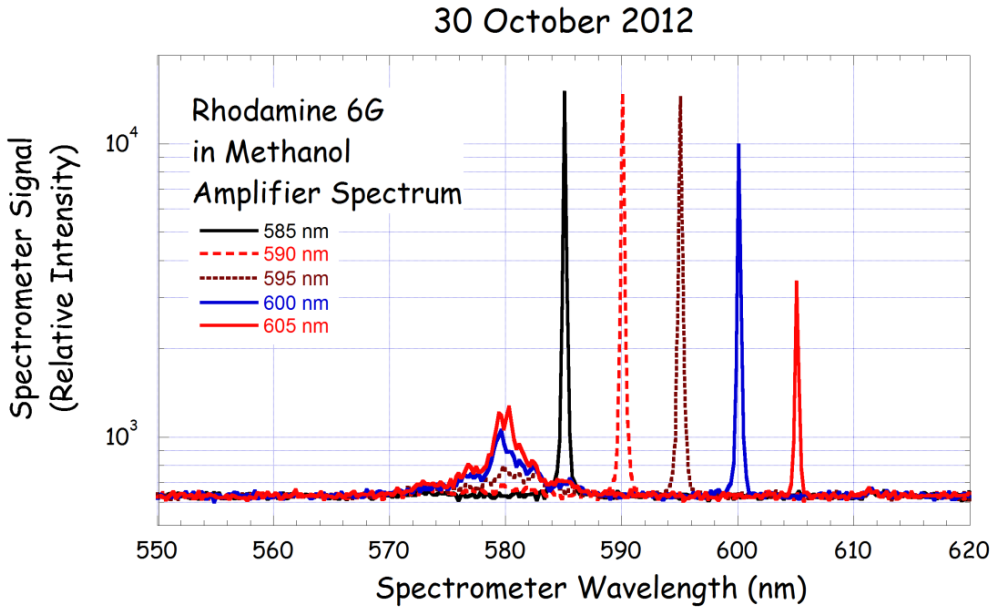

Figure 2.15 Spectra of the excimer-pumped dye laser beam with Rhodamine 6G dye at various grating settings from 585 to 605 nm after realignment.

started at a different wavelength from the previous night, at 589.0412 nm. We made a linewidth scan in profiles 11/1 through 28/4 from 589.0441 nm to 589.0326 nm (Figure 2.16). The effective linewidth was much broader than in the previous night at 8.5 pm, with an effective cross-section of 2.1×10^{-16} m^2. Only signals greater than 10% of the maximum were used for this calculation. The remainder of the data was taken at 589.0408 nm with the exception of sets 32-35 which were taken at 589.0403 nm; the integrated profile is shown in Figure 2.17. It is unclear why the linewidth was larger, indicating less optimum conditions, during this night. Sky conditions could be at fault, or perhaps the new alignment did not help the performance but rather degraded it.

A false color plot of the densities from data used in the integrated profile is shown in Figure 2.18. On this night, continuous data was taken for over 2.5 h, which is still not long enough to see significant variations in the layer given our resolution. However, some d and broadening of the layer can be seen over time.

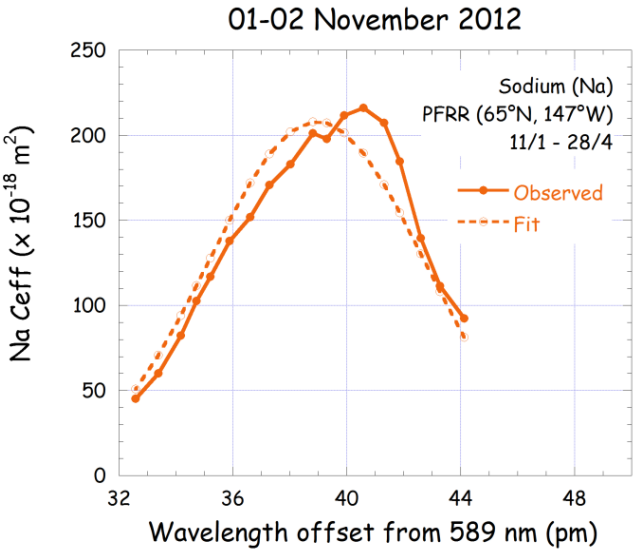

Figure 2.16 Na linewidth scan on 1-2 November 2012.

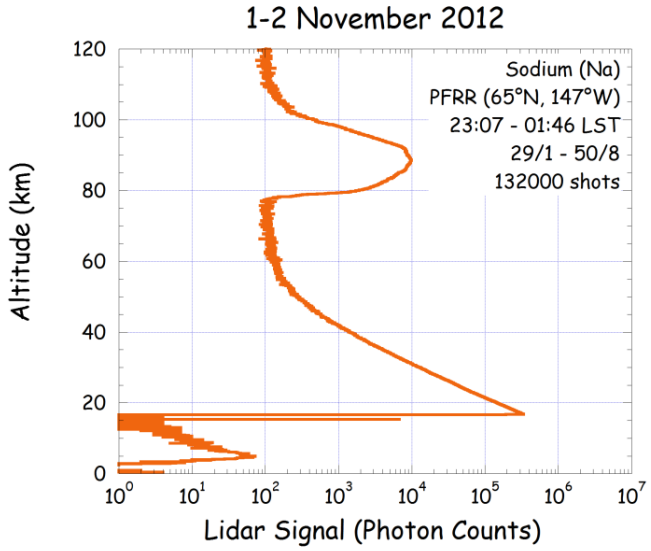

Figure 2.17 Average Na profile from observations on 1-2 November 2012.

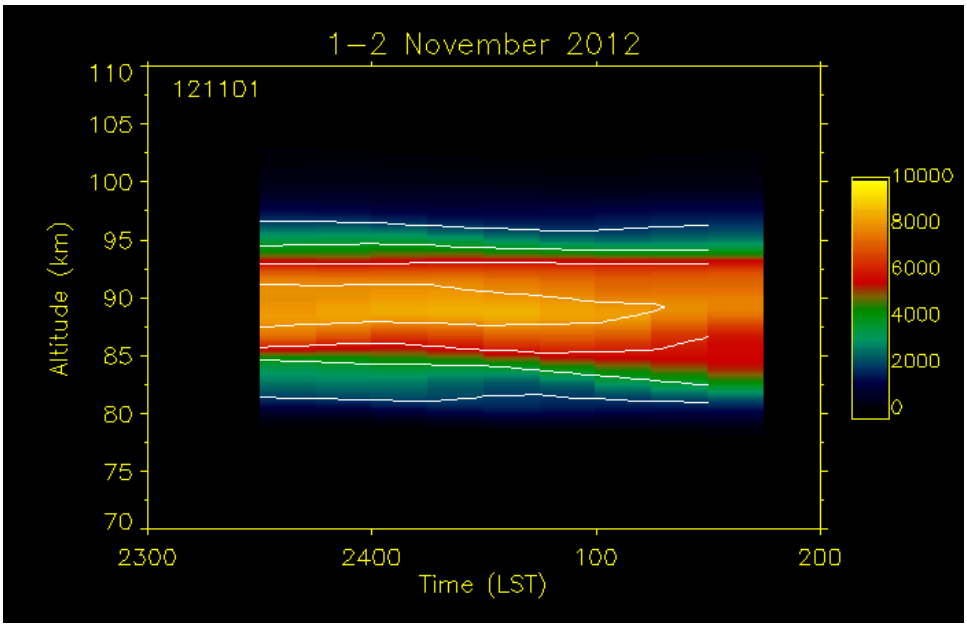

Figure 2.18 False color Na density plot from the night of 1-2 November 2012.

2.8.4. 19 February 2013

On the night of 19 February 2013, we took the first observations with the new Nd:YAG-pumped dye laser. Wavelength calibration with the HCT found the Na line to be near 593.5 nm on the grating setting in the dye laser; this is over 4 nm off from the catalogued air wavelength of 589.0 nm. Apparently the grating in this laser is not manufactured to the same precision as the excimer-pumped laser, and we have calibration issues. Later experimentation found that the grating motor can move accurately in small steps of a picometer, which is necessary for fine-tuning to the peak of the line and performing a linewidth scan, but larger steps of several nanometers upset the calibration significantly. Therefore, during subsequent observations we had to find the line with the HCT and then only make small adjustments to the wavelength setting so as to keep the calibration.

Initial data taken on this night started after midnight on the morning of 19 February and gave signals of up to 21 counts per shot, fluctuating down to around 15 counts per shot at times due to variations in the Na layer. We took a linewidth scan to assess the performance of the new laser in profiles 7 – 20 (Figure 2.19). The result gives an effective linewidth of 6.3 pm with a C_{eff} of 2.7×10^{-16} m^2. Signals greater than 25% of the maximum signal were used in the lineshape fit, as this threshold gave the best fit. This linewidth is in between the range of measurements of C_{eff} taken with the excimer-pumped laser earlier in this observing season.

After the linewidth scan, we took about two hours of data at the peak of the Na line, which at that time occurred at 593.486 nm on the grating. The integrated profile of this data, sets 22-38, is shown in Figure 2.20.

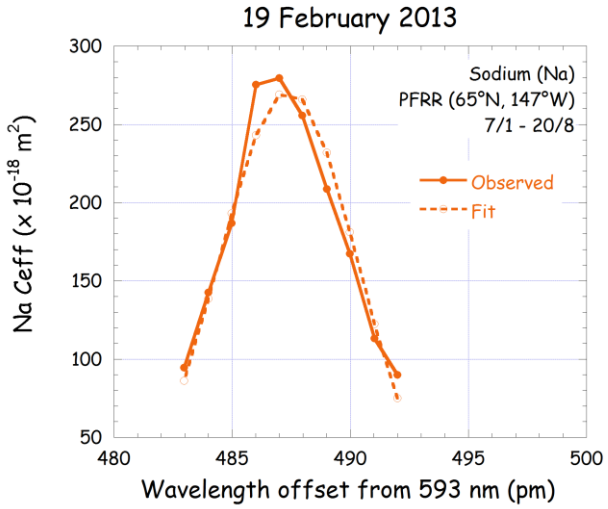

Figure 2.19 Na linewidth scan on 19 February 2013.

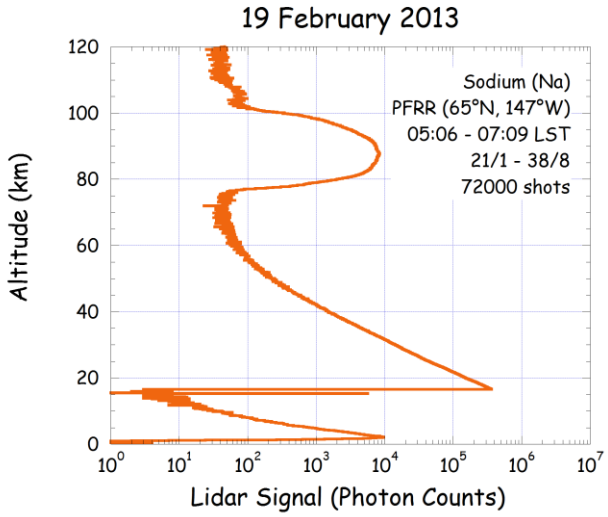

Figure 2.20 Average Na profile from observations on 19 February 2013.

Comparing the Rayleigh signal in these measurements taken with the Nd:YAG-pumped laser to measurements taken with the excimer-pumped laser, we can determine the relative increase in laser power. Using Rayleigh counts from 30-40 km from 19 February 2013 data and from 23-24 October

2012 data for 40,000 laser shots on each night, we find that the Nd:YAG-pumped laser gives about seven times more signal than the excimer-pumped laser. This number is very similar to the ratio of the powers measured with the energy meter, 9 times, as discussed earlier. Due to the increased signal, we could now decrease the integration time to calculate densities from photon counts, and increase our time resolution. Keeping the same ratio of bin width to bin spacing, we now integrate over a 12 minute sliding window with a step size of 3 minutes, increasing the resolution by a factor of 5 over the densities produced from previous observations with the excimer-pumped dye laser. The false color plot is shown in Figure 2.21. Small undulations can now be clearly seen in great detail, even though the time span of this observation is not any longer than those shown in this chapter from the excimer-pumped laser – only about 2 h. Initially the layer is bifurcated, with the upper peak density being higher, but as time goes on the peak descends and the density decreases to a constant value for most of the observation. Slight short-period

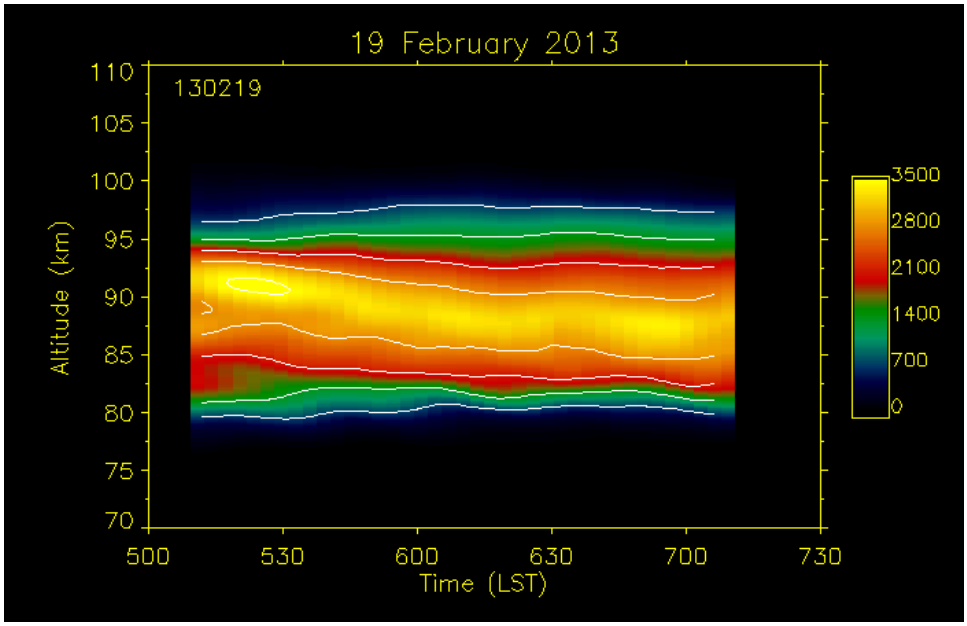

Figure 2.21 False color Na density plot from the night of 19 February 2013.

wave motions are visible on the bottom side of the layer throughout the observation.

2.8.5. 12-13 March 2013

On our second night of observations with the new laser, we began with a linewidth scan in profiles 1-12 (Figure 2.22). Signals greater than 25% of the maximum were used in the fit of the lineshape. The value of the linewidth was calculated to be 3.7 pm, much narrower than the previous night's measurements and also narrower than the measurements taken with the excimer-pumped laser. The value of C_{eff} was determined to be 3.9×10^{-16} m^2. Wavelength calibration of the grating had again shifted due to moving the grating several nanometers, and we found the new peak to be at 595.118 nm. We took data at this wavelength for nearly 6 h, only shifting by 1 pm near the end of the dataset. The integrated profile for this data is shown in Figure 2.23.

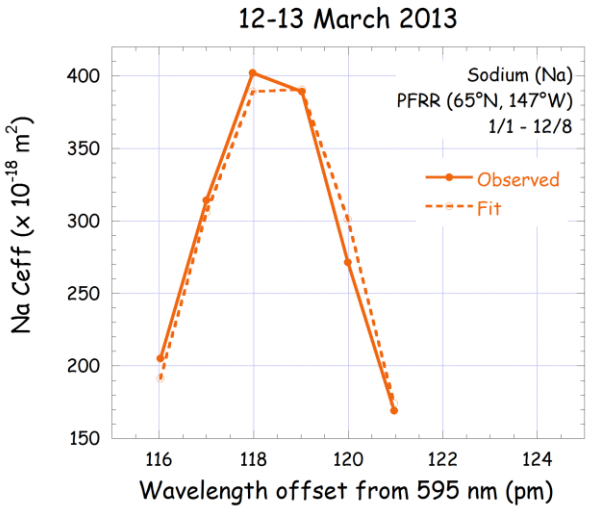

Figure 2.22 Na linewidth scan on 12-13 March 2013.

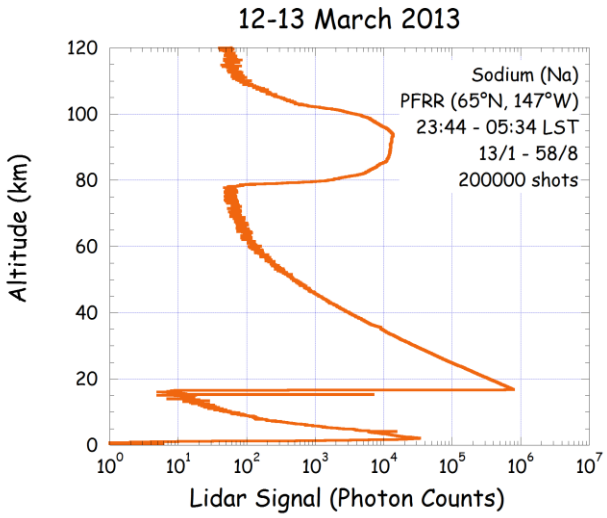

Figure 2.23 Average Na profile from observations on 12-13 March 2013.

The false color plot for this data shows very significant motion, made clear by the high resolution provided by the new laser (Figure 2.24). In the middle of the observation period (0200 – 0300 LST) overturning of the Na is seen. Such overturning is associated with breaking of atmospheric waves [Collins and Smith, 2004]. During this episode, the peak of the layer trails off toward the bottom around 85 km while a new peak forms around 95 km, bifurcating the layer significantly. After the former peak has disappeared, the bottom edge of the layer moves up several kilometers. The new peak then spikes to a much higher concentration than the rest of the night and remains at that intensity for about an hour before decreasing and broadening again near the end of the night. A sporadic layer forms at about 100 km for about 0.5 h prior to the overturning [Collins et al., 1996]. Many small also perturbations are seen in the layer throughout the night and may reflect small-scale wave breaking and turbulence [Pfrommer et al., 2009].

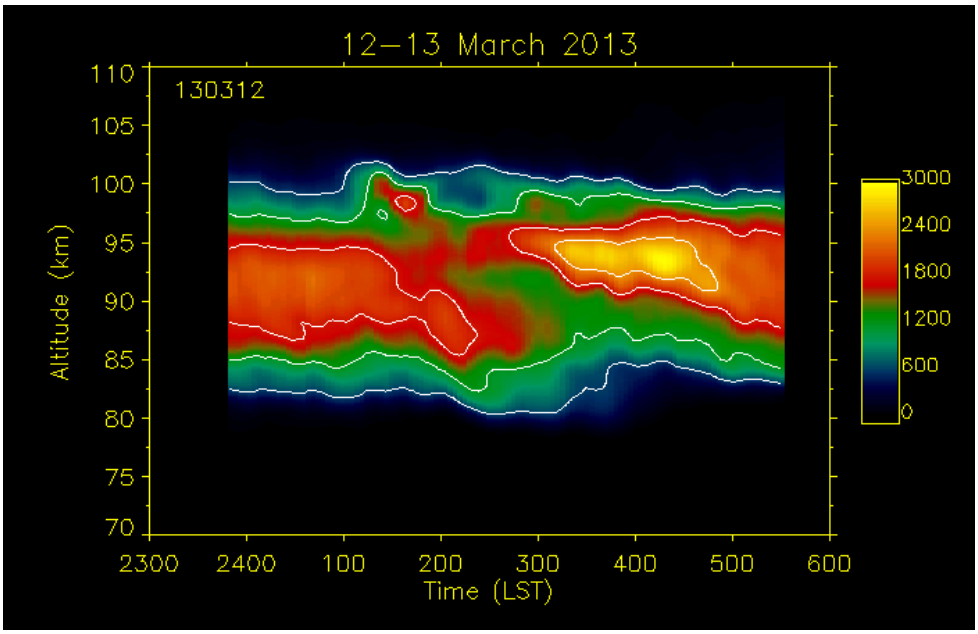

Figure 2.24 False color Na density plot from the night of 12-13 March 2013.

2.8.6. 16 March 2013

Data began after midnight on the morning of 16 March for a final night of Na observations with the Nd:YAG-pumped dye laser during the 2012-2013 season. We began at a grating setting of 595.132 nm, but the peak of the line drifted to 595.135 nm within two hours and to 595.137 nm within the next hour. We took a linewidth scan in sets 34 through 41 near the end of the night which gave similar results to that from 12-13 March. The linewidth was measured to be 4.0 pm with a C_{eff} of 3.8×10^{-16} m^2 (Figure 2.25). Signals greater than 25% of the maximum were used in the linewidth calculation. Figure 2.26 shows the integrated profile for the data taken in sets 1 through 33.

The continuous measurements for this night span about 4 h and show a variety of behavior in the layer, including a major blooming on the bottom side into a bifurcated peak near the beginning of the night (Figure 2.27). This enhancement dissipates in what appears to be a wave breaking motion. The

peak of the layer remains relatively constant in density while decreasing in altitude slightly over the night. No distinct, smooth wave patterns can be seen in this data, but there are many interesting dynamics visible.

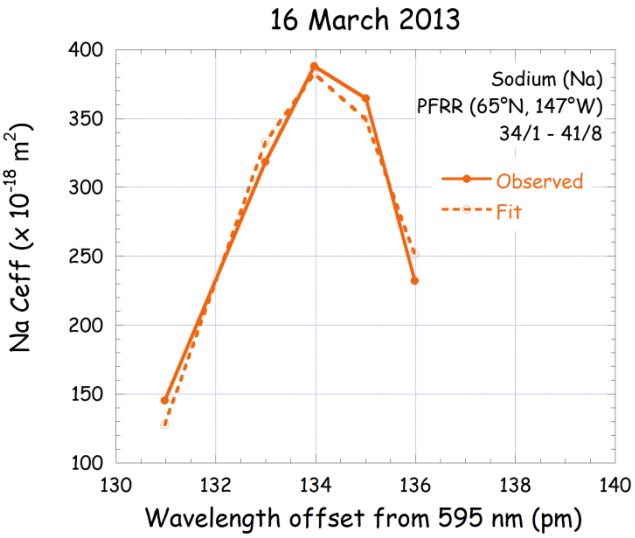

Figure 2.25 Na linewidth scan on 16 March 2013.

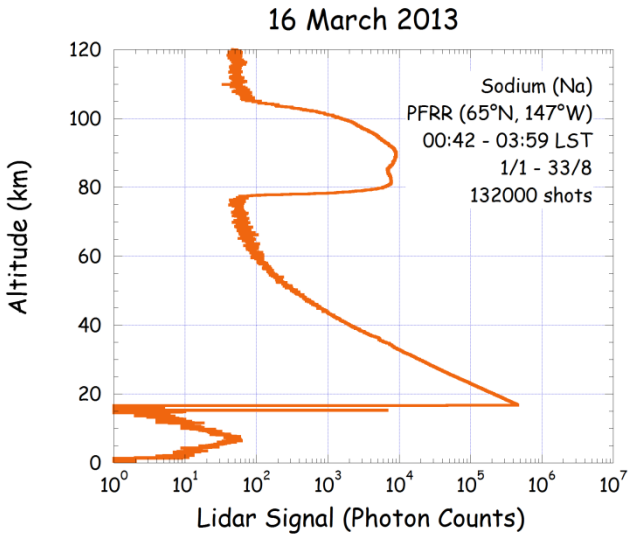

Figure 2.26 Average Na profile from observations on 16 March 2013.

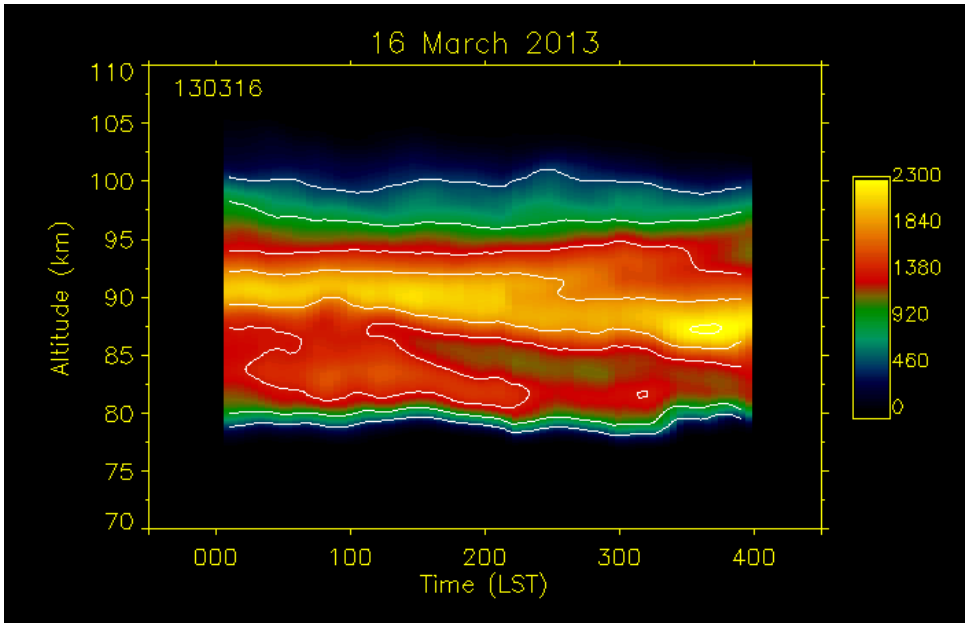

Figure 2.27 False color Na density plot from the night of 16 March 2013.

2.9. Analysis of lidar system performance

To demonstrate the use of the lidar equation and to determine the system efficiency (ηT^2 in the lidar equation) with both lasers, we present an analysis of the photon counts on one night from each laser: 23-24 October 2012 and 12-13 March 2013. Table 2.4 lists the system parameters and data from each of these nights that are used in the lidar equation.

First in our analysis, we calculate the peak Na density manually using Equation 2.12. Taking a 1 km slice centered on the peak of the layer, Z_{Res}, we determine the photon counts in this range, N_{Res}. We take the Rayleigh counts N_{Ray} in a 1 km slice centered at 30 km, and background counts N_{Bkg} from 120-125 km. The background is scaled to the size of the 1 km range and subtracted from the counts in the resonance and Rayleigh ranges to give the resonance and Rayleigh signals. Density of air, ρ_{Air} (density of Rayleigh scatterers) is calculated from radiosonde data at 30 km. Values of C_{eff} were determined by linewidth scans; both were approximated to 3.8×10^{-16} m^2, the

Table 2.4 Lidar observation parameters for efficiency analysis

Parameter	23-24 October 2012	12-13 March 2013
Z_{Res}	87.2	93.7
N_{Res}	64993	190370
N_{Ray} (29.5 - 30.5 km)	34164	397350
N_{Bkg} (120 - 125 km)	4399	3745
σ_{π}^{R} (589.0 nm)	4.14×10^{-32} m^2/sr	
C_{eff}	3.8×10^{-16} m^2	
ρ_{Air} (30 km)	3.92×10^{17} cm^{-3}	3.42×10^{17} cm^{-3}
ρ_{Res} (automated)	8060	2060
ρ_{Res} (manual)	8740	2130
Laser Energy, E_L	3.0 mJ	26 mJ
N_{shots} ($R_L\Delta t$)	88000	200000
Laser Wavelength, λ	589.0 nm	
Receiver Area, A_R	0.805 m^2	
ηT^2 (Resonance)	0.32%	0.21%
ηT^2 (Rayleigh)	0.29%	0.20%
ηT^2 (Expected)	1.50%	

closest value pre-programmed with accompanying parameters into the density calculation routine. The Rayleigh scattering cross-section, σ_{π}^{R}, was calculated from Equation 2.8 for 589.0 nm. Inserting these values into Equation 2.12, we obtained a manual value for ρ_{Res} in the 1 km peak density range. Automated values for the same range are also listed in the table. The manually calculated values using a simple, rough approximation are within 10% of the values from the automated density routine, which takes into account beam absorption as it goes through the Na layer and analyzes densities at a 75 m resolution.

To compare the operation of our two lasers with the large-aperture receiver system, we calculate the lidar system efficiency factor, which includes the efficiency of the receiver and the transmission of the atmosphere, for each of the selected nights. All the other values in the lidar equation are known from the observations, and we can calculate the

efficiency separately for the resonance and Rayleigh ranges, giving us a comparison to assess the accuracy of the calculation. The lidar equation for resonant scatter is given in Equation 2.7, and the equation for Rayleigh scatter is given in Equation 2.9. Plugging in values to these equations from Table 2.4 and solving for ηT^2, we find that the efficiency factor was about 0.3% with the excimer-pumped dye laser on 23-24 October, while it was about 0.2% for observations with the Nd:YAG-pumped dye laser on 12-13 March. Efficiencies calculated for the resonance and Rayleigh ranges were within 10% of each other on both nights. We calculate an expected value for ηT^2 at 1.5% based on a 50% transmission of the atmosphere, five optical surfaces in the telescope with a 90% reflectivity, a 50% transmissive filter, and a quantum efficiency in the PMT of 20%. Our efficiency values are lower than this expected value by a factor of five or more; this is likely from the transmission of the atmosphere, which is variable and cannot be easily determined as a separate factor. Due to ice particles in the Alaskan winter atmosphere, much light may be scattered out of the laser beam, reducing the efficiency significantly. Our values of ηT^2 are consistent with those obtained by Light [2009] of about 0.6% using the same telescope, but a PMT with a quantum efficiency of 40% instead of 20%. This reduction in PMT efficiency accounts for the corresponding reduction in the value of ηT^2.

3. Waves in the Mesospheric Metal Layers

In this chapter, we investigate the behavior of the mesospheric metal layers, through previous observations from LRL-PFRR made between December 2000 and January 2003. We revisit the conclusions of several former studies of motions in the metal layers, both from LRL-PFRR and elsewhere, that discussed oscillations in the metal layers and common motions between multiple metals.

3.1. Wave motions in the mesosphere

Density measurements of mesospheric metals can be used as a tracer for air motions in the mesosphere. Long-period oscillations (i.e., 2-13 h) of the Na layer were studied by Collins and Smith [2004] using lidar observations from LRL-PFRR. They used harmonic fits to several density levels in night-long datasets to characterize the motions of the layer. These density levels were defined by fractions of the peak density ρ_{max}: $\rho_{max}/2$, $\rho_{max}/4$, $\rho_{max}/8$, and $\rho_{max}/16$. The density contour with the best fit was then used to fit the other contours to the same period. By using a linear fit to the phase of each of these fits, it is possible to calculate the vertical phase progression of the oscillation and obtain a vertical wavelength. It was found that 24 of the 52 nights considered showed downward propagating harmonics consistent with upward propagating gravity wave behavior. This conclusion was corroborated by simultaneous observations of OH airglow temperature that also showed similar oscillations. The method used by Collins and Smith was biased toward long-period waves, as the wave must remain coherent for the duration of each observation to be detected.

Common motion of the Na and Fe layers has been presented by Yi et al. [2008] from simultaneous lidar observations of both metals taken in

China. The authors note a high correlation between contours of Na and Fe in threshold. Out of 26 observations over the course of a year, 12 of these nights yielded measurements with high SNR that allowed for detection of the bottomside of both layers with high accuracy and precision. On these 12 nights, the correlation coefficient between the altitudes of the Na and Fe contours is 0.96. While the authors report the common movement of the layers, they do not suggest a mechanism for the phenomenon, but simply report the observations.

Strong correlation between species in the upper atmosphere was also reported by Gelinas et al. [2005], in which sounding rocket measurements of charged dust in the mesosphere were compared to lidar measurements of iron. The profiles of the dust and the metal species were found to be very similar, including their change over the course of the night.

On a smaller scale, downward motions in the bottom side of the Na layer have been observed coincident with the motion of a mesospheric inversion layer (MIL) at LRL-PFRR, [Collins et al., 2011]. The sodium descended with the topside of the MIL, where the temperature lapse rate was adiabatic. The sodium observations were made at a resolution of 15 minutes and so could resolve turbulent eddies directly. However, the authors analyzed the motions in terms of diffusive transport and estimated the eddy diffusion in the upper mesosphere associated with this event. Coherent oscillations with a period of several hours that propagate vertically throughout the layer were also present in the observations. The movement of the Na and the MIL appears to be consistent with gravity wave breaking as the features follow a downward phase progression.

Pfrommer et al. [2009] employ a lidar system with a large 6-meter mercury mirror to achieve very high resolution measurements of the sodium layer, on the order of 10 m in altitude and 100 ms in time. Exquisite

turbulent features with Kelvin-Helmholtz billows are observed in the bottom side of the Na layer with this system. Coherent oscillations with upward propagating waves are seen on a small scale, and fine stratification that the authors believe is best explained by transport by gravity waves with periods on the order of minutes.

It is well-established that gravity waves play an important role in the middle atmosphere [Andrews et al., 1987]. That the dynamics of the metal layers can be used to observe them directly and characterize their spatial and temporal scales. We seek to extend the work done by Yi et al. [2008] using simultaneous Na and Fe observations from LRL-PFRR, by characterizing common motions in the Na and Fe layers in terms of gravity waves. To do so, we analyze the layers using a similar technique to that used by Collins and Smith [2004]. Thus, we provide a better framework for understanding the motion of the metal layers and the gravity waves that perturb them.

3.2. Seasonal characteristics of the Na and Fe layers

Observations of the Na and Fe layers show significant annual variations, with both layers experiencing a maximum in their abundances in winter and a minimum in summer [Plane, 1991]. Several nightly averages for observations of the Na and Fe layers at LRL-PFRR in each season of the year are shown in Figure 3.1. Seasonal changes in both layers are clearly visible; the layers are broader and denser in the winter than summer. Furthermore, the peak of the layers are found at a lower altitude in winter than in summer. This behavior is generally understood as follows: the mesopause region is colder in summer than winter and the chemistry of the metals favors free metals at higher temperatures [Plane et al., 1998].

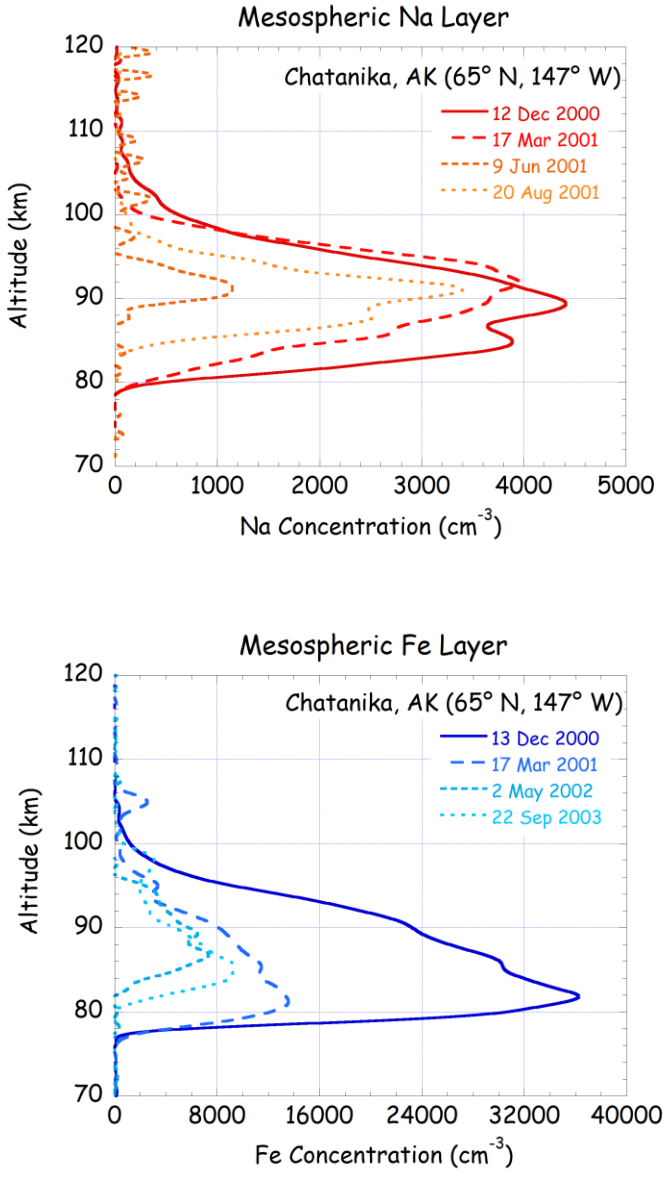

Figure 3.1 Nightly average profiles of Na (top) and Fe (bottom) taken at several points throughout the year to show annual variations.

Data taken at LRL-PFRR over the course of several years (1999-2003) has been fit to an annual sinusoidal pattern in Figure 3.2. The nightly average column abundance, centroid height, and RMS width of the Na and Fe layers are shown as a function of day in the calendar year. Abundances of Fe are much more variable over the year than Na, with Na about nine times

more abundant in winter than summer while Fe decreases 20 times from its wintertime maximum in summer. The centroid height also changes more in Fe than in Na, with Na about 89 km in winter and 92 km in summer while Fe moves from around 85 km in winter to 93 km in summer. However, RMS width is more variable in Na than in Fe, with Na varying between 3 and 5 km while Fe fluctuates slightly around 5 km. The Fe layer comes to a much sharper peak when at its maximum abundance than Na, and the density gradient is much stronger, especially on the bottom side, in Fe than Na. Layer characteristics from Na observations taken during this study (discussed in Chapter 2; Table 2.3) fall within the ranges of these annual fits. Parameters used in calculating the fit curves are tabulated in Table 3.1.

Table 3.1
Annual fit parameters[1] for column abundance (CA), centroid height (CH), and RMS width (RW) in both metals.

	Constant	Amplitude	Phase Offset
Fe CA	1.17×10^{14} m^{-2}	1.06×10^{14} m^{-2}	354.0 days
Fe CH	89.2 km	3.99 km	193.0 days
Fe RW	4.99 km	0.352 km	297.0 days
Na CA	5.03×10^{13} m^{-2}	3.92×10^{13} m^{-2}	2.0 days
Na CH	90.7 km	1.67 km	167.0 days
Na RW	3.94 km	1.18 km	4.1 days

[1] Data is fit to the equation $x = C + A\,Cos\left(\frac{2\pi}{365}(t-\varphi)\right)$, where x is the desired quantity, C is the constant, A is the amplitude, t is time in days, and φ is the phase offset in days.

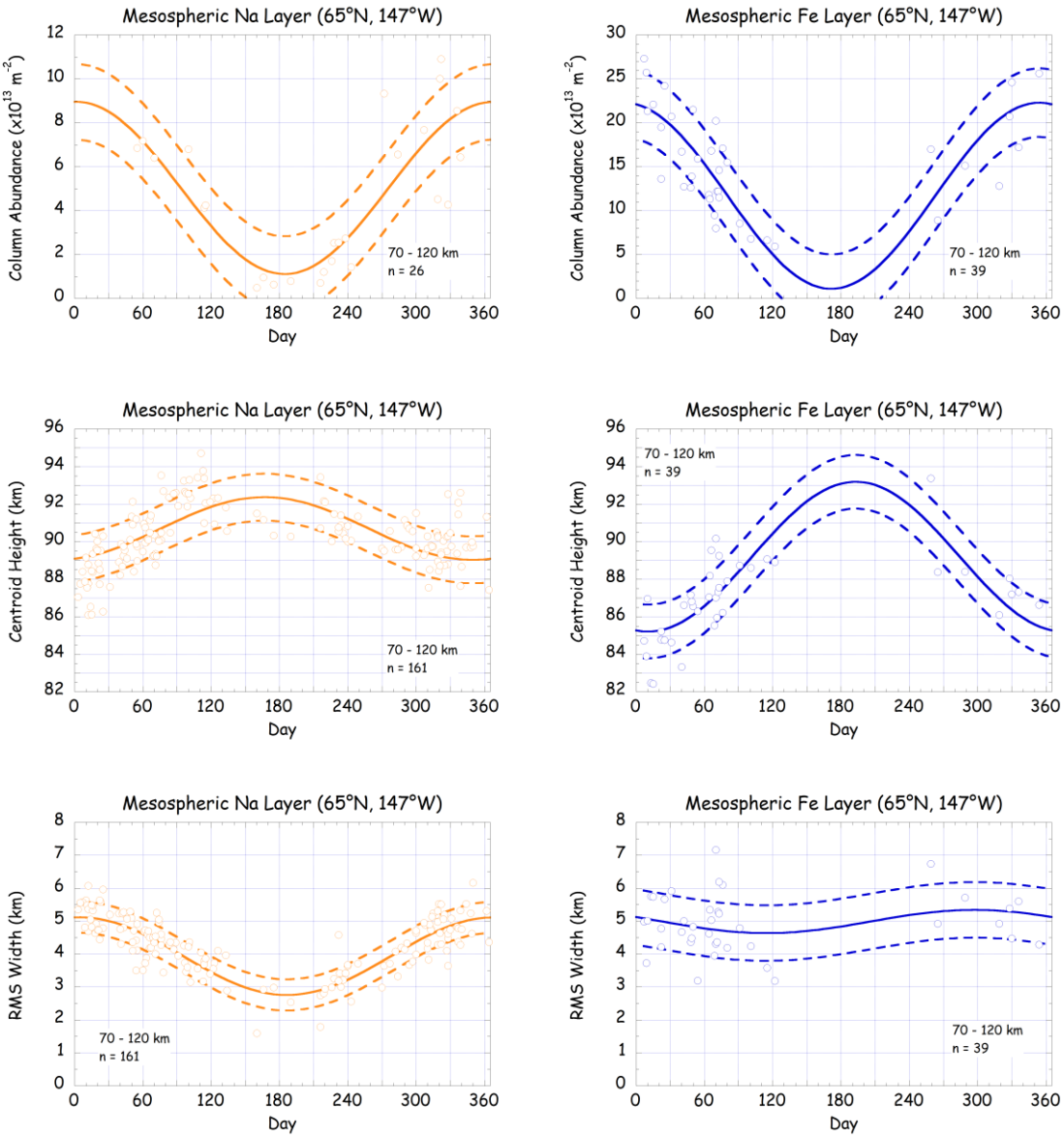

Figure 3.2 Seasonal variation of the Na layer (left panel) and Fe layer (right panel). Plots show column abundance (top), centroid height (middle), and RMS width (bottom) as a function of day within the year. All data points are nightly averages from observations taken at LRL-PFRR. Na data taken between 31 August 1999 and 25 April 2003. Fe data taken between 19 February 2001 and 2 December 2003.

Fits at the summertime minimum are largely extrapolations due to the difficulty of taking observations in the continuous daylight of mid-summer. Although there were some Na observations taken at this time, no Fe measurements were made between May and September. Data for Na column abundance is only from nights when Fe measurements were not made. The Candela flashlamp-pumped dye laser used for these Na measurements (introduced in Chapter 1) tended to drift in its wavelength tuning, and thus yield lower lidar signals (and subsequently lower density values) than expected. However, the Lambda Physik excimer-pumped dye laser used for both Na and Fe measurements is stable enough to allow for a reliable determination of C_{eff} and subsequent calculation of column abundance.

Based on the meteoric abundances, the abundance ratio between Fe and Na (based on number density) is 7.9. However, our observations show that the ratio of the atmospheric abundances is different. Measured column abundance ratio (Fe/Na) over the course of a year is shown in Figure 3.3. The average ratio is 2.1, with a pronounced minimum of 0.9 in summer and a maximum of 2.8 in fall. The midwinter value is 2.5. This discrepancy between meteoric and atmospheric abundances is due to chemical partitioning of each species between free atoms and compounds that occurs at differing amounts between different metal species.

3.3. Concurrent Na and Fe observations at LRL-PFRR

Between December 2000 and January 2003, 21 nights of simultaneous sodium and iron measurements were taken at LRL-PFRR (Table 3.2). Data from these nights forms the basis for our study of corresponding motions in the two metal layers. Densities are produced for these nights for a 60-minute integration time in steps of 15 minutes. For each of these nights of data we extracted constant density contours on the bottomside of the layer to trace

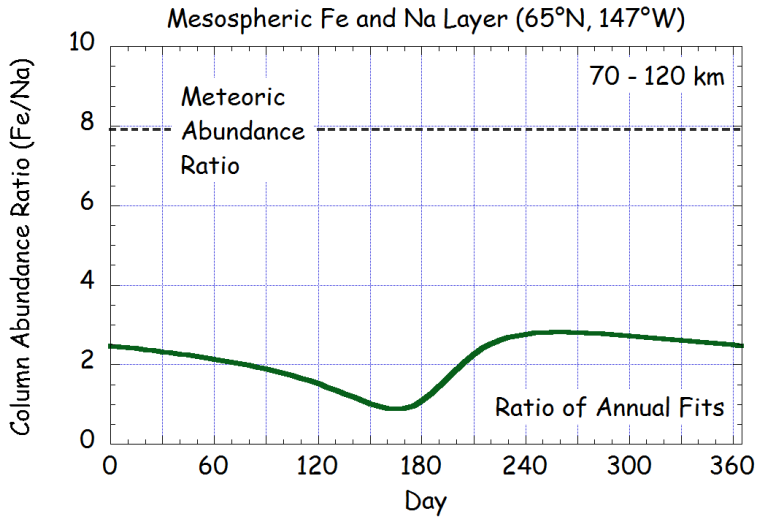

Figure 3.3 Observed abundance ratio of Fe to Na as a function of day within the year, compared to the expected abundance ratio as obtained from meteoric composition.

the motion of the layer. In defining the density contours, we use the average profile for the night and find the altitude of the peak density, then round down to the nearest kilometer and extract the density for that altitude. Moving down the profile, we take the densities in 1 km steps until we reach a threshold of 50 cm^{-3} or until we reach an altitude of 70 km. These densities are then traced throughout the night as they vary with altitude.

Data from the night of 12-13 March 2002 shows well-defined oscillations that are coherent between Na and Fe. False color plots of Na and Fe densities observed on this night are shown in Figure 3.4. The appearance of the layers on these nights is fairly tranquil, with no sporadic layers. High Na density regions in the center of the layer show a continual downward trend, with new patches of high density forming higher in the layer to keep the overall profile fairly constant with time. In Fe, the peak of the layer experiences a sharp increase near the end of the night.

Table 3.2

List of nights with simultaneous observations of Na and Fe, including the start and end times of observations of each metal on that night

Date	Na Start	Na End	Fe Start	Fe End
2000/12/13	21:30	04:30	21:00	04:40
2000/12/15	22:00	06:00	22:00	06:00
2001/02/19	21:30	03:00	21:20	02:40
2001/02/23	22:30	07:20	23:30	07:20
2001/03/17	20:20	05:40	21:30	05:40
2001/11/24	20:40	08:20	21:30	08:00
2001/11/26	21:20	01:00	22:20	07:00
2002/01/22	20:00	09:30	21:00	08:30
2002/01/31	21:00	04:00	21:40	04:00
2002/02/09	00:20	06:30	01:00	06:00
2002/02/11	20:30	05:30	23:00	05:00
2002/03/03	20:00	00:00	21:30	00:00
2002/03/05	19:40	03:20	20:30	02:30
2002/03/06	19:20	06:00	20:00	06:00
2002/03/07	20:00	06:20	20:00	06:20
2002/03/10	20:20	05:40	22:00	05:40
2002/03/11	20:00	05:40	20:20	05:30
2002/03/12	20:30	05:40	22:20	05:30
2002/03/13	19:50	03:30	20:40	06:00
2002/03/14	01:40	05:40	22:00	05:50
2003/01/25	21:20	05:30	21:40	08:30

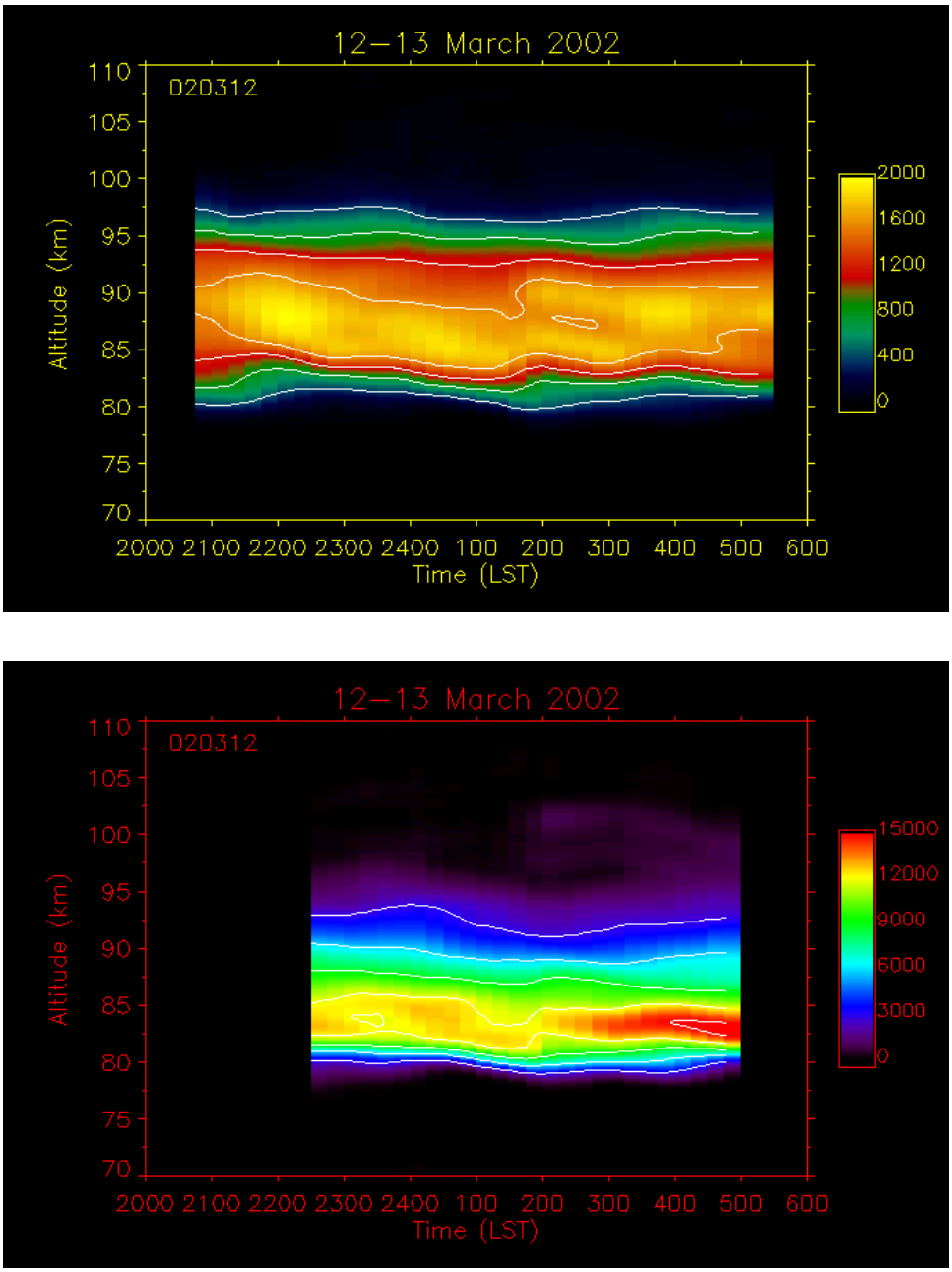

Figure 3.4 False color plots of Na (top) and Fe (bottom) densities on the night of 12-13 March 2002.

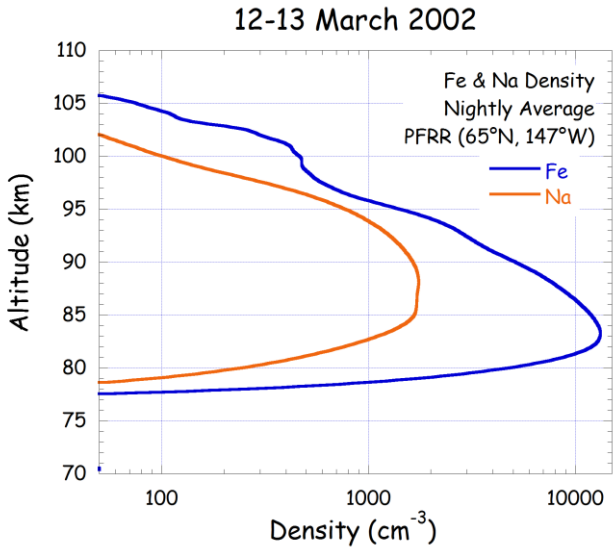

Figure 3.5 Average Na and Fe profiles for the night of 12-13 March 2002.

The average profile for both metals over the night is shown in Figure 3.5. The peak density in Na occurs at 88 km with contours calculated down to 79 km, while the peak density in Fe occurs at 83 km with contours calculated down to 78 km. In selecting contours for fitting, we exclude the top 4 Na contours, which are all bunched together in the center of the layer, leaving six bottom side contours from 84 km to 79 km. The 83 km Fe contour is very short compared to the length of the data (density was only at that level for the latter part of the night), and the 82 km contour has a discontinuity, so we exclude both of those leaving four contours from 81 km to 78 km. Thus we are left with three overlapping contours at 81, 80, and 79 km (Figure 3.6).

Comparing the motions of the sodium and iron layers, we plot the density contours from equivalent altitudes in the average profile against one another. Ideally, if the sodium and iron layers move together as they are both

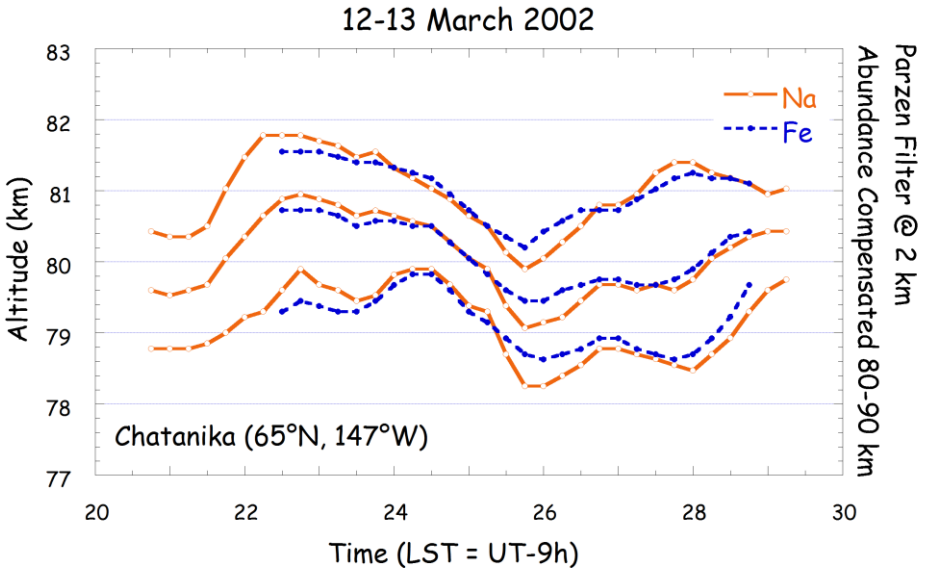

Figure 3.6 Overlapping Na and Fe contours on the night of 12-13 March 2002.

perturbed by the same wave motions, these plots would show a straight line. We perform a least-squares fit on each altitude and calculate Pearson's R correlation coefficient for the fit as follows:

$$R = \frac{\sum_i (x_i - \bar{x})(y_i - \bar{y})}{\sqrt{\sum_i (x_i - \bar{x})^2}\sqrt{\sum_i (y_i - \bar{y})^2}} \tag{3.1}$$

where the data points are (x_i, y_i) and $\bar{x}$ and $\bar{y}$ are the mean values of the individual point coordinates [Press et al., 1992].

On the night of 12-13 March, correlation of the contours between Na and Fe is exceptionally good on the bottom side of the layer. The 80 km contour gives a correlation of 0.99, while the 81 km contour gives a correlation of 0.98 (Figure 3.7).

Lower correlation between the two metal layers is seen on the night of 17-18 March 2001. False color plots of this data are shown in Figure 3.8.

Much more complicated dynamics are apparent, especially in the iron layer where a very high-altitude sporadic layer appears at 105 km between 0100 and 0200 LST. This high-altitude sporadic layer is followed by a second sporadic layer nearer to the main layer at 95 km from 0200 to 0300. The main peak of the Fe layer has some fluctuation in density and altitude over time but is not very dramatic. The Na layer experiences some significant fluctuations in density in the middle part of the layer. Both layers still show some wave motion on the bottom edge. Correlation, however, is lower, with the best R-value only 0.73 at the 81 km contour (Figure 3.9).

On the night of 13-14 December 2000, the Na and Fe layers do not move together at all. False color plots (Figure 3.10) show very little dynamics; the layers are rather featureless. The best correlation is 0.48 on the 79 km contour (Figure 3.11). The lack of large-amplitude wave motions allows small scale random motions to dominate the movement of the Na and Fe contours. As a result, there is no clear common motion observed.

For each night we pick the contours at altitudes where the sodium and iron layers overlap and correlate the two metals at each of these altitudes. Towards the peak of the layer the contour path is often chaotic, but contours near the bottom edge often display wave patterns that correlate well. The best correlation out of the overlapping altitudes is tabulated for each night in Table 3.3. The layers appear to correlate quite well; of these 21 nights, 14 (67%) have a correlation coefficient higher than 0.85, and the lowest value of correlation is 0.48. Very high correlations are common; 11 (52%) of these nights have a maximum correlation greater than 0.95.

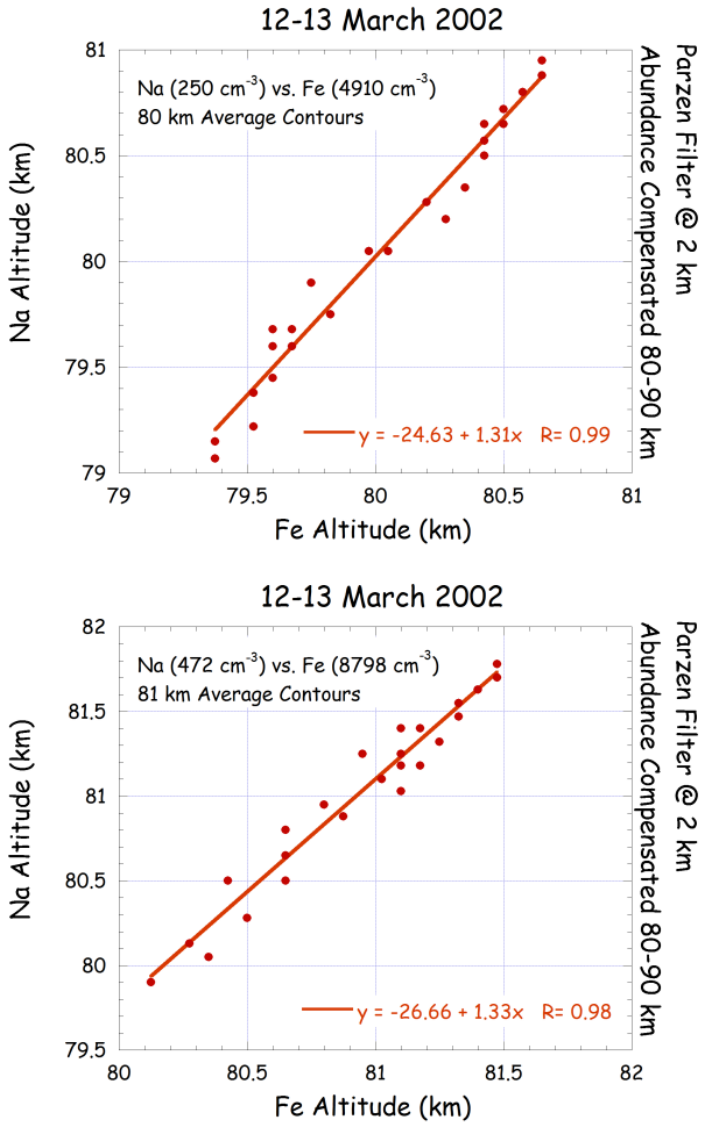

Figure 3.7 Na vs. Fe contours with best correlation, 80 km (top) and 81 km (bottom) for the night of 12-13 March 2002.

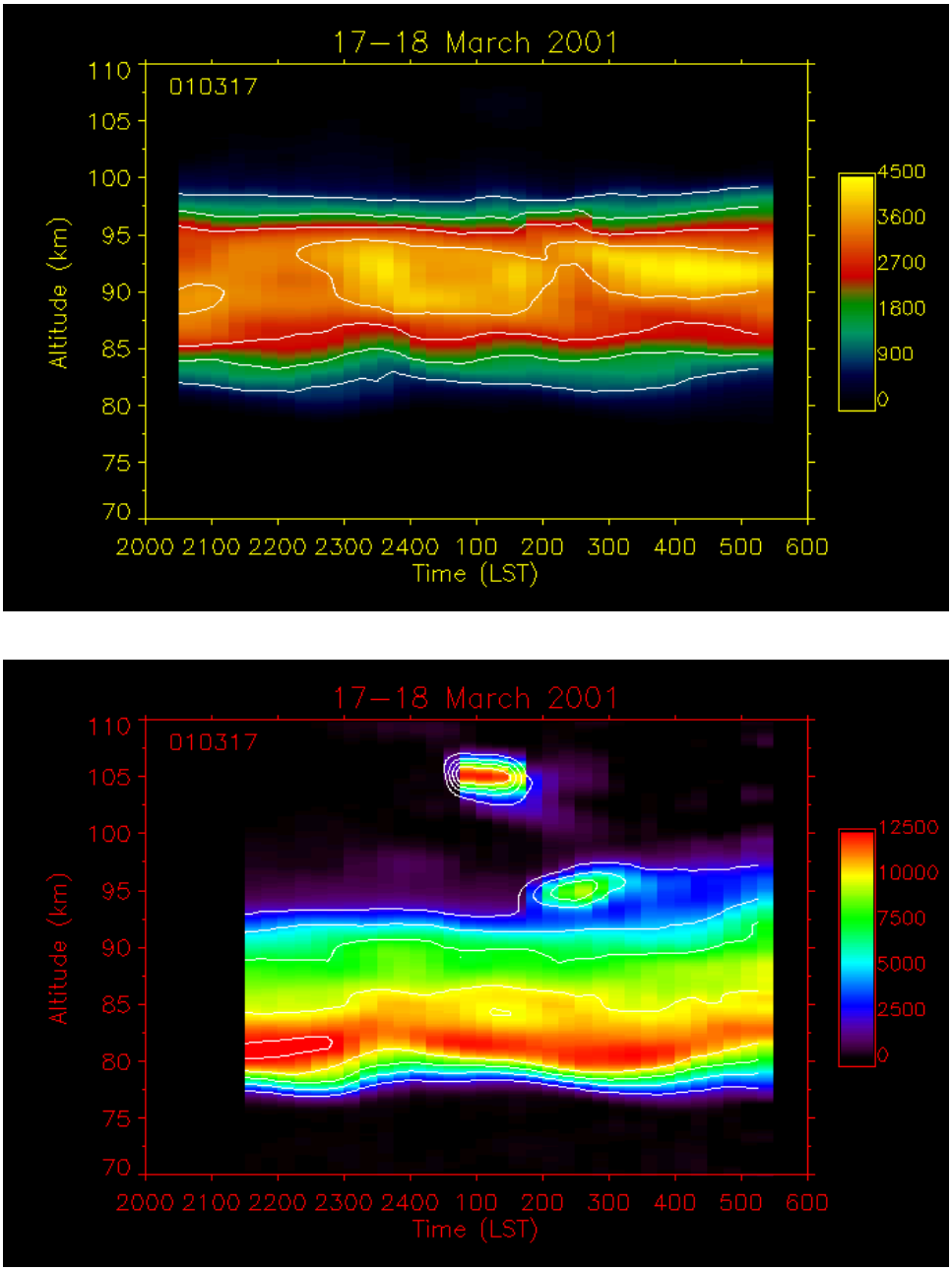

Figure 3.8 False color plots of Na (top) and Fe (bottom) densities on the night of 17-18 March 2001.

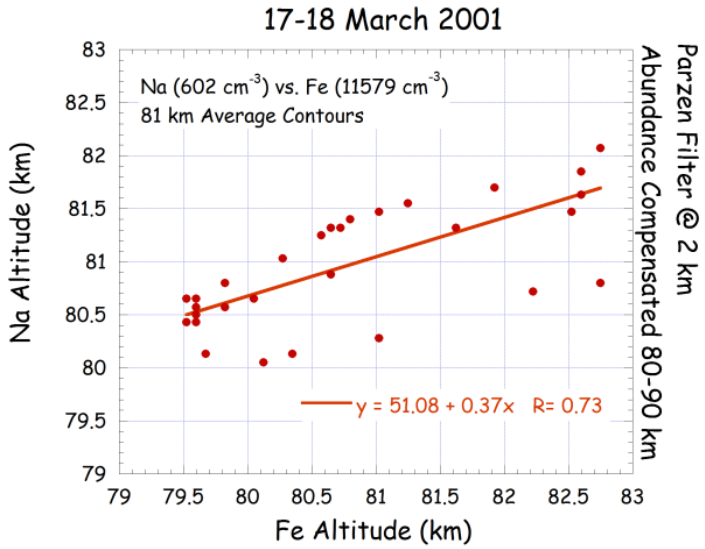

Figure 3.9 Na vs. Fe 81 km contour, best correlation for the night of 17-18 March 2001.

3.4. Contour fits to wave motions

Correlation in the motions of the two metal layers suggests an atmospheric forcing for the motions, but does not provide insight as to the mechanism. Our hypothesis is that the motions in the bottom side of the metal layers are manifestations of gravity waves, so we look for wave motion in the density contours that should be similar in both metals. For each night, we fit all the contours in both metals to the harmonic wave equation [Collins and Smith, 2004]

$$Z(t) = Z_0 + Z_m t + A\,Cos\left(\frac{2\pi(t-\varphi)}{T}\right) \tag{3.2}$$

where $Z(t)$ is the altitude of the density level as a function of time, Z_0 is the reference altitude, Z_m is the slope of a linear component (usually very small), and A, φ, and T are the amplitude, phase, and period, respectively, of the harmonic. The effectiveness of the fit is determined by the signal-to-noise ratio (SNR), which is calculated by

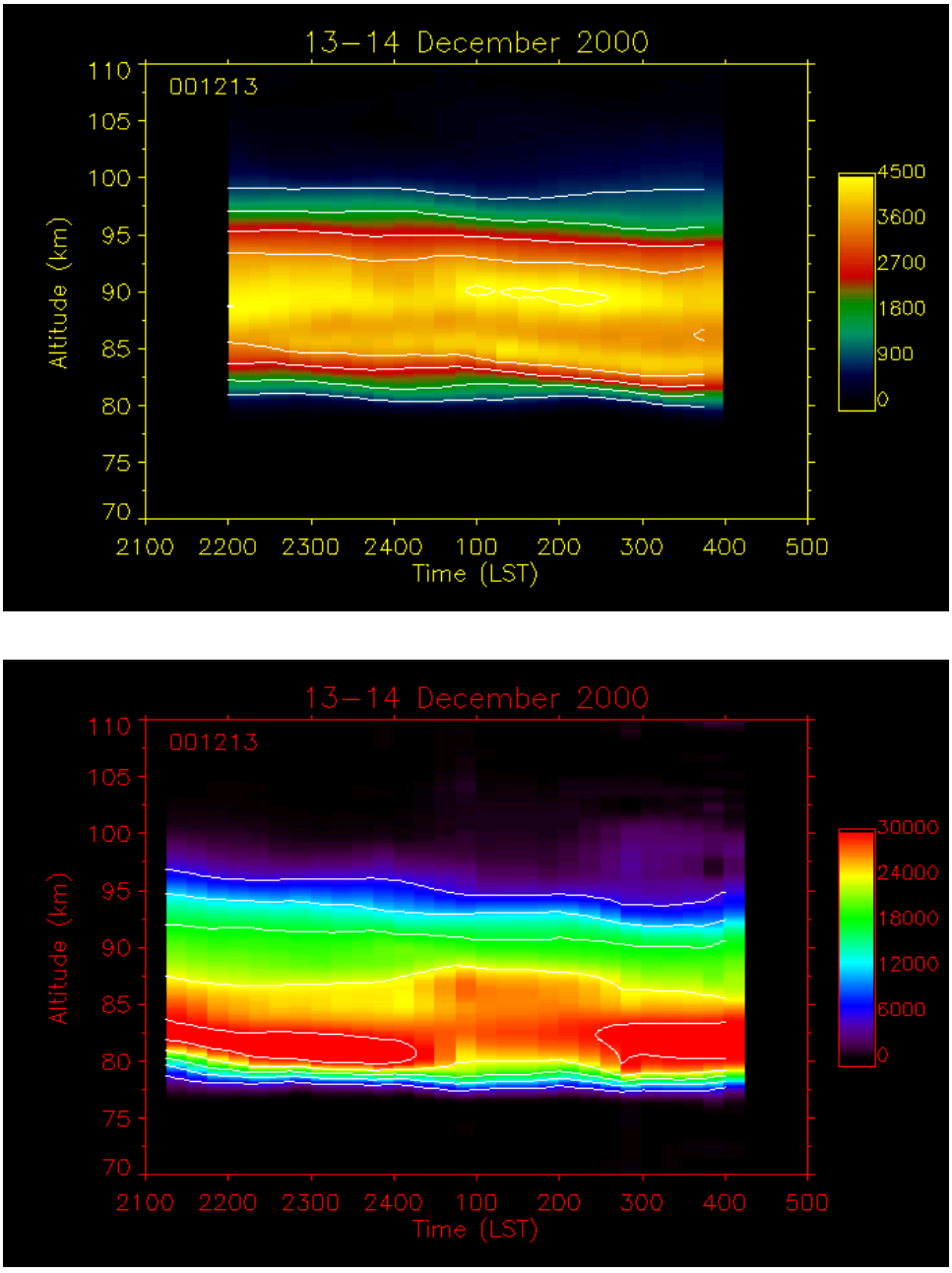

Figure 3.10 False color plots of Na (top) and Fe (bottom) densities on the night of 13-14 December 2000.

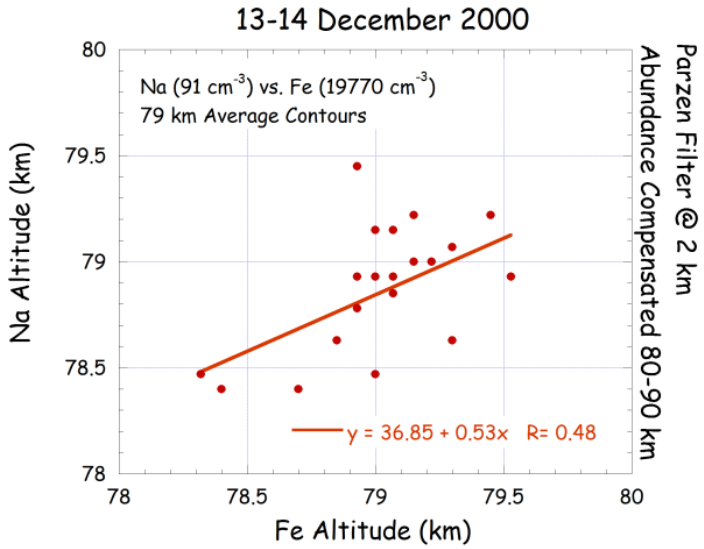

Figure 3.11 Na vs. Fe 79 km contour, best correlation for the night of 13-14 December 2000.

$$SNR = \frac{1}{2}\left(\frac{A}{E_{RMS}}\right)^2 \tag{3.3}$$

where E_{RMS} is the RMS error in the fit. Following the Monte Carlo method used by Collins and Smith, we determine the approximate significance level of the fit based on the SNR and the number of points used (Figure 3.12).

In addition to fitting each contour to its own harmonic, the fit for each contour was propagated to the other contours by fitting them to a harmonic with the same period as the selected contour. If the motion is caused by gravity waves, it should propagate vertically. These fits were then used to calculate a vertical wavelength by fitting the phase of the fit versus the average altitude of the contour to a straight line. The vertical wavelength is then the period divided by the slope of this line. In the vertical wavelength calculation, contour fits with SNR values lower than 0.25 were discarded so as to avoid skewing the estimated wave parameters by inclusion of poor fits.

Table 3.3 Best correlation coefficient by altitude between Na and Fe on each night in the dataset

Date	Average Altitude (km)	Na Density (cm^{-3})	Fe Density (cm^{-3})	Pearson's R	Number of points
2000/12/13	79	91	19770	0.48	24
2000/12/15	76	71	13042	0.87	29
2001/02/19	80	105	6686	0.98	17
2001/02/23	85	854	21082	0.49	27
2001/03/17	81	602	11579	0.73	32
2001/11/24	81	310	15398	0.88	17
2001/11/26	86	2221	23979	0.8	7
2002/01/22	80	104	12429	0.79	42
2002/01/31	79	421	19823	0.72	21
2002/02/09	79	448	15595	0.89	17
2002/02/11	79	217	2426	0.99	24
2002/03/03	81	300	11508	0.97	8
2002/03/05	80	97	2831	0.98	25
2002/03/06	83	687	8706	0.99	22
2002/03/07	81	211	4315	0.98	36
2002/03/10	80	238	4548	0.98	28
2002/03/11	81	293	3905	0.96	32
2002/03/12	80	250	4910	0.99	26
2002/03/13	80	242	3736	0.75	24
2002/03/14	81	419	6250	0.97	12
2003/01/25	76	451	2394	0.97	28

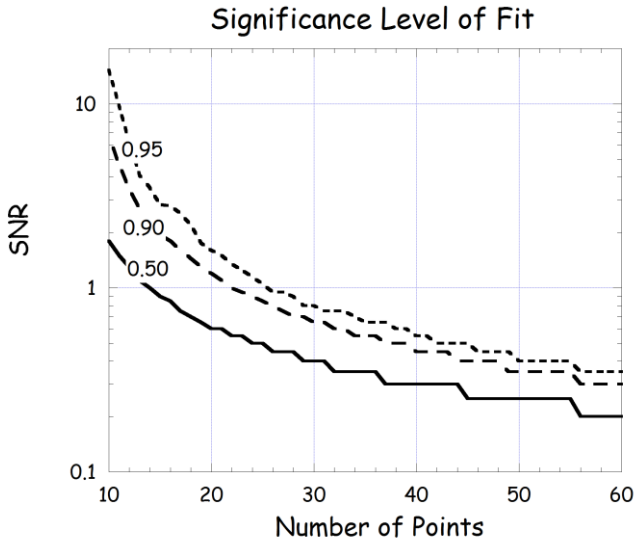

Figure 3.12 Significance level of fits to a certain number of points for a particular SNR. Based on a Monte Carlo technique with harmonic fits to random noise. Adapted from Collins and Smith [2004].

To choose contours for accurate fitting to wave motions, some visual inspection was necessary. Because our method of selecting density levels includes the entire half of the layer below the peak, the upper contours near the middle of the layer often do not follow distinct wave motions and can sometimes be discontinuous. In the lowest part of the layer, contours may also be discontinuous due to the low density levels. Although the SNR threshold eliminates many of these problematic contours from the vertical wavelength calculation, it does not always catch them, so we eliminate them from our fits manually. Contours that showed good wave motions but had small data gaps were not used for fitting to find the best period, but were fit to periods from other selected contours for the purposes of the vertical wavelength calculation. After this pruning, we had several contours in the bottom side of the layer with which to propagate the phase progression with height. Exceptions are several Fe nights in which no fit showed a high

enough SNR to exceed the threshold value of 0.25 in more than one contour, so the vertical wavelength could not be calculated.

If gravity waves are the cause of the wave motions in the metal layers, waves with the same period should be seen in both metals. Since the Na layer is less steep on the bottom side and less prone to sporadic layering than the Fe layer, we believe it to be a more robust tracer of gravity wave activity. To investigate common behavior between the two metal layers, we fit the qualifying Fe contours to the best fit period from the Na layer on that night and obtain a vertical wavelength from the phase progression.

The night of 12-13 March represents the best instance in our dataset of a clear phase progression with height that is similar between the Na and Fe layers. Plots of the all the contours for each metal and their fits to the best fit period for Na are shown in Figure 3.13. The maximum SNR occurred in both metals at 81 km. In Fe, the fit period was 4.9 h with a SNR of 6.8, while Na gave a fit period of 5.1 h with a SNR of 3.2. Propagating these periods to all the other contours in the respective layer, we obtain a vertical wavelength of -11.9 km for Na and -10.0 km for Fe. Thus we obtain downward propagating harmonics with a very similar wavelength in both metals, as would be expected for gravity wave behavior. To push the comparison farther, we fit the Fe contours to the Na best fit period and calculated a vertical wavelength of -10.1 and a maximum SNR of 6.8, very similar to the values for the Fe best fit period. The SNRs plotted with height in Figure 3.13 are for the fit to the Na period in both Na and Fe contours.

The best fit contours in Na for each night are listed in Table 3.4 along with the calculated vertical wavelength for the fit period. Of the 21 nights of data, 19 show harmonic fits at or above the 95% confidence level based on Figure 3.12; the remaining two are above the 90% confidence level. The periods of the fits range from 2.3 to 11.6 h, with an average of 5.3 h.

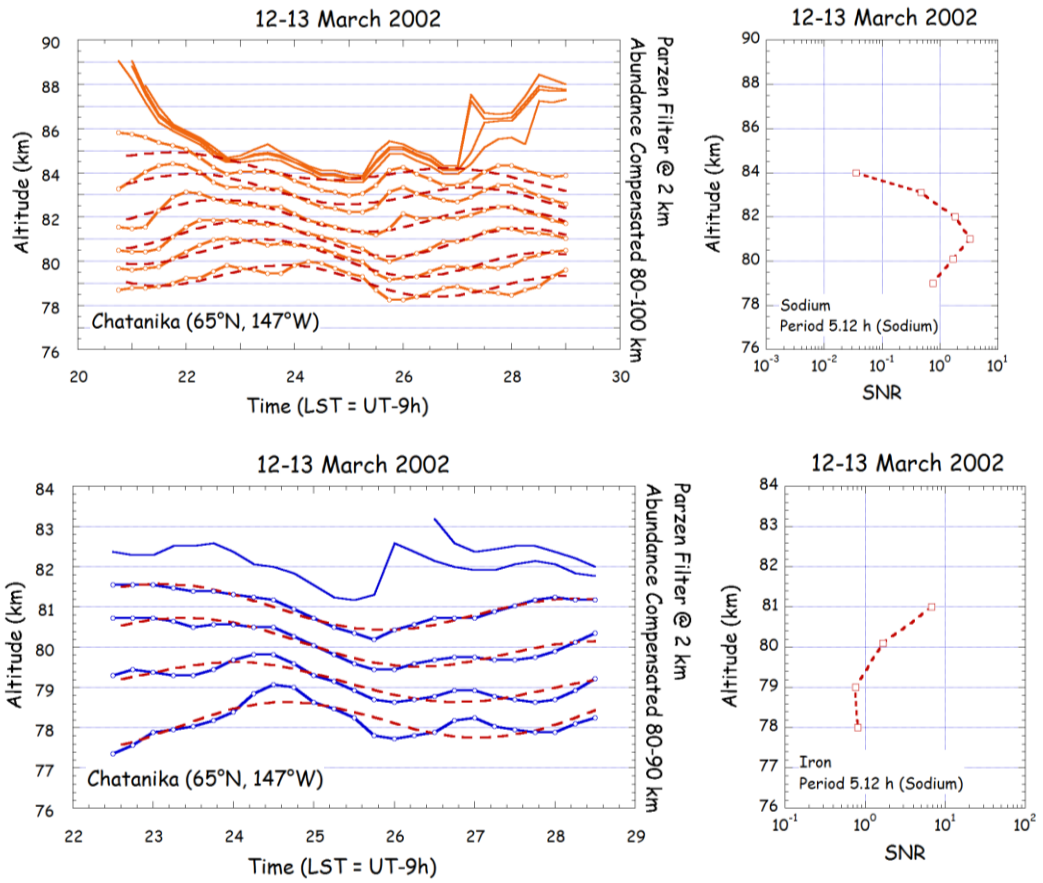

Figure 3.13 Na (top) and Fe (bottom) contours (solid) and fits (dashed) to the best fit period for Na, 5.12 h, which was found for the 81 km contour. Upper contours in each metal, shown without fits, were not fit because of their position close to the middle of the layer. The right panel shows the SNR of the fit on each contour with altitude.

Amplitudes of the waves range from 0.2 to 1.6 km, with an average of 0.8 km. Downward propagating harmonics appear in 19 of the nights, with wavelengths ranging from 9.5 to 70.0 km and an average of 27.5 km.

Fe contours are listed in Table 3.5. Two of these days did not yield high enough SNRs to meet our threshold of 0.25 on more than one contour in the propagation of the best fit period, so a vertical wavelength could not be calculated. Of the remaining 19 days, all have harmonic fits at or above the 95% confidence level save one, which is above the 90% confidence level. Periods range from 1.5 to 8.5 h, with an average of 5.1 h; amplitudes range

Table 3.4 Na best fit contours

Date	Altitude (km)	Density (cm^{-3})	Period (h)	Amplitude (km)	Wavelength (km)	SNR	Points	Significance
2000/12/13	81.0	1322	3.4	0.30	-11.9	4.2	24	95%
2000/12/15	79.0	898	4.6	1.07	190.1	1.6	30	95%
2001/02/19	84.0	1206	2.7	0.34	18.1	1.7	18	90%
2001/02/23	85.0	854	6.7	0.92	-10.1	5.6	32	95%
2001/03/17	80.1	295	4.9	0.67	-17.8	4.2	36	95%
2001/11/24	83.1	991	6.4	1.57	-21.4	1.6	43	95%
2001/11/26	85.0	1881	2.3	0.88	-9.5	8.4	12	95%
2002/01/22	83.1	3078	11.6	0.96	-26.5	1.2	51	95%
2002/01/31	82.0	6087	3.0	0.43	-40.3	4.2	25	95%
2002/02/09	80.1	1051	4.6	1.09	-64.3	2.0	21	95%
2002/02/11	79.0	217	5.8	0.66	-38.5	0.9	34	95%
2002/03/03	80.1	195	2.9	0.23	-10.0	6.8	13	95%
2002/03/05	80.1	97	4.9	0.79	-64.8	3.6	27	95%
2002/03/06	83.1	687	9.1	0.87	-70.0	6.1	39	95%
2002/03/07	86.1	1348	7.5	1.38	-36.7	7.7	38	95%
2002/03/10	79.0	89	6.7	1.07	-19.0	4.6	35	95%
2002/03/11	81.0	293	8.0	0.54	-22.1	4.0	35	95%
2002/03/12	81.0	472	5.1	0.73	-11.9	3.2	35	95%
2002/03/13	82.0	838	3.8	0.38	-19.2	1.0	27	95%
2002/03/14	81.0	419	2.9	0.61	-14.7	4.0	13	90%
2003/01/25	75.0	69	4.9	0.47	-14.2	3.0	29	95%

Table 3.5 Fe best fit contours

Date	Altitude (km)	Density (cm^{-3})	Period (h)	Amplitude (km)	Wavelength (km)	SNR	Points	Significance
2000/12/13	-	-	-	-	-	-	28	-
2000/12/15	76.0	13042	4.9	1.35	87.3	2.3	31	95%
2001/02/19	76.0	519	2.9	0.64	-9.5	6.5	17	95%
2001/02/23	84.0	19526	5.3	1.01	-20.5	3.1	27	95%
2001/03/17	77.1	1384	5.6	0.68	-16.5	6.1	32	95%
2001/11/24	78.0	2303	4.9	0.46	-23.4	1.6	21	95%
2001/11/26	78.0	269	5.8	0.19	24.3	6.3	30	95%
2002/01/22	78.0	1052	6.1	0.59	-15.9	1.1	41	95%
2002/01/31	77.1	5505	4.3	0.32	-16.6	2.9	21	95%
2002/02/09	78.0	11100	3.4	1.34	-48.5	8.0	18	95%
2002/02/11	78.0	310	3.6	0.37	-28.8	1.2	25	95%
2002/03/03	78.0	1338	1.5	0.25	-14.0	19.2	8	90%
2002/03/05	80.1	2831	4.3	0.79	-28.3	6.9	26	95%
2002/03/06	80.1	2501	8.5	0.35	-24.7	0.9	37	95%
2002/03/07	-	-	-	-	-	-	37	-
2002/03/10	78.0	475	5.8	1.17	-19.0	7.5	28	95%
2002/03/11	82.0	6039	6.4	0.67	301.4	3.4	33	95%
2002/03/12	81.0	8798	4.9	0.48	-10.0	6.8	26	95%
2002/03/13	78.0	362	5.8	0.80	-13.3	3.7	34	95%
2002/03/14	80.1	3182	5.3	1.00	-28.3	11.7	27	95%
2003/01/25	78.0	16974	6.7	0.40	-15.3	1.6	40	95%

from 0.2 to 1.4 km, with an average of 0.7 km. Downward propagating harmonics are seen on 16 of the nights. Wavelengths vary from 9.5 to 48.5 km, with an average of 20.8 km. Following Collins and Smith [2004], these wave parameters are plotted in Figure 3.14.

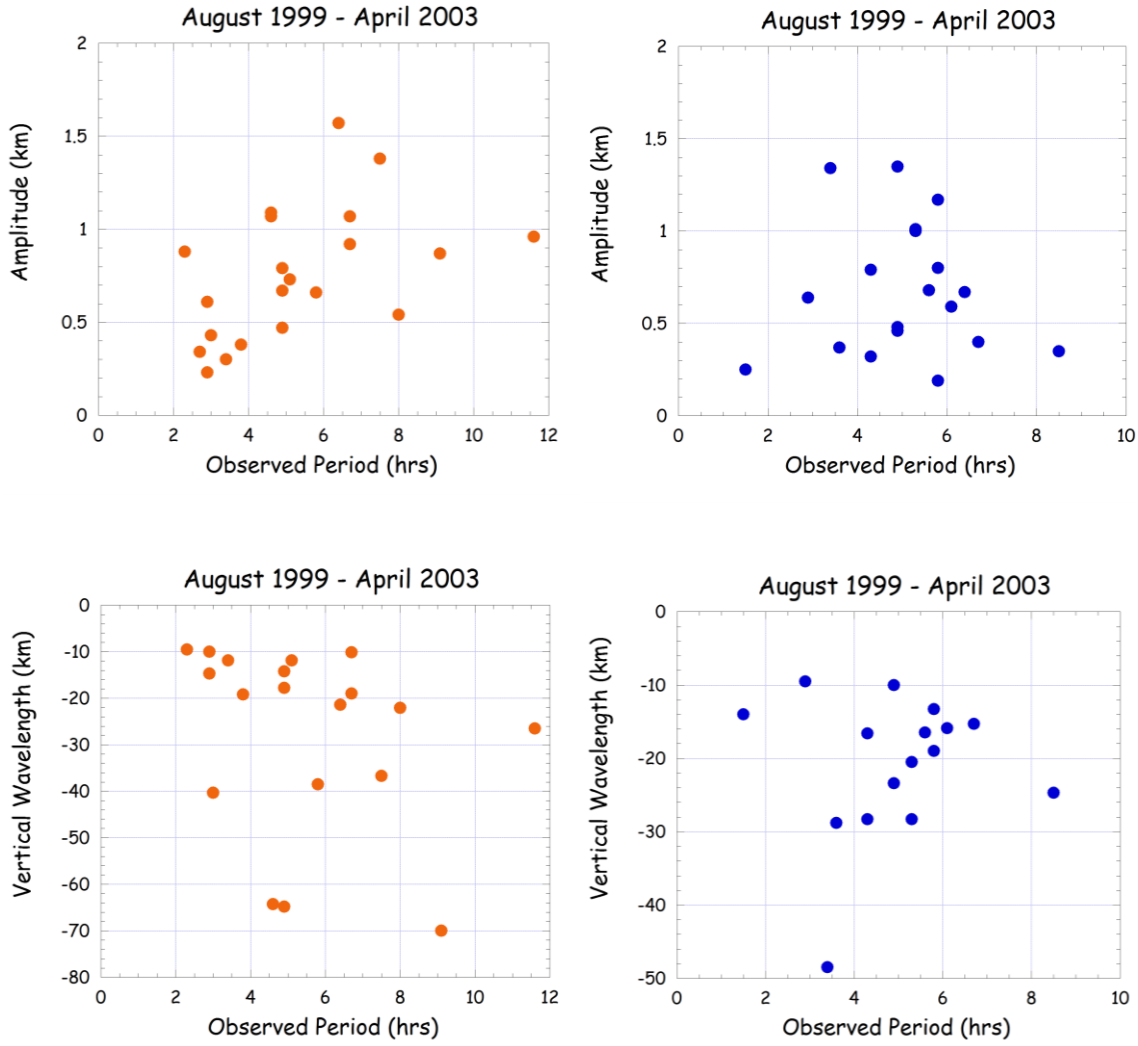

Figure 3.14 Observed characteristics of gravity waves in Na (left) and Fe (right) at LRL-PFRR. Plots show amplitude vs. period (top) and vertical wavelength vs. period (bottom). Only negative vertical wavelengths are shown; a few fit positive (see text).

The results of fitting Na periods to the Fe contours for each night are tabulated in Table 3.6. In this case, vertical wavelengths cannot be estimated for five of the nights. For the 16 nights that remain, downward propagating harmonics are present on 13 nights. The vertical wavelengths vary from 8.5 km to 42.5 km, with an average of 21.6 km.

Table 3.6 Fe contours fit to Na best fit period

Date	Period (h)	Altitude (km)	Wavelength (km)	SNR	Points	Significance
2000/12/15	4.6	74.1	92.2	2.1	31	95%
2001/02/19	2.7	76.0	-9.8	5.7	17	95%
2001/02/23	6.7	83.1	-8.5	2.2	27	95%
2001/03/17	4.9	79.0	-18.1	3.9	32	95%
2001/11/24	6.4	78.0	-25.7	5.7	21	95%
2002/01/22	11.6	78.0	-42.8	0.4	41	50%
2002/01/31	3.0	78.0	-17.0	2.0	21	95%
2002/02/09	4.6	75.0	-37.6	4.2	18	95%
2002/02/11	5.8	78.0	-23.8	0.7	25	50%
2002/03/03	2.9	77.1	-15.6	112.6	8	95%
2002/03/05	4.9	79.0	-23.6	6.4	26	95%
2002/03/06	9.1	80.1	-24.4	1.1	37	95%
2002/03/07	7.5	80.1	336.5	0.6	37	90%
2002/03/10	6.7	81.0	-23.7	8.1	28	95%
2002/03/11	8.0	81.0	531.9	2.1	33	95%
2002/03/12	5.1	81.0	-10.1	6.8	26	95%

3.5. Conclusions

In our study of these 21 nights of simultaneous Na and Fe data, we see a high degree of correlation between the motions of the two metals; 14 of the nights have maximum correlations of 0.85 or greater. By tracing constant density contours on the bottom side of the layer at roughly the same altitudes in both layers, we are able to see motions that, since they are common between the two metals, are caused by an physical perturbation. Our hypothesis is that gravity waves are the cause of these oscillations in the mesosphere. To test this hypothesis, we fit the smooth bottom-side contours in both metals to a harmonic wave function for all observations in our dataset. The best fit period in a particular layer was then fit to all the smooth contours in that layer, and the phase progression with height used to calculate the vertical wavelength. We find that the harmonic fits on most of the nights (19 in Na, 16 in Fe) exhibit the features expected from gravity waves, with downward propagating harmonics having wavelengths on the scale of 10-40 km. These results are similar to the results from a similar study by Collins and Smith [2004]. However, in this study we have two metal layers to compare, and we also find the correspondence between the Na and Fe layers described by Yi et al. [2008]. Our wave fits are also similar between the two metals on most of our nights, supporting our hypothesis that gravity waves are the cause of the oscillations. Thus, we conclude with more evidence that the mesospheric metal layers can be used as a tracer for wave motions near the mesopause.

4. Nickel Observations

With our understanding and instrumentation of resonance lidar established, we began our search for the mesospheric nickel (Ni) layer. To our knowledge there are no published lidar measurements of the Ni layer. First, we discuss the planning and staging for observations at the most promising wavelength. We follow this with an estimation and simulation of the signal expected from the Ni layer. We then describe our five nights of observations near the resonance line. We highlight our most promising measurements and present our best estimate of the Ni layer. Summarizing our search, we show a simulation of what signal we should obtain based on updated information about the efficiency of our lidar system from our experience. We conclude with a series of simulation experiments to determine what adjustments to our system might make a more confident detection of the Ni layer possible.

4.1. Spectroscopy of Ni

To begin planning for our detection of Ni, a suitable wavelength for resonance interaction had to be chosen. Metal layers in the upper atmosphere consist of neutral, unexcited atoms. Thus, only transitions involving the ground state would be viable for resonance lidar. We consulted the online NIST Atomic Spectra Database [NIST, 2012] and identified all such transitions. It happens that all the transitions available occur at wavelengths in the ultraviolet. As discussed in section 2.2, we evaluate the strength of a transition by the line-integrated absorption cross-section, σ_0 (Equation 2.15). The NIST database lists the values of wavelength of the transition, Einstein A coefficient of the transition, and degeneracy of the upper and lower states, which we then used to calculate σ_0 for each line. A plot of the line-integrated absorption cross-section for all these lines is shown in Figure 4.1.

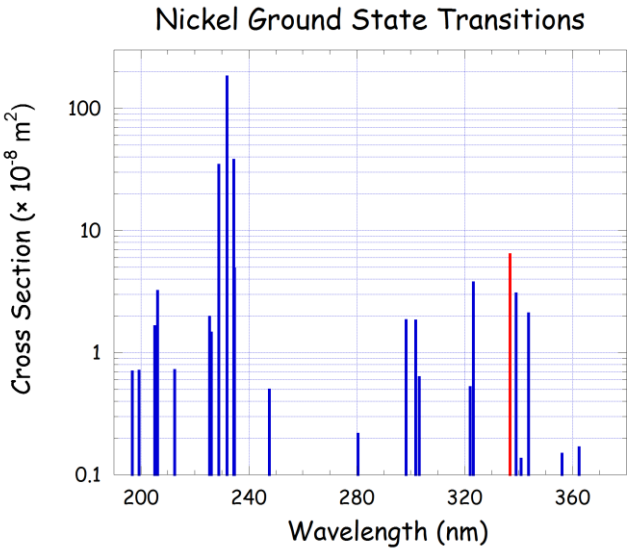

Figure 4.1 Ground state transitions in neutral Ni atoms by wavelength. Strength of the lines is given by the line-integrated scattering cross-section (Eq. 2.15). The chosen 337 nm line is shown in red. The wavelengths are air wavelengths at STP.

Because of the short wavelengths of these lines, two problems present themselves: the dye laser performance and absorption by the ozone layer. Our dye laser cannot produce light at wavelengths shorter than the pumping wavelength of 308 nm. Due to ozone absorption, the atmospheric transmission drops off significantly at wavelengths shorter than 320 nm [Berk et al., 2006] – a factor of 100 between 320 and 300 nm (Figure 4.2). This effectively limits our choice of lines to those with wavelengths longer than 320 nm. The best candidate in this case is the line at 336.957 nm, henceforth referred to as the 337 nm line.

Ni has a ground-state electron configuration of $1s^2 2s^2 2p^6 3s^2 3p^6 3d^8 4s^2$; it is a transition metal with atomic number 28, very close to that of iron (Fe). As such, its chemical properties are very similar to that of Fe. The electron configuration levels in this transition are from $3d^9(^2D)4p$ to $3d^8(^3F)4s^2$ [NIST, 2012]. As the Ni line is a simple lineshape, which we assume to be similar to that of Fe, the effective scattering cross-section is the same as that given in

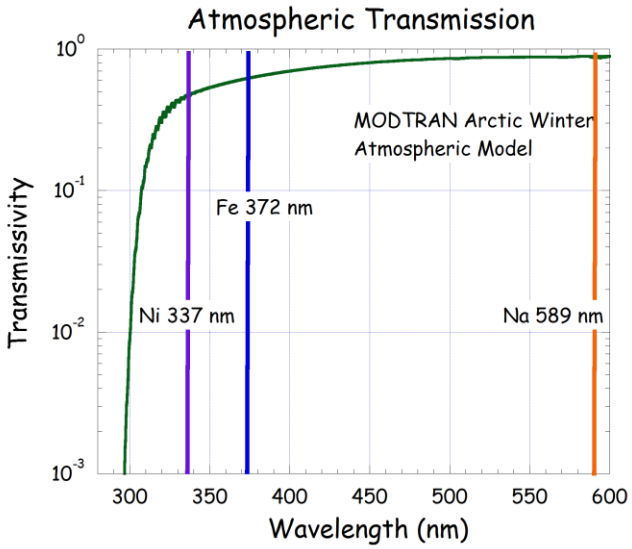

Figure 4.2 Atmospheric transmission in the near-UV from the MODTRAN5 Sub-Arctic Winter Atmosphere model [Berk et al., 2006]. The great increase in absorption is mostly a result of the ozone layer.

Equation 2.19. The absorption line parameters from the NIST database for the 337 nm Ni line are given in Table 4.1 along with the parameters for Na and Fe as given in Table 2.1 for comparison. Observations will be made more difficult by the fact that the Ni line is weaker than that of Na or Fe (i.e., 4% of the Na cross-section and 58% of the Fe cross-section).

4.2. Choosing the laser dye and receiver filter

To choose the dye for use in the dye laser, we had several constraints. The dye must be excitable by the XeCl excimer laser at 308 nm, and give a lasing wavelength range that includes 337 nm. Also, for ease of operation the

Table 4.1 Resonant lines used for observations

Line	λ (nm) (Air)	A_{21} (10^7 s^{-1})	g_1	g_2	σ_0 (10^{-7} m^2 Hz)
Na 589 nm (D2)	588.995	6.16	2	4	17.0
Fe 372 nm	371.993	1.62	9	11	1.09
Ni 337 nm	336.957	1.80	9	7	0.632

dye must dissolve in dioxane or methanol, and should have the maximum efficiency possible. The dye that best fit our needs was found to be p-Terphenyl, which has a maximum lasing efficiency of 8% at 343 nm and a range from 332-360 nm [Brackmann, 1997].

For our receiver, we used a 3 nm bandwidth filter from Omega Optical centered at 337 nm with a central transmissivity of about 55%. The transmission spectrum of this filter as provided by the manufacturer is shown in Figure 4.3.

Testing the laser's performance on p-Terphenyl dye, we took spectra at the peak of the dye, 343 nm, and at our target wavelength for Ni, 337 nm (Figure 4.4). The stimulated emission is clearly visible at all four wavelength settings. The spontaneous emission is also visible between approximately 338 nm and 346 nm. The amplitude of the laser line at the Ni resonance wavelength (337 nm) is about half that at the wavelength of the peak fluorescence of the dye (343 nm). Overall, the performance of the dye is as we expect for a dye laser so far into the UV.

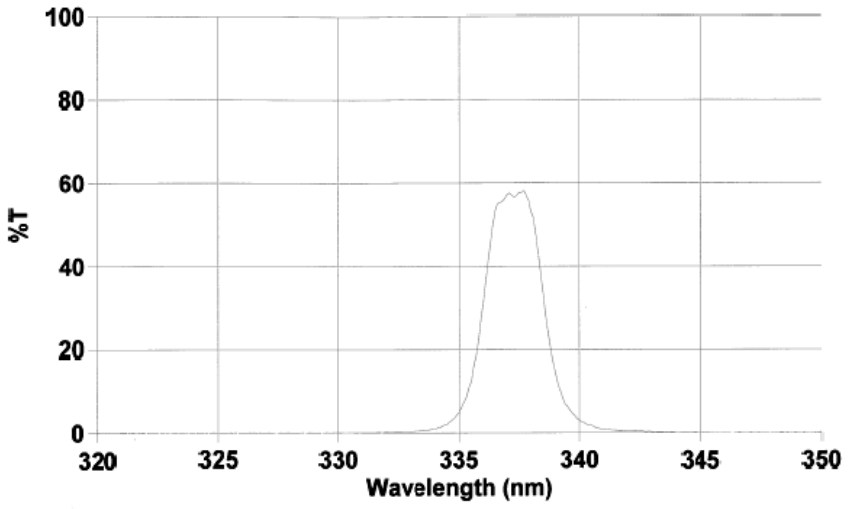

Figure 4.3 Transmission spectrum of our 337 nm receiver filter. Courtesy of Omega Optical.

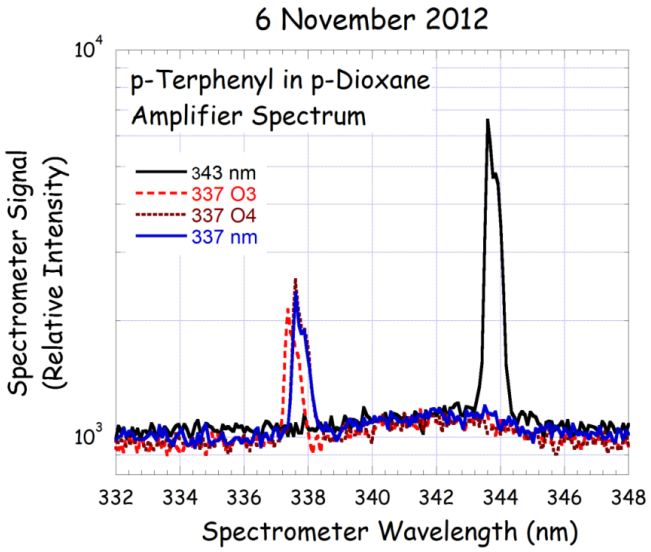

Figure 4.4 Spectra of the excimer-pumped dye laser beam on p-Terphenyl dye at the peak of the dye (343 nm) and at the Ni wavelength (337 nm, in grating orders 8 (default), 3, and 4).

Since a diffraction grating in the dye laser oscillator selects for the lasing wavelength, the efficiency of the oscillator depends on the grating order and angle of incidence. A spectrum in the grating is produced in multiple orders, and the most efficient order is the smallest that is available [Halliday and Resnick, 1981]. Because of the physical geometry of the oscillator, the grating can only move over a small range of wavelengths and so it must employ multiple orders for the entire range of wavelengths possible in the laser. If the wavelength of interest is near the edge of a grating order change, then the angle of incidence on the grating is high (i.e., the light grazes the grating surface) and more the reflection is less efficient. As the grating angle of incidence increases the reflection coefficient decreases. To check that we were getting maximum power at 337 nm, we made measurements of the spectrum at the default order, 8, as well as orders 3 (grating setting 898 nm) and 4 (grating setting 674 nm). We found that the lower orders did not increase the laser power, as the grating is at a fairly large angle at 337 nm; thus the reflection from the grating is fairly high.

4.3. Simulation of Ni lidar observations

As the resonance lidar system at LRL-PFRR has been used in the past to conduct reliable measurements of Fe, we estimate the appearance of the Ni layer by comparing the properties of Fe and the properties of Ni. Ni and Fe are similar elements, being close on the periodic table, and both metal layers are assumed to originate from meteoric ablation. Both are transition metals, with Fe having atomic number 26 and Ni atomic number 28. More importantly, both have their optimum line for resonance lidar observations in the ultraviolet, with Fe at 372 nm and Ni at 337 nm. We test our simulation using sodium (Na) measurements to simulate iron measurements. Parameters specific to the metals being measured are listed in Table 4.2.

4.3.1. Estimation of Ni signal

The power received by the lidar receiver is determined by several factors in the lidar equation, some of which depend on properties related to the particular element being observed. Therefore, to simulate the lidar signal from the Ni layer, or Ni profile, we ratio each factor in the lidar equation based on the properties of Ni to those factors based on the properties of Fe. This procedure results in a scale factor that we can apply to an observed Fe layer to determine the expected profile.

Table 4.2 Parameters of the lidar equation specific to the observed metals

Element	Z	m_a (amu)	λ (nm)	σ_0 (m^2 Hz)	ρ_m (%)
Sodium (Na)	11	23.0	588.995	1.70×10^{-6}	0.6
Iron (Fe)	26	55.8	371.993	1.09×10^{-7}	11.5
Nickel (Ni)	28	58.7	336.956	6.32×10^{-8}	1.5

As we discussed in Chapter 2 the lidar equation can be written as follows:

$$N_s(z) = [\eta T^2]\left[\frac{E_L R_L \Delta t}{hc/\lambda_L}\right][C_{eff}(\lambda_L)\rho(z)\Delta z]\left[\frac{A_R}{4\pi z^2}\right] \quad (4.1)$$

where each of the terms has been presented in Equation 2.7. Of these factors, the receiver efficiency is expected to be the same between the two metals, as the response of the mirrors and detectors is expected to be similar between the two wavelengths, and the transmission of our filters for the two wavelengths are similar. The altitude of the Ni layer is expected to appear at a similar altitude to that of Fe, because meteoric ablation, which creates the layers, occurs in a particular altitude range. The remaining performance factors (i.e., Laser power, Atmospheric transmission, Number density, and Effective cross-section) are discussed as follows.

Laser power – P_L

In a pulsed dye laser, the power (P_L) is given by the product of the pulse energy (E_L) and the pulse repetition rate (R_L). The power changes according to the dye efficiency and the position of the desired line within the spectrum of the dye. Prior to actually operating the dye laser with the proper dye for Ni at 337 nm and measuring the output power, we can only estimate the power ratio between the configuration for Fe and Ni using the dye efficiencies. Fe was observed with QUI dye, which has a peak efficiency of 11% at 390 nm [Brackmann, 1997]. For Ni observations, p-Terphenyl has a peak efficiency of 8% at 343 nm. We take the ratio of these two percentages to provide a rough estimate of the power ratio. The Fe line at 372 nm is located in the wings of the QUI spectrum, while the Ni line at 337 nm is closer to the peak of the p-Terphenyl spectrum, so our estimate of the power scaling is conservative.

Atmospheric transmission – T

The transmission of the atmosphere in the wavelength regime of interest is largely determined by ozone, which increases its absorption very quickly toward shorter wavelengths. This is of course assuming an atmosphere perfectly clear of clouds, ice particles, and aerosols during the observations. Using the MODTRAN simulation of atmospheric transmission for the Arctic winter atmosphere, we obtain a transmission value of 61% at 372 nm for Fe and 47% at 337 nm for Ni [Berk et al., 2006].

Number density – $\rho(z)$

Since we assume that the metal layers in the upper atmosphere are produced by meteoric ablation, we estimate the relative abundances of the metals by their relative abundances in meteorites found on the Earth's surface. This method also assumes that the chemistry of Ni is similar to that of Fe, leaving a similar percentage of atoms in the upper atmosphere as free neutral atoms instead of part of other compounds. As introduced in Chapter 1, the meteoric abundances by weight are 11.5% for Fe and 1.5% for Ni [Plane, 1991]. The ratio of these abundances must be scaled by the inverse of the ratio of their atomic weights in order to obtain number density. The atomic weight of Fe is 55.8 amu, and the atomic weight of Ni is 58.7 amu.

Effective cross-section – $C_{eff}(\lambda_L)$

As discussed in section 2.2, the line-integrated absorption cross-section gives a measure of the absorption strength of each atomic transition. Using the line-integrated absorption cross-section to compare the two elements assumes that the lineshapes of Fe and Ni are similar and that the laser linewidth is roughly equivalent to that of the atomic absorption line in both

cases. From Table 4.1, the values of σ_0 are 1.09×10^{-7} m^2 Hz for Fe and 6.33×10^{-8} m^2 Hz for Ni.

Combining all the above ratios, we obtain the ratio of the expected resonance lidar signal between Fe and Ni:

$$\frac{N_{S\,Ni}}{N_{S\,Fe}} = \frac{8\%}{11\%}\left(\frac{47\%}{61\%}\right)^2\left(\frac{1.5\%}{11.5\%}\frac{55.8}{58.7}\right)\frac{0.633}{1.09} = 0.031 = 3\% \qquad (4.2)$$

Thus, the expected signal from the Ni layer would only be 3% of the signal expected from the Fe layer.

4.3.2. Resonance layer simulation program

To model the expected signal from the Ni layer, we developed a simulation program using the Interactive Data Language (IDL) that would take into account all the differences between the observed mesospheric metals and enable simulation of one species from observations of the other. Thus it is possible to simulate Fe from Na, Ni from Fe, or Ni from Na. The model takes as input measurements from past observations of a mesospheric metal using this lidar system, and then decomposes the combined signal into three parts (described in Chapter 1): background, Rayleigh signal, and resonance layer. The background signal per altitude bin is taken as the average of the signal from 200 to 300 km – a large range to avoid statistical uncertainty. To illustrate the procedure, we simulate an Fe profile from Na data taken at LRL-PFRR, then compare to Fe data taken at LRL-PFRR to evaluate the accuracy of the simulation. Using Na data from the night of October 23, 2012, we simulate the Fe data that was taken on October 28, 2008. The original signals from both observations are shown in Figure 4.5.

The Rayleigh signal is taken from 25 km up to the height where the signal drops below 3σ (three standard deviations) away from the background,

which in this case 52.7 km. Assuming that photon counts follow Poisson statistics, the standard deviation is equal to the square root of the mean. Thus the cutoff value we are using for signal is three times the square root of the background. The lower limit is set so as to be above the blanking (discussed in Chapter 1). Using this robust portion of the Rayleigh signal, the simulation fits the data to an exponential curve, which is then used to model the Rayleigh profile from 25 km to 300 km.

The region in which the resonance layer is expected to be found is set in the simulation to be between 70 and 110 km. The resonance signal is then identified in this region where the resonance signal is greater than 3σ above the background signal. In this case the altitude range where the resonance signal dominates is 70.0 to 105.9 km. The shape of the mesospheric metal layers can be described as an asymmetric Gaussian, where the topside has a larger RMS width than the bottomside. In our simulation, the resonance layer is divided into upper and lower parts around the peak of the layer. These parts are separately mirrored and modeled as a Gaussian, and the resulting curves are used to model the layer as a single asymmetric Gaussian. The background, Rayleigh, and resonance curve fits are then added together to make a complete modeled profile. This composite model profile is shown in Figure 4.6 with component plotted separately and overlaid onto the original measured profile.

Using the modeled lidar profile, we scale the component parts to simulate an expected lidar profile under different conditions as we discussed earlier in section 4.3.1. The background signal is scaled as desired to account

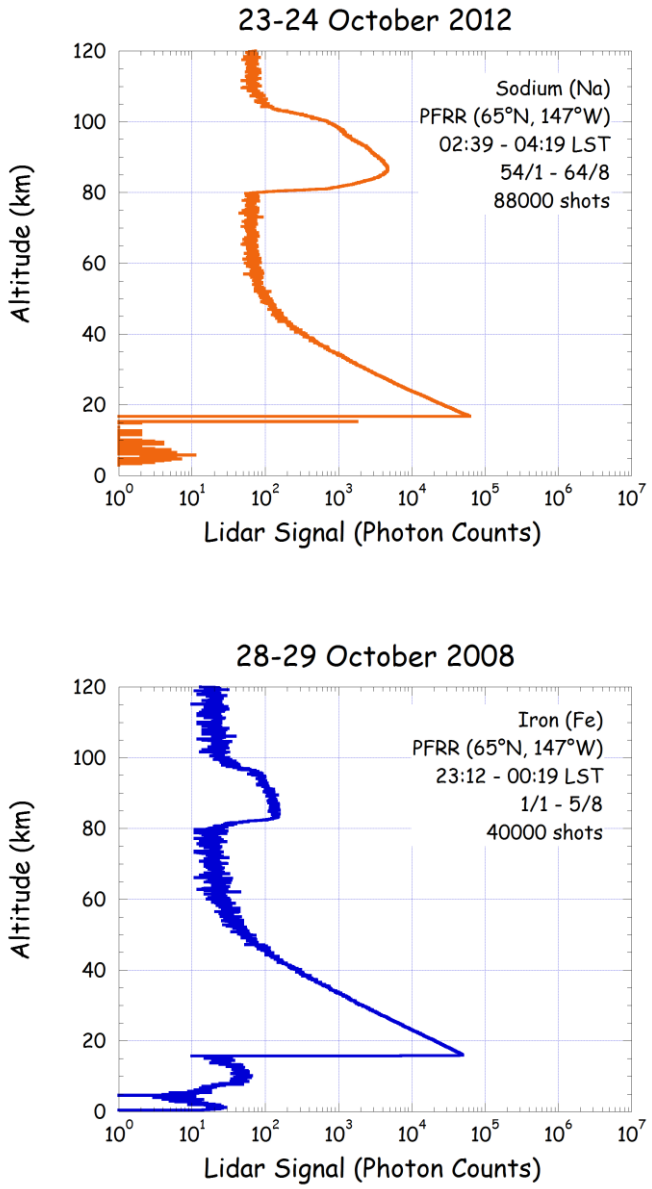

Figure 4.5 Average profiles of Na (top) and Fe (bottom) data taken at LRL-PFRR. The sodium data is used to simulate the Fe profile using the simulation program.

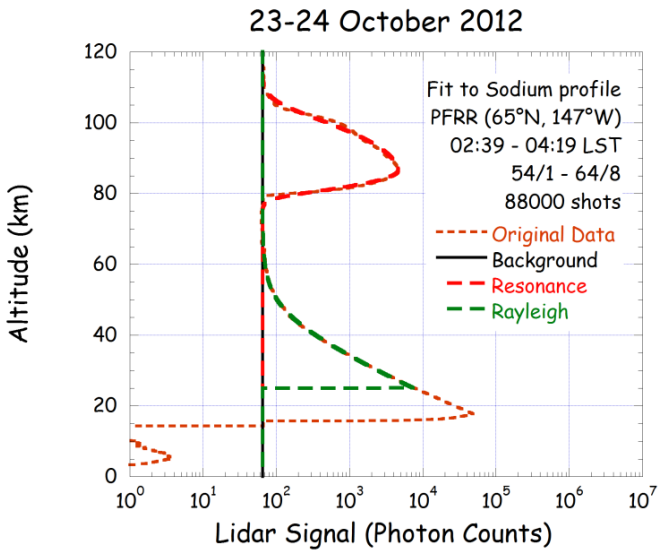

Figure 4.6 Sodium profile parts modeled by the simulation program.

for differing amounts of sky illumination (e.g., moonlight, aurora). The Rayleigh signal scales with wavelength, according to the λ^{-4} dependence of Rayleigh scattering. For example, the Rayleigh signal increases by a factor of 6.3 when the wavelength changes from 589 nm to 372 nm. The resonance signal scales with effective cross-section and metal number density. Both the Rayleigh and resonance signal are also proportional to the laser power and atmospheric transmission. All three signals are proportional to the number of laser shots.

Rather than using measurements of the laser power at the beginning of the observations we can use actual Rayleigh signals to quantify the laser power and atmospheric transmission over the whole observation period. By taking the Rayleigh counts in a particular altitude range from the observations at both wavelengths, scaling for the number of laser shots in the profiles, and scaling for the wavelength dependence of Rayleigh scatter, it is possible to obtain a scale factor that more accurately relates the lidar system performance between the two wavelengths. In this simulation, we take the

Rayleigh counts between 30 and 35 km from both the data used for the simulation and data from the night for which the simulation is produced. The ratio of these counts, 0.89, is then scaled to the number of laser shots composing the data that is used for the simulation, a factor of 2.2, as well as scaled for Rayleigh scattering to the wavelength of the data used in the simulation, a factor of 0.16, to produce a scale factor of 0.31 that accounts for both laser and atmospheric effects. The simulated Fe background signal is determined directly from the Fe measurements by scaling for the number of laser shots.

To scale the resonance layer, ratios of Fe over Na are calculated for the absorption cross-sections and number densities (listed above in Table 4.2), a total factor of 0.51. These factors are multiplied together with the lidar system factor to produce a resonance scale factor of 0.16, or 16%, between Na and Fe. The modeled Na resonance layer is then multiplied by this scale factor to give a simulated Fe resonance layer. The modeled 589 nm (Na) Rayleigh profile is scaled for the wavelength dependence of Rayleigh scatter to give a simulated 372 nm (Fe) Rayleigh profile. Adding together the resonance and Rayleigh regimes to the background from the night of the simulation, we obtain a simulated Fe profile.

Since we are comparing the simulated profile to Fe measurements with 40,000 laser shots, we scale the entire simulated profile, from the 88,000 shots of the Na data. To simulate how measurements appear, we add random noise with a magnitude of the square root of the signal. The resulting simulated profile is plotted in Figure 4.7 along with the measured Fe profile. We find that the shape of the simulated layer, based on the Na layer shape, is different than that of the measured Fe layer, but this difference is expected because the simulation does not take into account the differences in shape between the layers. However, the integrated signal, calculated between 70

and 120 km, is 2.4 times higher in the simulated profile than in the measured profile. This can be explained by the manner in which abundance scaling is done in the simulation. In the simulation, atmospheric abundances of the metals are scaled by their relative abundances in meteorites. Based on the meteoric abundances, the ratio between Fe and Na is 7.9. However, as discussed in section 3.2, both metals vary in abundance by a factor of 10 over the course of a year, with the lowest abundance being in summer and the highest in midwinter. From Figure 3.3, the average column abundance ratio for the end of October, when this Na and Fe data was taken, is 2.8, with a maximum possible ratio of 4.8 and a minimum of 1.6. Taking this into account, we divide the meteoric abundance ratio by the average observed abundance ratio and obtain a discrepancy factor of 2.8 – very close to the discrepancy between our simulated Fe signals and the measurements of Fe in Figure 4.7. Thus our simulation accurately models the resonance lidar

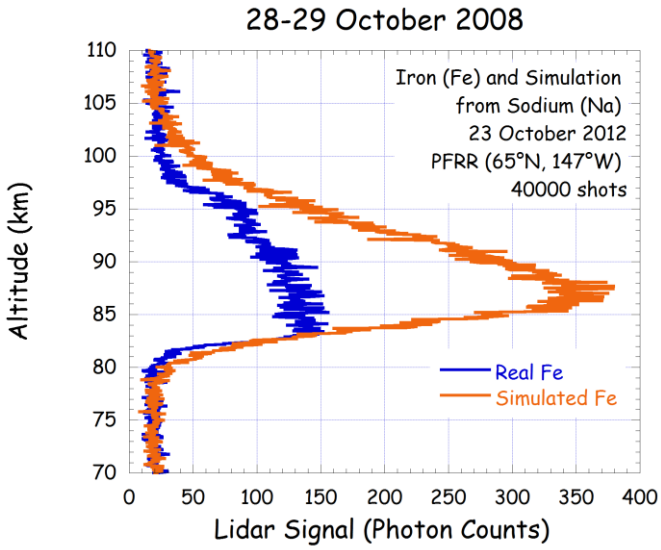

Figure 4.7 Comparison between the observed Fe profile and a simulation of the Fe profile from an observed sodium profile using the simulation program.

signals from different metal layers based on the appropriate physical and experimental parameters.

For Ni, no observation has been made as of yet to determine its abundance in the atmosphere. Therefore the only estimate that we can make must be based on meteoric composition. However, the actual abundance may vary by at least a factor of two from the simulation based on our experience with Na and Fe.

4.3.3. First-order Fe-based Ni simulation

With the simulation program working well to simulate data already taken, we made a preliminary simulation of how Ni measurements should appear. Fe data is used to simulate Ni because Fe and Ni are similar metals and the absorption line for both is in the ultraviolet. Thus, we expect the Ni signal to be similar to that of Fe, albeit of much lower amplitudes. We use the scaling factors discussed in section 4.3.1: a 3% scaling factor for the resonance layer and a 148% scaling for the Rayleigh profile.

For this simulation, we use the Fe data from October 28, 2008, consisting of 40,000 shots. The scaled profile is shown in Figure 4.8, without any noise. This is simply a scaling of the modeled Fe profile. Note how even without noise, the modeled Ni signal is barely visible on the log plot showing the entire profile (top panel). It is necessary to zoom in on the resonance range to see the layer (bottom panel).

To simulate how Ni measurements appear, we added noise to the scaled profile, shown in Figure 4.9 along with the original Fe profile for comparison. Again, we assume Poisson statistics, where the amplitude of the noise is equal to the square root of the signal. Notice that the layer is barely visible above the noise. Without prior knowledge that the layer is there, one may simply dismiss the slight rise in signal as a large piece of noise. In

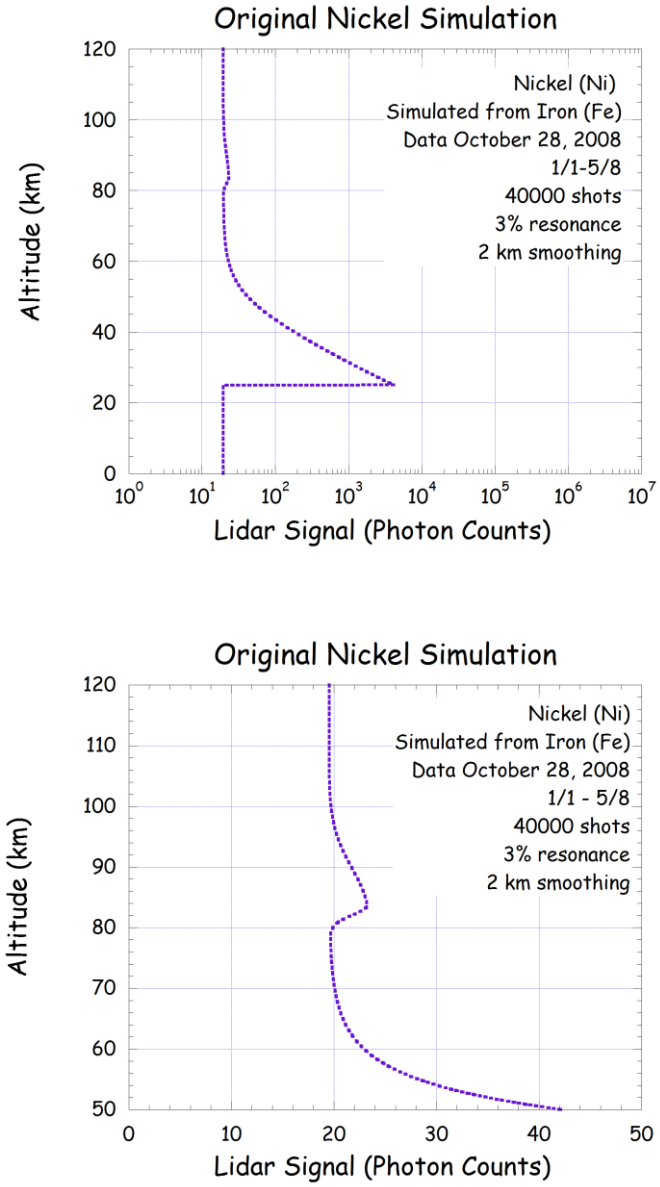

Figure 4.8 Simulated Ni profile without noise based on original estimation of the Ni signal before observations. The top panel shows the entire profile, while the bottom panel shows a close-up of the resonance layer.

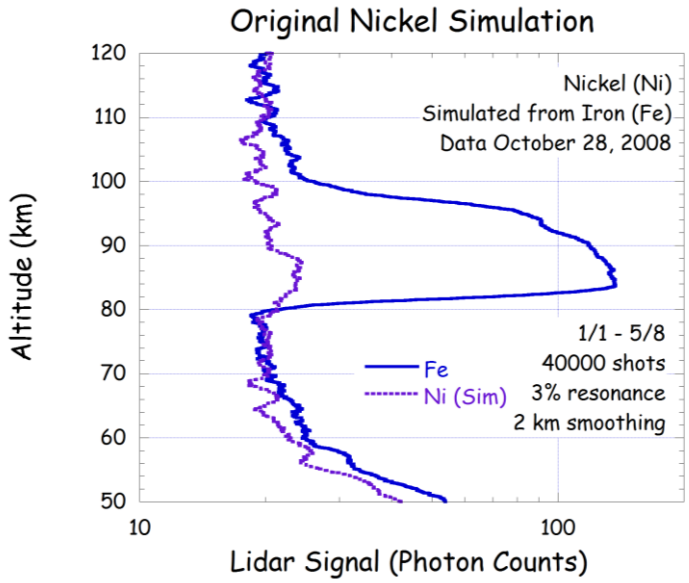

Figure 4.9 Simulated profile of Ni with noise added. The measured Fe profile is plotted for comparison.

addition, this simulated profile is made of 40,000 shots – much more than any single profile that we would view in the data acquisition program during observations. A single profile, made up of between 500 and 2400 shots, would give even less confidence in the signal; thus we do not expect to be able to see the nickel layer in real time during observations, as we do with Na and Fe. It is necessary to integrate together many profiles to reliably detect the Ni layer.

This simulation of the Ni signal is based on estimates of laser power, atmospheric transmission, and atmospheric abundances. However, the specific values are liberal estimates. In practice, with a wavelength so far into the UV, the maximum dye pumping efficiency may not be achieved in our laser, and the atmospheric transmission could easily be lower than expected from the model due to absorption and scattering by water vapor, ice crystals, and/or aerosols. Furthermore, abundance estimates are based on the abundances in meteorites, while the actual atmospheric abundance is

unknown. Thus detection of Ni may be even more difficult than estimated in this simulation. Another difficulty in detecting Ni arises because of the uncertainty as to the exact wavelength at which the line will appear.

To make matters even worse, the wavelength of the Ni line in the sky is not necessarily the same as the wavelength setting on the grating in the laser due to calibration issues and thermal effects, as discussed in section 2.7 for Na observations. Thus it is necessary to find the precise resonance laser wavelength of the line before taking observations. For Na, we have a terrestrial source of emission in the hollow cathode tube, which can be used to precisely identify the laser wavelength for observations. However, for other metals, such as Fe and Ni, we do not have such a laboratory emission source. Therefore, it is necessary to search over a range of wavelengths to find the resonance line. For Fe the lidar signal is large enough that the operator can tune the laser based on the echoes from the iron layer in real time. Based on Fe observations using this system, the resonance line could be as much as 50 pm longer than the corresponding laser wavelength. The laser wavelengths are plotted in Figure 4.10 with the expected air wavelength at STP obtained from the NIST database.

Because of the very low signal expected from Ni, we need to observe at the peak wavelength of the absorption line so as to maximize the signal. This poses a significant observational challenge. We must first scan through a range of about 50 picometers to find the Ni line in the sky, while we must also integrate over a long period in order to reliably discriminate between the wavelengths where we detect the layer and those where we do not.

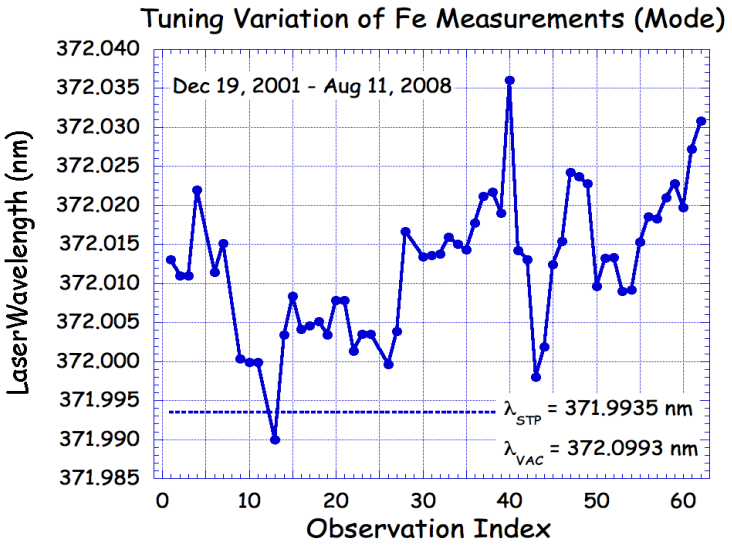

Figure 4.10 Grating settings on the excimer-pumped dye laser when tuned to the Fe 372 nm line for Fe observations on different nights.

4.3.4. Layer signal significance technique

While the operator can use visual inspection to optimize lidar measurements of Na and Fe in real time, the lower Ni signal preclude such an effort. To allow detection of the Ni layer, we developed a formal quantitative approach using the signal-to-noise ratio (SNR) of our measurements over the altitude range of the metal layers. The signal is defined as the lidar signal over the altitude range of the metal layers ($N_{S,R}$). The noise is defined as the uncertainty in that signal. The signal is determined as the difference between the total signal (N_{TOT}) and the background signal (N_B). We define the noise as the standard deviation in the signal. These signals are statistical in nature and described by Poisson statistics, thus the standard deviation is estimated as the square root of the expected signal. In our scans of wavelength searching for the Ni layer, we take one set of data at each wavelength, and then evaluate the SNR for each set. For a night of data, these SNR values could be plotted as a function of.

set number. These plots would be set-based significance plots, as they show the significance of any perceived signal from a layer at that wavelength. This measure would help distinguish signal from noise. To calculate the SNR, we calculate the average counts per bin (bin width 0.075 km) for 80-100 km (signal range) and 200-300 km (background range). We then subtract the counts in the 200-300 km (background) range from the counts in the 80-100 km range to calculate the signal. We calculate the standard deviation, taken as the magnitude of the noise, by the square root of the counts in 80-100 km added to the background. Dividing the signal by the standard deviation, we produce the SNR, as follows:

$$SNR = \frac{N_{TOT}(80 - 100\ km) - N_B(200 - 300\ km)}{\sqrt{N_{TOT}(80 - 100\ km) + N_B(200 - 300\ km)}} \qquad (4.3)$$

For the Fe profile from 28 October 2008 with 40,000 shots, we obtain an SNR value of 120. Scaled to 5,000 shots, assuming the Fe layer and atmospheric conditions remain unchanged, the SNR value decreases to 42. The SNR for the simulated nickel profile is 5.9 for 40,000 shots and 2.1 for 5000 shots. In both cases the SNR is scaled by 2.8, the square root of eight (i.e., the ratio of 40,000 to 5,000).

For the simulated Ni data, Figure 4.11 demonstrates the possible range of SNR values for measurements where the lidar is tuned to the resonance wavelength for the Ni line. These 50 sets were generated by taking the same scaled profile and separately adding random noise in 50 different instances, allowing for many different arrangements of the noise. All the simulated "sets" actually contain the simulated Ni layer. These results in this case show sets of 5000 shots with the Ni layer present that yield a SNR between -0.5 and 3.9, with an average value of 2.0. Since the layer will appear in real data during a wavelength scan at only one wavelength, the SNR that will appear at that point may be anywhere within the above range

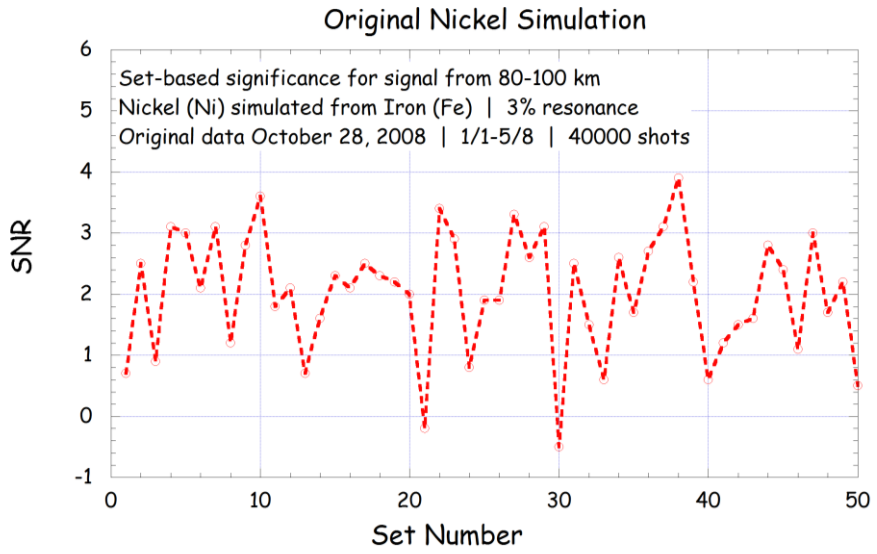

Figure 4.11 Significance plot of 50 simulated Ni profiles of 5000 shots each. Ni simulated from original estimate of Ni signal. Noise added separately in each profile.

of values, assuming the signal received from the Ni layer is as modeled in the simulation. To ascertain how well this may be distinguished from the noise of sets with no layer present, we ran the simulation without signal from the simulated Ni layer (Figure 4.12). In this case, the SNR varied from -2.7 to 2.4, with an average value of -0.2.

Examining these simulation results, we see that the SNR of the data including the resonance signal is, on average, about a value of 2 higher than the data excluding the signal, but about half of the possible range of SNR for data including the signal overlaps the range for data excluding the signal. Essentially, these results show that it may not be possible even under the best of conditions to clearly identify the presence of the Ni line in a wavelength scan at this resolution (5000 shots per set). The best this tool will allow is to indicate possible wavelengths for further investigation.

To investigate individual sets with a high SNR for more evidence of the Ni layer, we also use a similar SNR calculation in height. Taking the photon

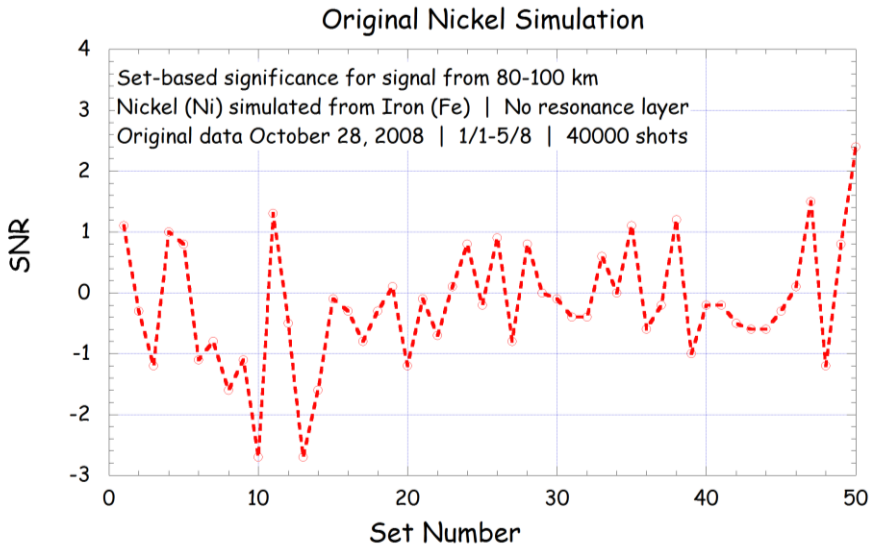

Figure 4.12 Significance plot of 50 simulated profiles of 5000 shots each at the Ni wavelength. No resonance signal present. Noise added separately in each profile.

count profile, we bin the photon counts in 5 km ranges and calculate the SNR according to Equation 4.3 for each of these bins instead of the one 80-100 km bin for the profile. We then plot the SNR with height to provide a more clear picture of any layer that may be present among the noise. Figure 4.13 shows the SNR profile for the 28 October 2008 Fe profile (top) and for the simulated Ni profile (bottom). For Fe, we see high SNR in the altitude range where the layer is located (78-102 km), making a clear outline of the layer. Below 78 km, the Rayleigh signal is also visible in the pattern of SNR. The Ni SNR profile also traces out the layer and the Rayleigh signal, although the appearance of the layer is rather angular and only has a peak SNR value of about 3 compared to the peak SNR value of nearly 80 in the Fe profile. However, the layer is much more clearly visible in the SNR profile than in the photon count profile due to noise in the latter; thus this technique can be used to provide evidence of a layer from a noisy signal.

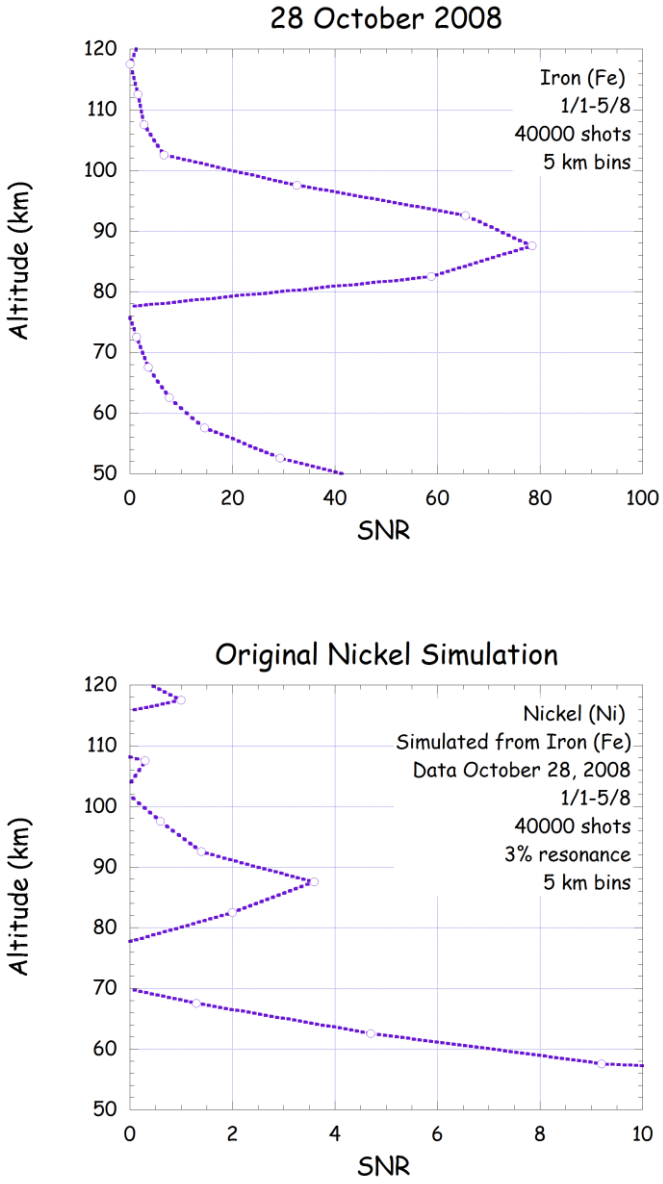

Figure 4.13 SNR in 5 km altitude bins as a function of altitude for 28 October 2008 Fe data (top) and for the Ni simulation (bottom).

4.4. Search for Ni

Between 7 November 2012 and 26 January 2013, we conducted our search for the Ni layer with 5 nights of observations (summarized in Table 4.3). Our first two nights, in November, consisted of a wavelength scan in an attempt to find the Ni line. We recurrently received high SNR (>2) in a range of a few picometers around 336.990 nm, and so our next night in December focused on this range with longer time integration, as well as a wavelength scan of the larger initial range. Once again, our highest signal was seen in this wavelength range, but not as strong. We followed this up with two more nights in January focused on our suspect range with much longer time integration, but the measurements from these nights did not yield sufficient SNR to indicate the presence of the Ni layer.

4.4.1. 7-8 November 2012

With our excimer-pumped dye laser running well on p-Terphenyl dye at 337 nm, we began our campaign to observe the Ni layer on the night of 7-8 November 2012. The excimer energy before beginning observations was 336 mJ per pulse with the laser high voltage set to 18 kV and a reprate of 5 Hz. The dye power at these settings and the grating set to 337 nm measured 0.9 mJ per pulse, and 0.12 mJ per pulse with the grating blocked to measure spontaneous emission. We took data with a high voltage setting of 22 kV and a reprate of 10 Hz.

Table 4.3 Summary of data taken during the Ni search

Night	Date	Time (LST)	Sets	Power
1	7-8 Nov. 2012	02:02 - 05:29	63	< 20 mW[1]
2	27-28 Nov. 2012	20:27 - 04:43	60	58 mW
3	20-21 Dec. 2012	18:15 - 06:13	49	81 mW[2]
4	18-19 Jan. 2013	19:39 - 05:06	25	54 mW
5	25-26 Jan. 2013	20:49 - 05:59	27	42 mW

[1] Estimated from measurement at 18 kV. [2] Enhanced power due to higher repitition rate.

Based on experience with Fe observations, we decided to start our observations at 60 pm above the Ni line at 337.017 nm and take a set of data at each wavelength in picometer steps downward until reaching the Ni line at 336.956 nm. Each of these sets consisted of 1 profile with 1000 shots. As the following significance plot shows, the highest absolute values of SNR were negative, and positive SNR values were never greater than about 1.5 (Figure 4.14). The signal from the resonance layer was about the same as that of the background. However, each set only contains 1000 shots, a fairly short time, so longer integration may help to bring out any resonance layer that is present.

4.4.2. 27-28 November 2012

We made our second search for Ni on 27-28 November 2012. Before observing this night and all remaining nights of the Ni search, we changed the dye in the laser to ensure maximum lasing efficiency in the dye. In

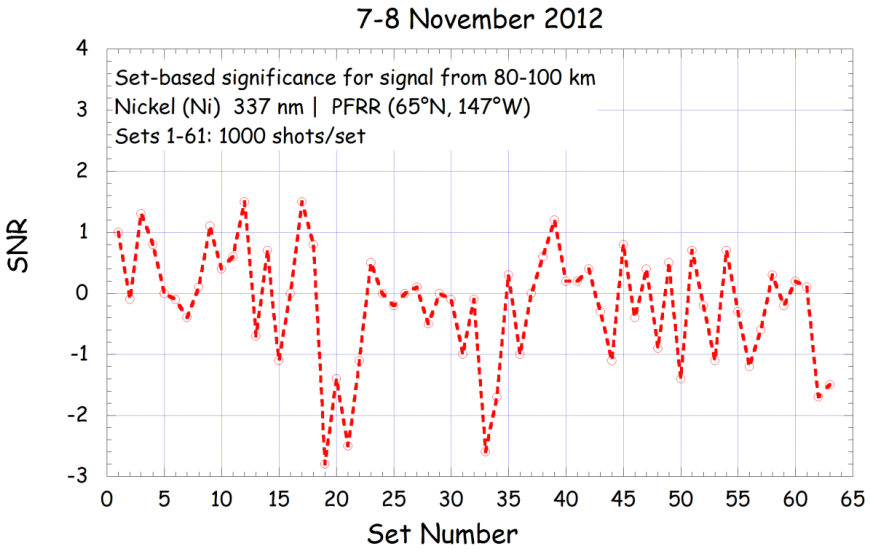

Figure 4.14 Significance plot of data taken during the Ni search on 7-8 November 2012.

addition, prior to this night we changed the gas in the excimer laser to maximize its performance. With the excimer set to 18 kV and 1 Hz, the excimer energy was 318 mJ per pulse, and the dye energy at 337 nm measured 4.2 mJ per pulse, 0.07 mJ with the grating blocked. This was a significant increase in laser power from the previous night of observations, and the low energy produced with the grating blocked indicates that nearly all of this energy was stimulated emission produced at the desired wavelength instead of wasted spontaneous emission. At excimer settings of 10 Hz and 20 kV, the excimer energy was 435 mJ. The dye energy at the peak wavelength of the dye, 343 nm, measured 9.6 mJ per pulse, while at 337 nm the energy was 5.8 mJ per pulse. Thus we see that the dye at 337 nm lases at 60% of its peak efficiency. The dye energy with the grating blocked was 0.15 mJ in both cases, again demonstrating the absence of spontaneous emission. The laser power for observations on this night was thus 58 mW at 10 Hz.

With the laser operating at a much higher power, we enhanced our signal even farther by taking data with a longer time integration. We made a new wavelength scan from 337.007 nm to 336.956 nm in 1 pm steps, with 4 profiles per set and 1250 shots per profile. All these factors combined lead to 5 times more shots and about 14 times more laser power than on 7-8 November. The longer integration time gives more statistical confidence in assessing the presence of a layer, and the increase in laser power would give more signal from any resonance layer that existed without increasing background counts. One challenge we faced on this night was the presence of a full moon, which elevated the background signal over the previous night.

After making the entire wavelength scan, a quick onsite analysis of the data showed the highest signal level for the night at set 20, with an SNR of 3.4. This set was taken at a grating setting of 336.988 nm (Figure 4.15). After the initial wavelength scan, we took 8 more sets near this wavelength,

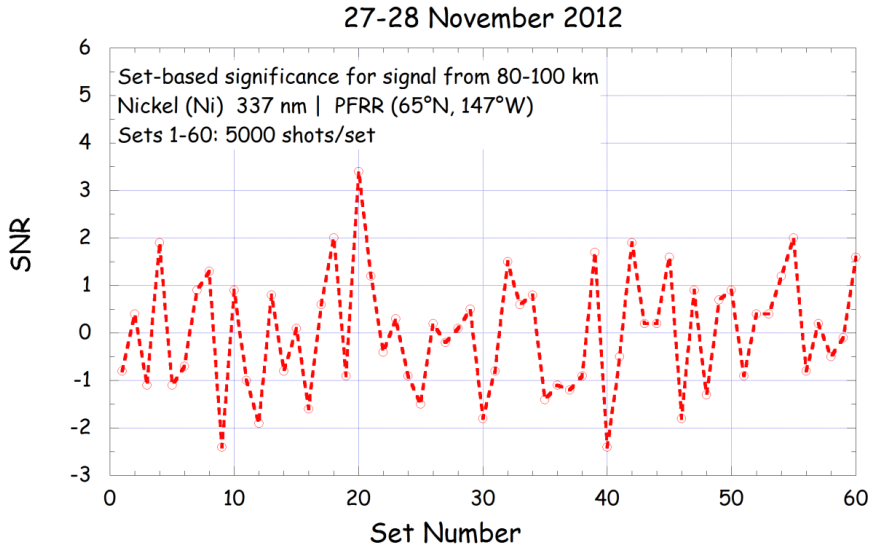

Figure 4.15 Significance plot of data taken during the Ni search on 27-28 November 2012. Set 20 at 336.998 nm shows exceptionally high SNR in the resonance range and is the best possibility for a sighting of the Ni layer.

scanning between 336.988 nm and 336.990 nm. We increased the integration time by taking 16 profiles per set, corresponding to 20000 shots per set. In this scan, set 55 at 336.990 nm obtained a relatively high SNR of 2.0. This displacement from the first prospect wavelength of 336.988 nm could be the result of drift in the laser line, as a 2 pm shift in the line over the night is well within the range of drift experienced in our Fe and Na observations with this laser.

To probe the individual sets for the presence of a layer, we examined the SNR profile with height. For set 20 at 336.988 nm, we find the SNR increasing steadily from a value less than one at 75 km to a peak of over 3 at 85 km (Figure 4.16, top). Set 55 at 336.990 nm also shows a similar layer-like pattern, but broader this time (Figure 4.16, bottom). These two sets exemplify the behavior expected if the Ni layer were detected. However, it is possible that these values could be obtained in this configuration by random noise.

Yet this was an encouraging finding, and it gave us hope that we might again detect the appearance of layer near this wavelength in subsequent observations.

4.4.3. 20-21 December 2012

Our third night of observations was taken on 20-21 December 2012. At 10 Hz and 20 kV, the excimer energy was 417 mJ per pulse, and the dye energy was 5.4 mJ per pulse at 337 nm, similar to the energy on 27 November. For observations we ran the excimer at 15 Hz and 20 kV, giving a dye laser power of 81 mW. The moon was first quarter on this night, keeping background levels elevated but not as high as the previous night. On this night we focused our attention on a narrower wavelength region around the prospective wavelengths found on 27 November. We made two scans near 336.990 nm: sets 1-17 covered 336.997-336.981 nm, set 18 returned to 336.989 nm, and sets 19-25 covered 336.992-336.986 nm. To survey the rest of the possible range again, we then made a scan over 337.007-336.998 nm in sets 26-35, and over 336.981-336.968 nm in sets 36-49.

The highest set-based significance obtained during these scans was in set 21 at 336.990 nm with an SNR value of 2.3 (Figure 4.17). Looking at the altitude significance plot for set 21, we see the appearance of a layer between 75 and 95 km (Figure 4.18). However, this high SNR value appeared during the second scan of the narrow wavelength range, but not on the first. This wavelength, 336.990 nm, was also sampled in set 8, but that time only gave an SNR value of 0.2. Several other sets gave an SNR value of about 2, but none showed a pattern of SNR with altitude that indicated the shape of a layer, but were rather random. Thus, the observations on this night did not conclusively determine the presence of the Ni layer, but served to reinforce our conclusions from the 27 November observations.

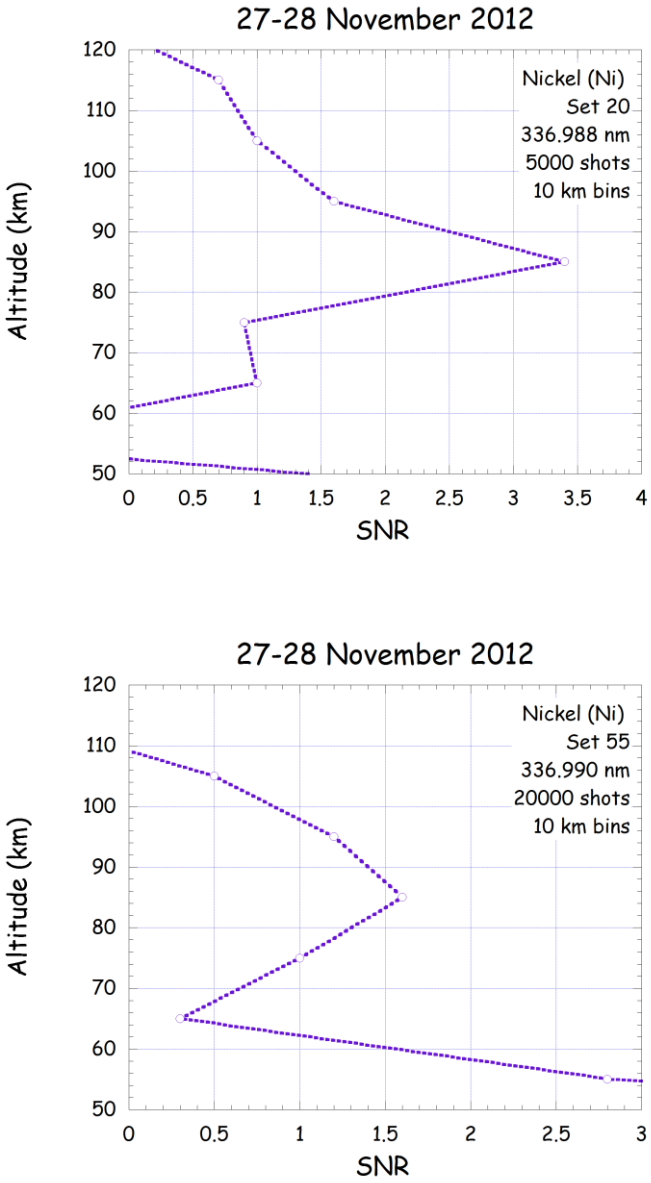

Figure 4.16 SNR in 10 km altitude bins as a function of altitude in several promising sets on 27-28 November 2012.

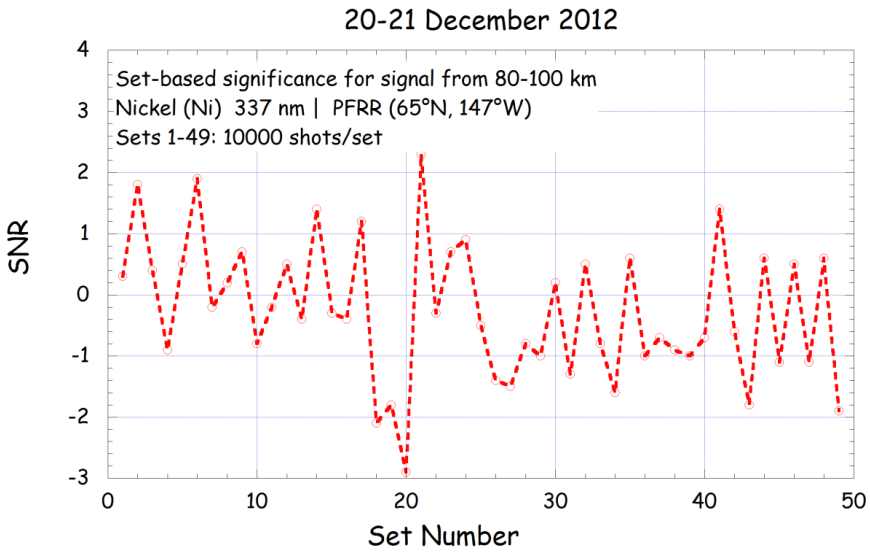

Figure 4.17 Significance plot of data taken during the Ni search on 20-21 December 2012. Set 21 (336.990 nm) shows evidence of a resonance signal.

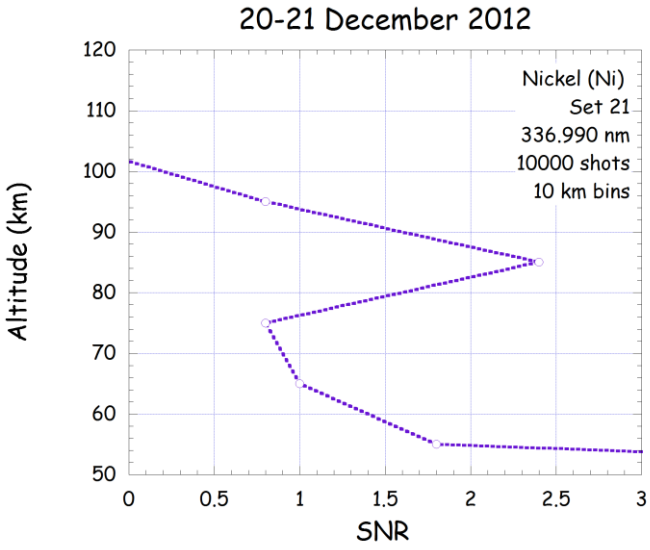

Figure 4.18 SNR in 10 km altitude bins as a function of altitude in the most promising set on 20-21 December 2012.

4.4.4. 18-19 January 2012

Before taking another night of observations we changed the gas in the excimer laser on 14 January 2013 to optimize its performance. The excimer cavity mirrors showed deposits, so we replaced the mirrors, decreasing light loss from absorption and scattering and increasing the laser output power (Figure 4.19). Prior to servicing, the excimer energy was 350 mJ per pulse at 5 Hz and 20 kV; after the changes, the energy was 426 mJ per pulse at the same operating settings.

On the night of 18-19 January 2013 we made our fourth attempt at measuring the Ni layer. Encouraged by our finding of high SNR in the region near 336.990 nm on the previous two nights, we focused our observations on that region. Our strategy was to increase our statistical confidence by taking long time integrations at each wavelength over the narrow range, and using the long night to scan this range several times, rather than hunting less thoroughly over a wider wavelength range and possibly missing the layer. Throughout the night we took data with 2400 shots per profile and 8 profiles

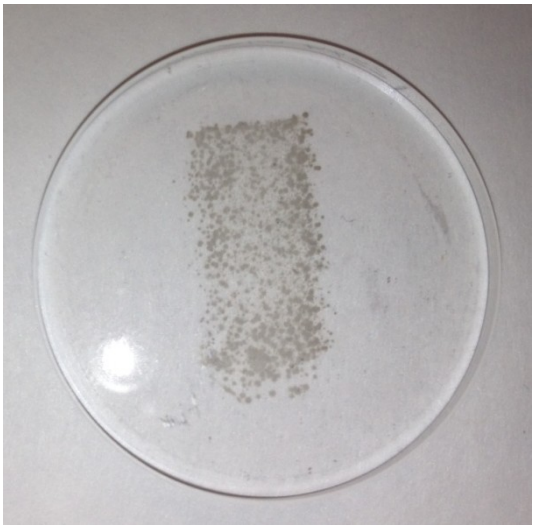

Figure 4.19 Burn marks on the excimer laser rear mirror after several nights of operation.

per set. We ran the excimer laser at 10 Hz and 20 kV. The excimer energy at these settings was 430 mJ per pulse, and the dye energy measured 5.4 mJ per pulse, or 54 mW. We scanned over the range 336.996-336.985 nm in sets 1-11, 336.990-336.986 nm in sets 12-16 and again in sets 17-21. Sets 22-25 stepped in finer precision from 336.990-336.989 nm, although in these last sets the sky conditions deteriorated so that the Rayleigh lidar, which was running simultaneously, was getting low signal.

The set-based significance for this night shows none of the sets with SNR values greater than 2 as in the previous two nights (Figure 4.20). The highest SNR value obtained is 1.3, while the lowest is -1.5. Obviously a negative SNR value is due purely to random fluctuations, so the random noise could cause an SNR as high positive as low negative. Thus we conclude that there is no evidence of signal in this data. There is a steady increasing trend in SNR over the night; this is may be due to decreasing background levels over the night. On this night the moon was in first quarter phase, so as

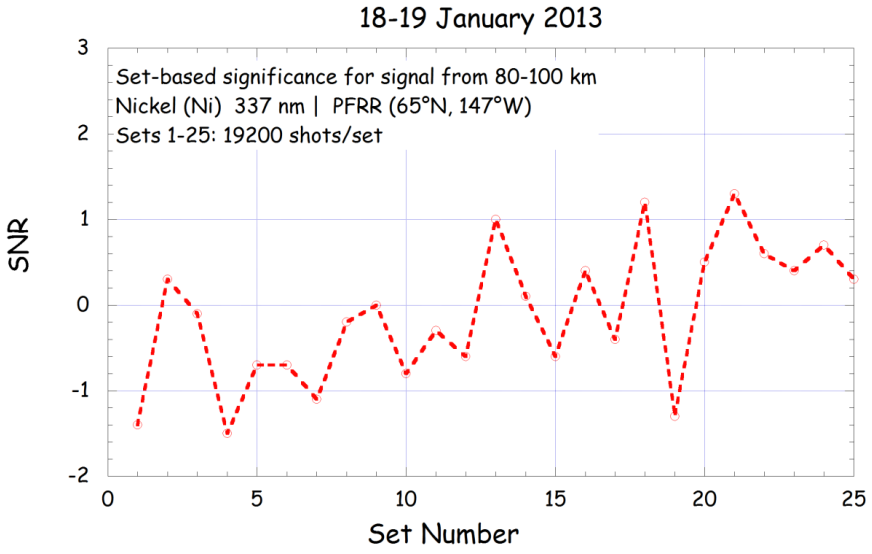

Figure 4.20 Significance plot of data taken during the Ni search on 18-19 January 2013.

it set in the middle of the night the background light decreased significantly. Although the sky looked very clear, the Rayleigh lidar experienced lower signal than expected from high altitudes that degraded throughout the night, evidently high cirrus moving over the area. Subvisual cirrus or diamond dust may have been present throughout the night, scattering light out of the beam and decreasing the signal even when the sky looked clear.

4.4.5. 25-26 January 2012

Our fifth and final attempt to observe the Ni layer took place on the night of 25-26 January 2013. We ran the excimer at 10 Hz and 20 kV, and measured an energy of 411 mJ per pulse. The dye energy at these settings measured 4.2 mJ per pulse at 337 nm, giving a laser power of 42 mW. Once again, we focused on our prospective wavelength region, a 9 pm range from 336.993 to 336.985 nm. We made three scans of this range, for a total of 27 sets. As on the previous night, we took sets with very long time integration, 2400 shots per profile and 8 profiles per set. Unfortunately, there were no promising sets in the data; all the SNR values for the resonance layer range were below 2 (Figure 4.21). While the night was very cold, about -35°C, and very clear, there was a very bright full moon in the sky during the entire observation period. This moonlight kept the background about 10 times higher than the previous night. In addition, the aurora was very active during the night, and during some periods brief spikes in signal levels could be seen when the aurora was in the beam. Thus, any resonance signal that was present was drowned out by the background signal.

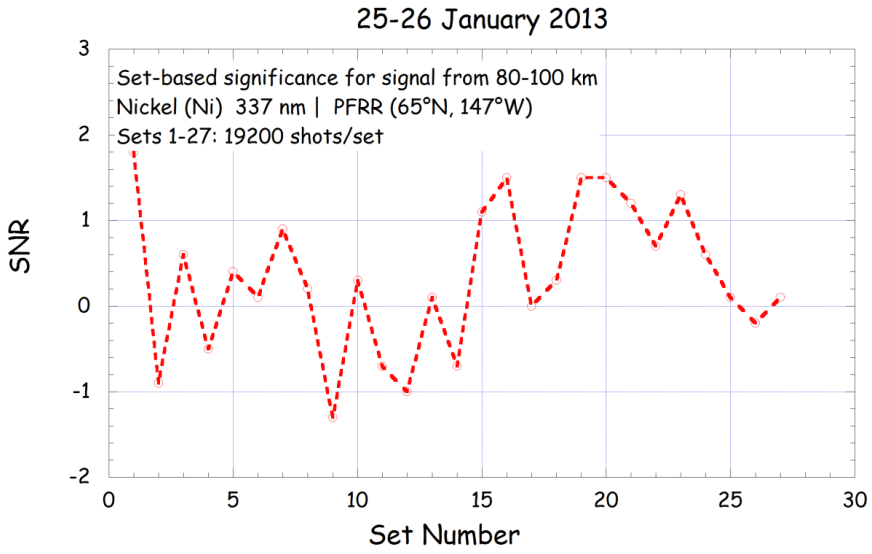

Figure 4.21 Significance plot of data taken during the Ni search on 25-26 January 2013.

4.5. Ni layer characteristics

After our fifth night in late January, we decided to conclude our Ni search. At this time of the year, mesospheric metal abundances drop from their peak levels in November (discussed in section 3.2). Since the signal levels from the Ni layer are already expected to be at the threshold of detection at best with peak abundances, it is unlikely that we would detect the layer with lesser abundances. In light of the last two nights of observations, during which we took long integrations at each wavelength in our most promising wavelength region, but experienced no possible detections of the layer, we determined that any chances of detecting the layer were past for the year.

4.5.1. Evaluation of Ni observations

Looking at all the accumulated Ni data, we culminated our study with an analysis of all the sets that showed some possibility of a Ni layer. A set can be considered a possibility if the signal from 80-100 km is higher than the statistical uncertainty in this range. The background range for these calculations is taken as 200-300 km. Thus to be considered, the SNR as shown during the discussion of observations must be greater than 1. Of all the sets where this condition is met, the most reliable possibilities occur in the range 336.985-336.995 nm due to the preponderance of possibilities in this range and the pattern of significance with altitude appears to outline a layer in several of the sets in this range. No sets showed sufficient SNR in the resonance range to confidently disclose the presence of a layer, except perhaps set 20 on 27-28 November 2012 at 336.988 nm. After inspecting the photon count profiles of each of the sets, we narrowed the prospective sets down to the three listed in Table 4.4, all of which have an SNR of 2 or greater. Although the January nights yielded some sets with SNRs higher than 1, none were higher than 2, and the photon count profiles showed no evidence of a layer. There were no prospective sets seen in the first night of observations, 7-8 November 2012.

Looking at the individual profiles, we find that set 20 on 27 November is the most promising, with a large SNR at 80-90 km (Figure 4.22, top). The peak of this spike is larger than any other spike of noise in the entire profile.

Table 4.4 Possible sightings of the Ni layer

Date	Set	Wavelength (nm)	Shots	SNR
Nov. 27	20	336.988	5000	3.4
Nov. 27	55	336.990	20000	2.0
Dec. 20	21	336.990	10000	2.3

However, it is only slightly above the rest of the noise, and could easily be simply a large spike of noise. Nevertheless, this is the best possibility of a layer that we found in the entire study. Set 55 on this same night also had a high SNR; while there is elevated signal in the 80-100 km range, this may be simply noise based on the appearance of the rest of the profile (Figure 4.22, bottom). Set 55 is at a higher count level than set 20 because of the longer time integration: 20000 shots instead of 5000.

The third high SNR profile was set 21 on 20-21 December. Once again, this set has elevated signal in the 80-100 km region, but no features that could be distinguished from the noise and conclusively determined to be a layer (Figure 4.23). The signal levels on 20 December are also much lower than those on 27 November, probably due to the decreased background levels from moonlight. After subtracting the background counts (average of 200-300 km), we added the three profiles together to obtain the best possible look at any layer that might be present (Figure 4.24). We see a prominent layer-like shape between 80-90 km, largely influenced by the 27 November set 20. Figure 4.25 shows the SNR as a function of altitude for the combination of these three sets; a layer appears to be present, and has about the same signature as the SNR profile for the Ni simulation. For the 80-100 km range bin, the SNR value in the combined profile of the three sets is 3.6, in the upper end of the range for SNR in the Ni simulation.

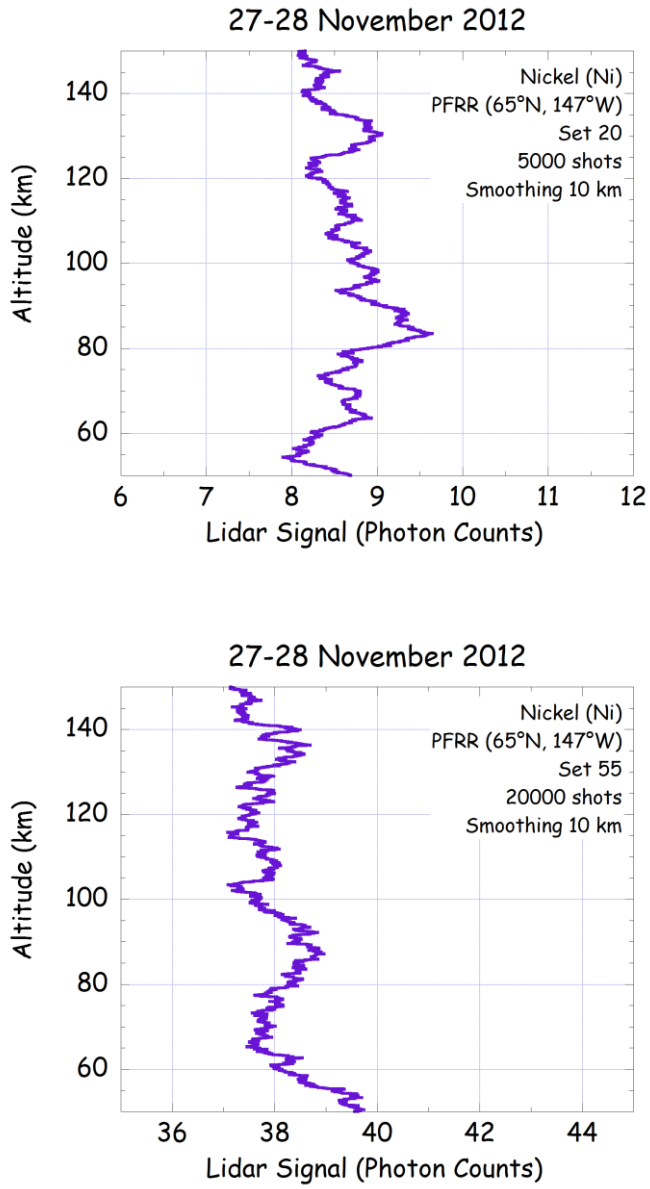

Figure 4.22 Profiles of the resonance layer in the highest SNR sets taken on 27-28 November 2012.

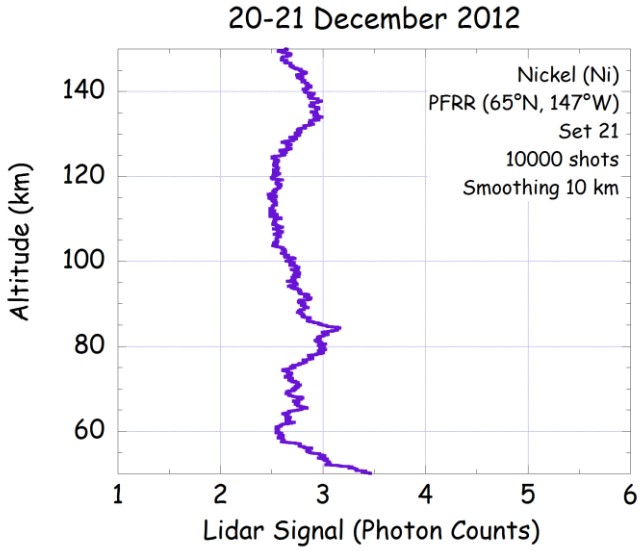

Figure 4.23 Profile of the resonance layer in the highest SNR set on 20-21 December 2012.

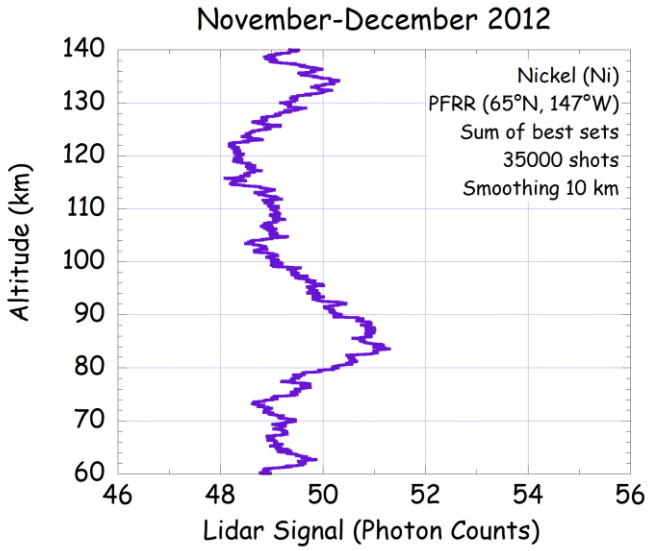

Figure 4.24 Combination of the three highest SNR sets taken during the entire Ni search: 27 November sets 20 & 55, and 20 December set 21.

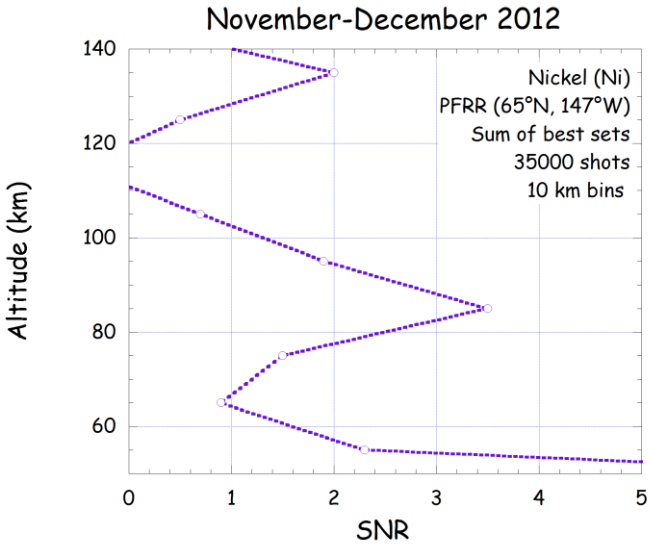

Figure 4.25 SNR in 10 km altitude bins as a function of altitude for the combination of the three most promising sets.

4.5.2. Ni density estimate

With our results from several sets producing signals similar to those expected from the Ni simulation, we proceed to make an estimate of the Ni density from these observations. Since we do not have a measured linewidth and C_{eff} for Ni, we use several C_{eff} values from past Fe measurements and scale them based on the σ_0 values for Fe and Ni (Equation 2.19; Table 4.1). The largest C_{eff} used for computing Fe densities is 4.2×10^{-17} m^2 with a linewidth of 1 pm, which scales to 2.4×10^{-17} m^2 for Ni; the smallest C_{eff} used for Fe is 1.2×10^{-17} m^2 with a linewidth of 4 pm, which scales to 6.9×10^{-18} m^2 for Ni. Density profiles calculated with these values are shown in Figure 4.26. The raw photon count profiles are quite noisy, so these profiles are smoothed at 10 km before determining the density profile. A main layer extends from about 74 to 103 km with a peak at 88 km. A secondary peak at 110 km. Given the data quality, we define the Ni layer within these boundaries of the main layer and filter the densities at 10 km to calculate the layer parameters,

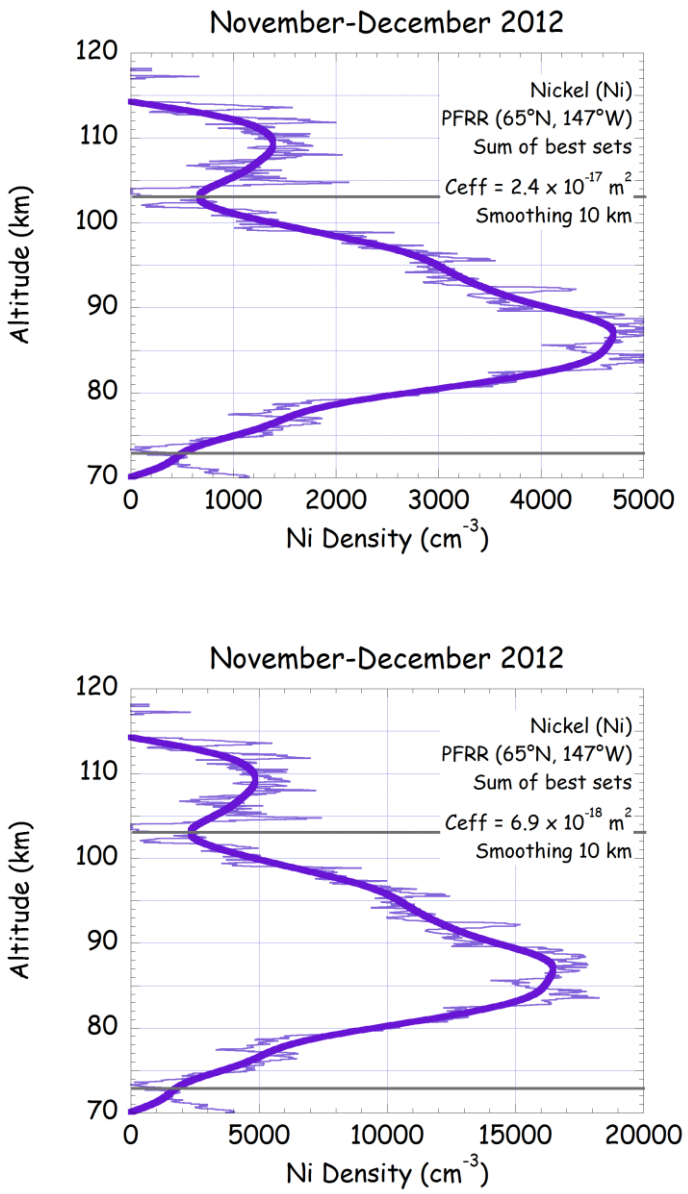

Figure 4.26 Estimated Ni density profiles from a combination of the three best sets based on a Ceff of 2.4 × 10^{-17} m^2 (top) and 6.9 × 10^{-18} m^2 (bottom). The thick curves are Parzen filtered at 10 km, while the thinner curves are unfiltered.

given in Table 4.5. We present the values for the Ni density retrievals for both values of C_{eff}. Comparing the column abundance of Ni with that of Na and Fe in Figure 3.2 we see that column abundance of Ni is between that of Na and Fe.

4.5.3. Specific Na-based Ni simulation

To reevaluate our estimated Ni signal based on the observed conditions, we run our Ni simulation as before, but this time obtaining the parameters pertaining to laser performance and sky conditions from Rayleigh counts in the 30-35 km altitude range in the 27 November Ni measurements. We make a simulation for 27 November lidar system parameters because the Rayleigh counts are higher on this night than on any of the other Ni observations. Factors depending on the target species are scaled as in the original Ni simulation. Na data from 23 October 2012, taken just before the Ni observations began, is used for original data to provide the shape of the layer in this simulation. The lidar system scaling, taken from the Rayleigh counts in 30-35 km, is 0.024, and the target species scaling is 0.036, leading to a total scaling of 0.001, or 0.1%, to simulate the Ni layer from observations of the Na layer. The background signal is taken from the 27 November Ni measurements. Figure 4.27 shows the simulated Ni profile without the noise

Table 4.5 Estimated parameters of the Ni layer

	$C_{eff} = 2.4 \times 10^{-17}$ m^2	$C_{eff} = 6.9 \times 10^{-18}$ m^2
Column Abundance (10^9 cm^{-2})	8.3	29.2
Peak (km)	87.0	87.0
Centroid Height (km)	88.1	88.1
RMS Width (km)	6.5	6.5
Peak Density (10^3 cm^{-3})	4.7	16.5
Bottomside RMS Width (km)	5.7	5.7
Topside RMS Width (km)	7.3	7.3

added for 35,000 shots, the same number of shots as in the composite profile of the three best sets in Figure 4.24. The signal level from the layer that appears in this profile is much smaller than that of the random noise fluctuations in the measurements.

In Figure 4.28, a night of data at the Ni wavelengths for the conditions of 27 November has been simulated set-by-set by calculating the expected profile without noise and adding noise in each set. Each of the 50 profiles has 5000 shots, as did each set in the main scan on 27 November. We find in this simulation that the SNR values fluctuate randomly between 3.1 and -1.4, with an average of 0.55. These simulated values of SNR appear similar to the results we presented in section 4.4 for our five nights of observations. Figure 4.29 shows the expected results for no signal present; the SNR value

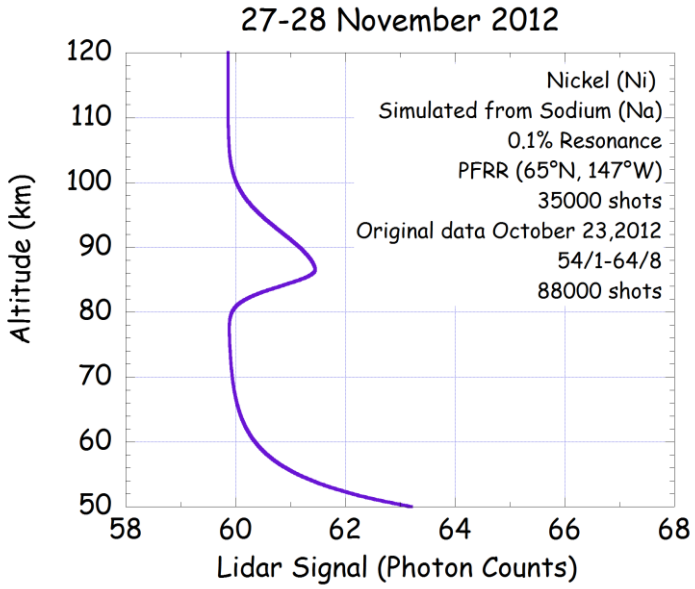

Figure 4.27 Simulated Ni layer for 27 November parameters without noise added.

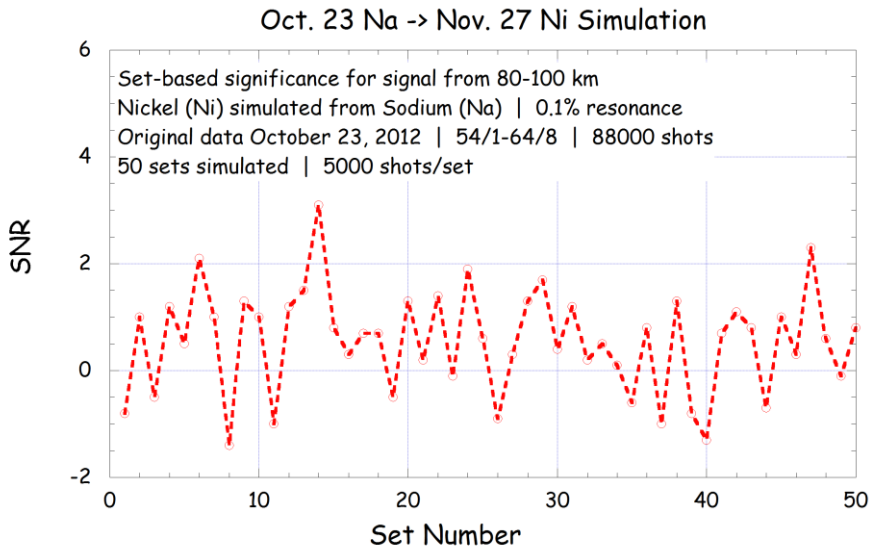

Figure 4.28 Significance plot of simulated Ni data for 27 November observations using 23 October sodium data.

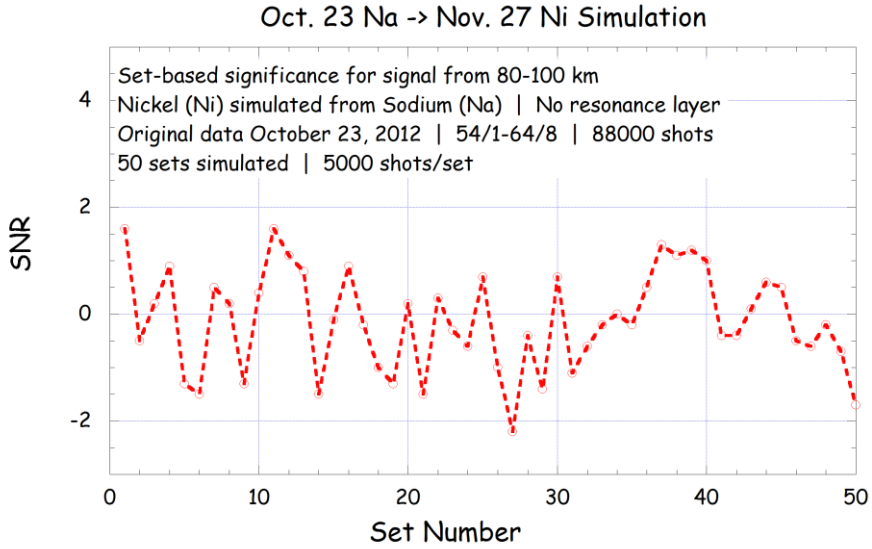

Figure 4.29 Significance plot of simulated data at the Ni wavelength with no resonance layer present for 27 November observations using 23 October sodium data.

fluctuates between 1.6 and -2.2, with an average of -0.13. Thus it appears that the sets we chose, with SNR values between 2.0 and 3.4, are in the range of values expected for sets containing the resonance layer, but above the range of values produced from random noise, indicating that we likely made a detection of the layer.

4.6. Detection threshold simulation

From these simulations, it is clear that the results we found during our Ni search are to be expected for our lidar system. Some signal from the Ni layer may have been found in our data, due to the predominance of possible sightings occurring in the same wavelength range of 988-993 nm. However, the resonance signal contained in these profiles is still close the range of random noise, and we could not reliably repeat our measurements of the layer every time we observed at the prospective wavelength. Thus we conclude that we are at the threshold for Ni detection with our current lidar system.

To determine what parameters we might change to pass the detection threshold and observe the Ni layer with high confidence, we ran several statistical experiments with the Ni simulation program. In these experiments, we modified the background level and the laser power separately, multiplying each by a scale factor. Modifying background levels allows us to determine how sky conditions affect the measurement, and whether taking observations under pristine conditions would improve our SNR above the threshold. Background light is contributed to the sky slightly by light pollution from Fairbanks, but due to our remote location most of the background is from moonlight and aurora. Atmospheric conditions affect the background as well: light cirrus or other ice or aerosol particles suspended in the atmosphere scatter the light that is there, taking light out of the laser

beam and enhancing the background from external sources. Laser power, of course, is the primary determinant of the amount of signal we receive, and the simulation experiment demonstrates what power we would need to lift the signal to a detectable level.

In each experiment, we made a night of simulated sets as before, using Na data taken on 23-24 October 2012, scaling lidar system parameters using Rayleigh counts from 27-28 November 2012, and simulating 100 sets of 5000 shots per set. The simulated profiles are scaled by a multiplier of either background counts or laser power, depending on the experiment. For each set we calculated the SNR of the resonance layer as described in the preceding discussion of the Ni search.

4.6.1. Background scaling

In the first experiment, we explore how the SNR varies with background scaling. Background is scaled by a multiplier that ranges from 0.0 to 2.0 in steps of 0.1. For each value of background scaling, we compute an average maximum, minimum, and average SNR in three steps as follows:

1. Simulate a night of data as described above and determine the maximum, minimum, and average SNR for the entire simulation.
2. Repeat this process 100 times, resulting in 100 values each of maximum, minimum, and average SNR.
3. Average each of these arrays of maximums, minimums, and averages to reduce statistical uncertainty. We also find the highest maximum and the lowest minimum of all the trials.

The result, shown in Figure 4.30, is a range of possible SNR and an average SNR for the simulated Ni layer as the background counts change. As the background increases from the value observed on 27 November (background scaling of 1.0), there is only a slight decrease in the SNR. Going the other

direction, SNR does increase noticeably below a background scaling of 0.5, gaining a factor of two at a background scaling of 0.2. At a background level of zero (the best possible case for detecting the layer), the average SNR is 5.6 with an average range from 4.2 to 6.7. However, this great increase is only seen below a background scaling of 0.1. Figure 4.31 shows the same experiment, but also includes the case of no resonance layer present. Without a resonance layer, there is no change in SNR with background, and the average SNR is zero. The range of possible SNR with the resonance layer present is only slightly higher than that of no resonance signal for all background scaling above 0.5, so it would be very difficult to distinguish the signal from the noise, as we saw in our observations.

The signal from the Ni layer is very low compared to the background for our current lidar system. It may be possible to reduce the background by at least a factor of four by using a smaller field of view (FOV) on the receiver telescope. During the Ni observations, we used a 2 mrad FOV, but for the Na and Fe measurements used in the Ni simulation, we used a 1 mrad FOV, which would allow less background light into the telescope. Along with this change, a darker, clearer night may further decrease the background enough to achieve an increase in the SNR.

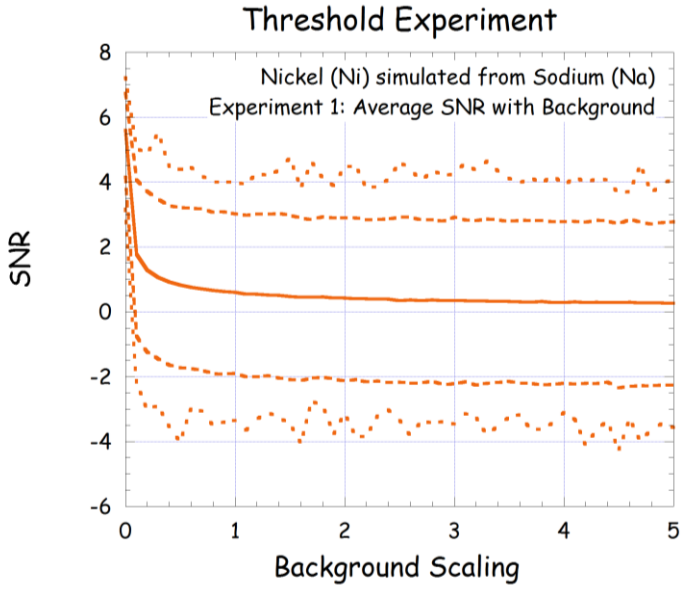

Figure 4.30 SNR in significance plots for the Ni layer simulated for 27 November as a function of background. Solid line is the average SNR, dashed lines are average maximum and average minimum, and dotted lines are highest maximum and lowest minimum.

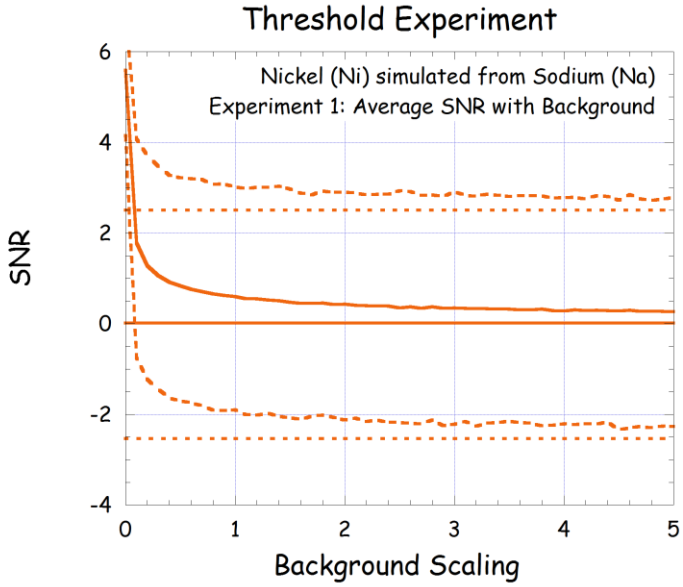

Figure 4.31 SNR with background for the case of both the resonance layer present and not present. Without the resonance layer, the SNR does not change with background, and the average is zero. Solid lines represent the average SNR for both cases, dashed lines are average maximum and minimum for the resonance layer, and dotted lines are the average maximum and minimum for no layer.

4.6.2. Laser power scaling

In Experiment 2 we repeat Experiment 1, but this time scaling laser power instead of background counts. Laser power is scaled from 1.0 to 10.0 in steps of 1.0. The results are shown in Figure 4.32. Experiment 2 shows a linear trend of increasing SNR with laser power, as expected. Currently, at laser power scaling of 1.0, we have an average SNR of about 1 and a possible range of SNR from -3 to +5 for sets actually observing the Ni layer. To ensure that the average minimum SNR would be above zero, we would need to raise the laser power by a factor of 4; the average value obtained would then be 2.5, and the average maximum SNR would be around 5. An increase in power by a factor of 7 would reliably raise the minimum possible SNR above 0.0 and bring the average to 4.0, with the maximum above 7.

On the night of 27 November, our dye laser power at 337 nm was about 60 mW; this was our highest power of all the Ni observations. According to these simulation experiments, detection of Ni would require raising this

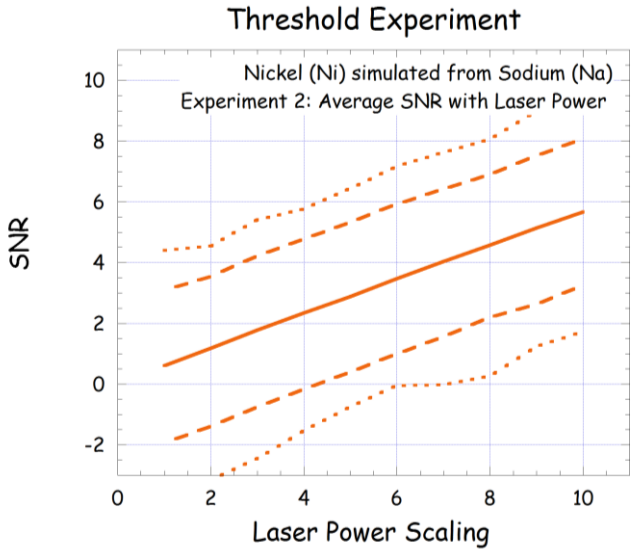

Figure 4.32 SNR in significance plots for the Ni layer simulated for 27 November as a function of laser power. Solid line is the average SNR, dashed lines are average maximum minimum, and dotted lines are highest maximum and lowest minimum.

power to about 240 mW, and would become much more probable if using a laser power of 420 mW. Our dye laser power on 27 November was 96 mW at 343 nm, the peak of the dye; for the excimer power of 4.35 W, the dye laser efficiency was 2.2%. The quoted efficiency of the dye is 8%, or a factor of 3.64 higher than the actual efficiency in our system. If we could optimize the laser performance to produce the maximum efficiency, our dye power at 337 nm would then be 211 mW. We could then have a signal return that would reliably give SNRs above those from random noise, enabling a confident detection of the Ni layer based on this simulation.

4.6.3. Ni Abundance scaling

Experiment 3, in which we scale Ni abundance from 0.0 to 10.0 in steps of 0.1 (Figure 4.33), is very similar to Experiment 2. However, based on observations of Na and Fe, as discussed in section 3.2, we expect that mesospheric metals are at their highest abundance in early winter, about the time the best observations were taken, so we do not expect Ni abundance to increase.

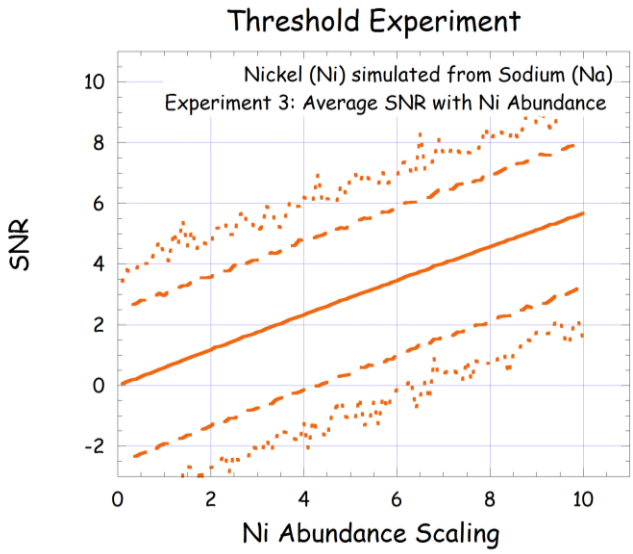

Figure 4.33 SNR in significance plots for the Ni layer simulated for 27 November as a function of Ni abundance.

5. Summary and Conclusions

In this thesis, we have conducted an integrated investigation of several aspects of resonance lidar studies of mesospheric metal layers (i.e., lidar system performance, dynamics of the mesospheric metal layers, and initial detection of the mesospheric nickel layer). Laser performance, at the heart of lidar observations, occupied much of the effort in this study. We have demonstrated the alignment and operation of an existing dye laser at LRL-PFRR and installed a new dye laser, successfully using it for observations. Using data taken at LRL-PFRR in 2000-2002, we summarized common motion of the sodium (Na) and iron (Fe) layers, tying together the conclusions of several previous studies on the dynamics of the metal layers. Our search for the previously undetected nickel (Ni) layer yielded new information on the limits of our resonance lidar system and resulted in a likely detection of the layer.

The existing excimer-pumped dye laser used for resonance observations at LRL-PFRR had not been operated for several years at the beginning of this study, so we performed some standard maintenance on the excimer laser and realigned the dye laser to achieve optimum performance. In summer 2012, we checked its performance by observing the spectrum and power output when operating on Rhodamine 6G dye, the dye used for Na observations which fluoresces around 590 nm. Once the fall observing season arrived, we took two nights of Na data to verify the performance of this laser on a target species that is very reflective and resonates at a visible wavelength. After determining that the laser was indeed operating properly, we shifted to a UV dye to pursue our search for the Ni layer.

During the course of this study, our lidar group obtained a new Nd:YAG-pumped dye laser system from another lidar group that had used it

for Na observations, but had discontinued its use. We intended to eventually use it for taking observations of Na concurrently with observations of another metal using the excimer-pumped dye laser. In this study, we installed the laser system, brought the Nd:YAG laser to an operational state, and aligned the dye laser, testing it with several nights of Na observations. Much of the work went into the setup of the Nd:YAG laser. Nd:YAG lasers are used for Rayleigh lidar observations at LRL-PFRR, so members of the lidar group have experience with their operation. Before operation, the cooling system had to be cleaned and the water deionized. Initial operation of the Nd:YAG laser produced very low power. We replaced the flashlamps, which provide the energy source for lasing. After several attempts at alignment still failed to increase the power, we found that the Q-switch in the oscillator was free-running, which was solved by a slight rotation of a 1/4 wave plate. The Nd:YAG power was then sufficient for operation at 2.8 W.

Following the setup of the Nd:YAG laser, the dye laser only required alignment of the Nd:YAG beam and then the resulting dye beam inside the dye laser cavity. The power produced by the dye laser was 0.28 W, about 9 times greater than the power produced by the excimer-pumped dye laser. After this new system was fully operational, we took three nights of Na data. Because of the higher signal, it was possible to process the data at a much higher time resolution. Whereas we processed previous resonance data with a 60 minute integration window in time steps of 15 minutes, we increased the resolution by 5 times for data taken with the new laser, using a integration window of 12 minutes and a time step of 3 minutes. This higher resolution allowed us to see much more detailed dynamics within the Na layer.

Dynamics in the metal layers are driven by atmospheric motions; therefore, these species can be used to study the dynamics of the mesopause region. Collins and Smith [2004] interpret the motions on the bottom side of

the Na layer on timescales of several hours as being caused by downward propagating gravity waves. These conclusions would be stronger if similar motions were found in several metals, showing that the dynamics were not simply driven by the chemistry of a particular species. Yi et al. [2008] present common observations of Na and Fe, showing a high degree of correlation in the motion of bottom side contours between the two metals, but do not suggest a mechanism. We sought to tie together these two studies using existing data from our lidar group. Between 2000 and 2003, 21 nights of simultaneous Na and Fe observations were taken at LRL-PFRR. We extracted constant density contours at similar altitudes on the bottom side of both metals and found high correlations between the species in the motions of these contours. Two-thirds of the nights surveyed showed best correlations greater than 0.85.

By fitting the contours to harmonic waves, we sought to determine if the motion was consistent with that of gravity waves. By taking the best fit period and propagating it to other contours in the bottom side of the layer, we could determine a phase progression with height and a vertical wavelength. Negative vertical wavelengths represent downward propagating waves expected from gravity waves. Over 90% of the nights surveyed in Na exhibited downward propagating waves, and all showed fits above the 90% confidence level based on the SNR of the fit, with most above 95%. Slightly less showed negative wavelengths in Fe, but still over 75%. All of these Fe nights showed fits above 95% confidence except one, which was above 90%. These results further support the conclusion that gravity waves are the result of motions in the mesosphere, and that metal layers can act as a tracer for these motions.

It is understood that meteoric ablation is the source of the metal layers. Many metals found in meteorites have been observed by lidar, but Ni,

a major constituent of meteorites, has not yet been observed. We sought to make a detection of Ni using our excimer-pumped dye laser system. The only viable resonant line for Ni is in the UV at 337 nm. Fe observations at 372 nm have been made with the excimer-pumped dye laser, and dyes are available that fluoresce over 337 nm with this system. However, observations of Ni are more difficult due to the decreased laser efficiency and increased atmospheric absorption that resulted from the resonant line being further in the UV. In addition, the abundance of Ni and the strength of the line are less than that of Fe. Our original estimate of the resonant signal from Ni was 3% of that from Fe. This estimate shows that the Ni layer is just barely detectable with our system, and thus requires a long integration time of over an hour to confirm its presence.

Because the laser tuning wavelength when tuned to the Ni line may be slightly different than the wavelength required for resonance due to index of refraction changes, it was necessary to search for the line at picometer resolution over a range of 50 pm higher than the listed transition wavelength. We conducted this wavelength scan on two nights in November 2012. The first night yielded no results, but the second night yielded a relatively high SNR (compared to other wavelengths) of the resonant layer range (80-100 km) at 336.988 nm, with the appearance of a resonant layer at the proper altitude. Later on the same night, we observed a fairly high SNR at 336.990 pm. The same 50 pm wavelength scan on a third night in December 2012 showed a high SNR at 336.990 nm. As these were the only possible detections of the resonance layer, we determined that the resonance line was likely found in the wavelength range 336.998-990 nm. We took two more nights of data in January 2013 focusing on a smaller range around 336.99 nm, but found no evidence of the Ni layer. On these two nights, we

experienced high background levels and possibly decreased metal abundance based on observed climatology of Fe and Na.

Simulation of the expected Ni signal after observations, basing the atmospheric transmission and laser power scaling on Rayleigh counts from observations during the Ni search, show about 5 times less signal expected than in the original simulation. The range of possible SNRs for the resonance layer region with signal is largely overlapping that without signal. Thus we conclude that the signals we received were as expected for our lidar system. We made an estimate of the Ni layer profile based on the three best sets of data that showed high SNR. We did not measure the linewidth of the laser directly at 337 nm, and we calculated the Ni densities for linewidths of 1 pm and 4 pm to obtain a range of possible values. We present the first estimate of the mesospheric Ni layer profile. The density values are similar to those found for Na and Fe in midwinter. Although it appears that we detected the Ni layer in these measurements, the signal is still too low to conclusively determine the presence of the layer. Our simulations suggest that the best way to make a clear detection of the Ni layer would be to increase the laser power. It may be possible with our dye laser to increase the power by a factor of four if the dye were to fluoresce at its maximum efficiency by better performance of the laser. Otherwise, a more powerful laser (e.g., a solid-state laser operating at 674 nm doubled to 337 nm) would be required to make routine Ni measurements that reveal the seasonal variation of the layer.

References

Abo, M. (2005), Resonance Scattering Lidar, in Lidar: Range-Resolved Optical Remote Sensing of the Atmosphere, edited by C. Wietkamp, pp. 307-323, Springer, New York, NY.

Andrews, D. G., J. R. Holton, and C. B. Leovy (1987), Middle Atmosphere Dynamics, 489 pp., Academic Press, Orlando, FL.

Baumjohann, W., and R. A. Treumann (1997), Basic Space Plasma Physics, 329 pp., Imperial College Press, London.

Berk, A., et al. (2006), MODTRAN5: 2006 update, Proceedings of the SPIE, 6233, 62331F.

Bowman, M. R., A. J. Gibson, and M. C. W. Sandford (1969), Atmospheric Sodium Measured by a Tuned Laser Radar, Nature, 221(5179), 456-457.

Brackmann, U. (1997), Lambdachrome® Laser Dyes, 284 pp., Lambda Physik GmbH, Göttingen.

Brasseur, G., and S. Solomon (1986), Aeronomy of the Middle Atmosphere, 2nd ed., 452 pp., D. Reidel Publishing Company, Dordrecht, Holland.

Breese, J. (2001), Development of a Fe Boltzman Temperature Lidar, Master's thesis, 98 pp, University of Alaska Fairbanks, Fairbanks, AK.

Chu, X., and G. C. Papen (2005), Resonance Fluorescence Lidar for Measurements of the Middle and Upper Atmosphere, in Laser Remote Sensing, edited by T. Fujii and T. Fukuchi, pp. 179-432, Taylor & Francis, Boca Raton, FL.

COESA (1966), U.S. Standard Atmosphere Supplements, 1966, U.S. Government Printing Office, Washington, D.C.

Collins, R. L., and R. W. Smith (2004), Evidence of Damping and Overturning of Gravity Waves in the Arctic Mesosphere: Na Lidar and OH

Temperature Observations, Journal of Atmospheric and Solar-Terrestrial Physics, 66(10), 867-879.

Collins, R. L., D. C. Senft, and C. S. Gardner (1992), Observations of a 12 h Wave in the Mesopause Region at the South Pole, Geophysical Research Letters, 19(1), 57-60.

Collins, R. L., K. P. Bowman, and C. S. Gardner (1993), Polar Stratospheric Clouds at the South Pole in 1990: Lidar Observations and Analysis, Journal of Geophysical Research: Atmospheres, 98(D1), 1001-1010.

Collins, R. L., T. J. Hallinan, R. W. Smith, and G. Hernandez (1996), Lidar Observations of a Large High-Altitude Sporadic Na Layer During Active Aurora, Geophysical Research Letters, 23(24), 3655-3658.

Collins, R. L., G. A. Lehmacher, M. F. Larsen, and K. Mizutani (2011), Estimates of Vertical Eddy Diffusivity in the Upper Mesosphere in the Presence of a Mesospheric Inversion Layer, Annales Geophysicae, 29(11), 2019-2029.

Collins, R. L., S. M. Bailey, U. Berger, F.-J. Lubken, and A. W. E. Merkel (2009), Special Issue: Global Perspectives on the Aeronomy of the Summer Mesopause Region, Journal of Atmospheric and Solar-Terrestrial Physics, 71(3-4), 285-551.

Continuum (1991), Operation and Maintenance Manual: NY80, 81 & 82 Lasers, Continuum, Santa Clara, CA.

Fujii, T., and T. Fukuchi (Eds.) (2005), Laser Remote Sensing, 888 pp., Taylor & Francis, Boca Raton, FL.

Gardner, C. S. (1989), Sodium Resonance Fluorescence Lidar Applications in Atmospheric Science and Astronomy, Proceedings of the IEEE, 77(3), 408-418.

Gelinas, L. J., K. A. Lynch, M. C. Kelley, R. L. Collins, M. Widholm, E. MacDonald, J. Ulwick, and P. Mace (2005), Mesospheric Charged Dust

Layer: Implications for Neutral Chemistry, Journal of Geophysical Research: Space Physics, 110(A1), A01310.

Halliday, D., and R. Resnick (1981), Fundamentals of Physics, 2nd ed., 947 pp., John Wiley & Sons, Inc., New York.

Irving, B. (2012), Rayleigh Lidar Studies of Mesospheric Inversion Layers at Poker Flat Research Range, Chatanika, Alaska, Master's thesis, 159 pp, University of Alaska Fairbanks, Fairbanks, AK.

Light, A. (2009), Theoretical and Experimental Investigations of Resonance Fluorescence Lidar for Measurements of N_2^+ in the Auroral Atmosphere, Master's thesis, 162 pp, University of Alaska Fairbanks, Fairbanks, AK.

Murad, E., and I. P. Williams (Eds.) (2002), Meteors in the Earth's Atmosphere, 2nd ed., 322 pp., Cambridge University Press, Cambridge.

NIST (2012), NIST Atomic Spectra Database, Version 5, http://www.nist.gov/pml/data/asd.cfm, Acessed June 13, 2013.

Peshave, M. (2004), Design and Implementation of a Microcontroller-Based Closed-Loop Tuning-Controller for a Tunable Dye Laser, Master's thesis, 100 pp, University of Alaska Fairbanks, Fairbanks, AK.

Petty, G. W. (2006), A First Course in Atmospheric Radiation, 458 pp., Sundog Publishing, Madison, WI.

Pfrommer, T., P. Hickson, and C.-Y. She (2009), A Large-Aperture Sodium Fluorescence Lidar with Very High Resolution for Mesopause Dynamics and Adaptive Optics Studies, Geophysical Research Letters, 36(15), L15831.

Plane, J. M. C. (1991), The Chemistry of Meteoric Metals in the Earth's Upper Atmosphere, Int. Rev. Phys. Chem., 10(1), 55-106.

Plane, J. M. C., R. M. Cox, and R. J. Rollason (1999), Metallic Layers in the Mesopause and Lower Thermosphere Region, Advances in Space Research, 24(11), 1559-1570.

Plane, J. M. C., R. M. Cox, J. Qian, W. M. Pfenninger, G. C. Papen, C. S. Gardner, and P. J. Espy (1998), Mesospheric Na layer at Extreme High Latitudes in Summer, Journal of Geophysical Research: Atmospheres, 103(D6), 6381-6389.

Press, W. H., S. A. Teukolsky, W. T. Vetterling, and B. P. Flannery (1992), Numerical Recipes in FORTRAN: The Art of Scientific Computing, 963 pp., Cambridge University Press, Cambridge, UK.

Senft, D. C., R. L. Collins, and C. S. Gardner (1989), Mid-Latitude Lidar Observations of Large Sporadic Sodium Layers, Geophysical Research Letters, 16(7), 715-718.

Silfvast, W. T. (1996), Laser Fundamentals, 521 pp., Cambridge University Press, Cambridge.

Su, L. (2007), Development of Resonance Fluorescence Lidar for Studies of the Aurora, Ph.D thesis, 187 pp, University of Alaska Fairbanks, Fairbanks, AK.

Thurairajah, B., R. L. Collins, V. L. Harvey, R. S. Lieberman, and K. Mizutani (2010a), Rayleigh Lidar Observations of Reduced Gravity Wave Activity During the Formation of an Elevated Stratopause in 2004 at Chatanika, Alaska (65°N, 147°W), Journal of Geophysical Research: Atmospheres, 115(D13), D13109.

Thurairajah, B., R. L. Collins, V. L. Harvey, R. S. Lieberman, M. Gerding, K. Mizutani, and J. M. Livingston (2010b), Gravity Wave Activity in the Arctic Stratosphere and Mesosphere During the 2007–2008 and 2008–2009 Stratospheric Sudden Warming Events, Journal of Geophysical Research: Atmospheres, 115(D3), D00N06.

UW-DAS (2013), Atmospheric Soundings, http://weather.uwyo.edu/upperair/sounding.html, Acessed June 13, 2013.

Verdeyen, J. T. (1981), Laser Electronics, 444 pp., Prentice-Hall, Englewood Cliffs, NJ.

Wallace, J. M., and P. V. Hobbs (2006), Atmospheric Science: An Introductory Survey, 2nd ed., 483 pp., Academic Press, Burlington, MA.

Wayne, R. P. (2000), Chemistry of Atmospheres, 3rd ed., Oxford University Press, Oxford.

Weitkamp, C. (Ed.) (2005), Lidar: Range-Resolved Optical Remote Sensing of the Atmosphere, 455 pp., Springer, New York.

Yi, F., S. Zhang, X. Yue, Y. He, C. Yu, C. Huang, and W. Li (2008), Some Ubiquitous Features of the Mesospheric Fe and Na Layer Borders from Simultaneous and Common-Volume Fe and Na Lidar Observations, Journal of Geophysical Research: Space Physics, 113(A4), A04S91.

Appendix: Na and Fe Density Plots

False-color contour plots of the Na and Fe layers for the 21 nights of data used in the study in Chapter 3 are shown in this Appendix. Each page shows one night of data, with the Na layer in the upper plot and the Fe layer in the lower plot. Densities are given in atoms cm^{-3} and are listed in the color scale to the right of each plot; contours are plotted at each listed level in the scale. Times are given in local Standard Time (Alaska Standard Time: UT-9 h).

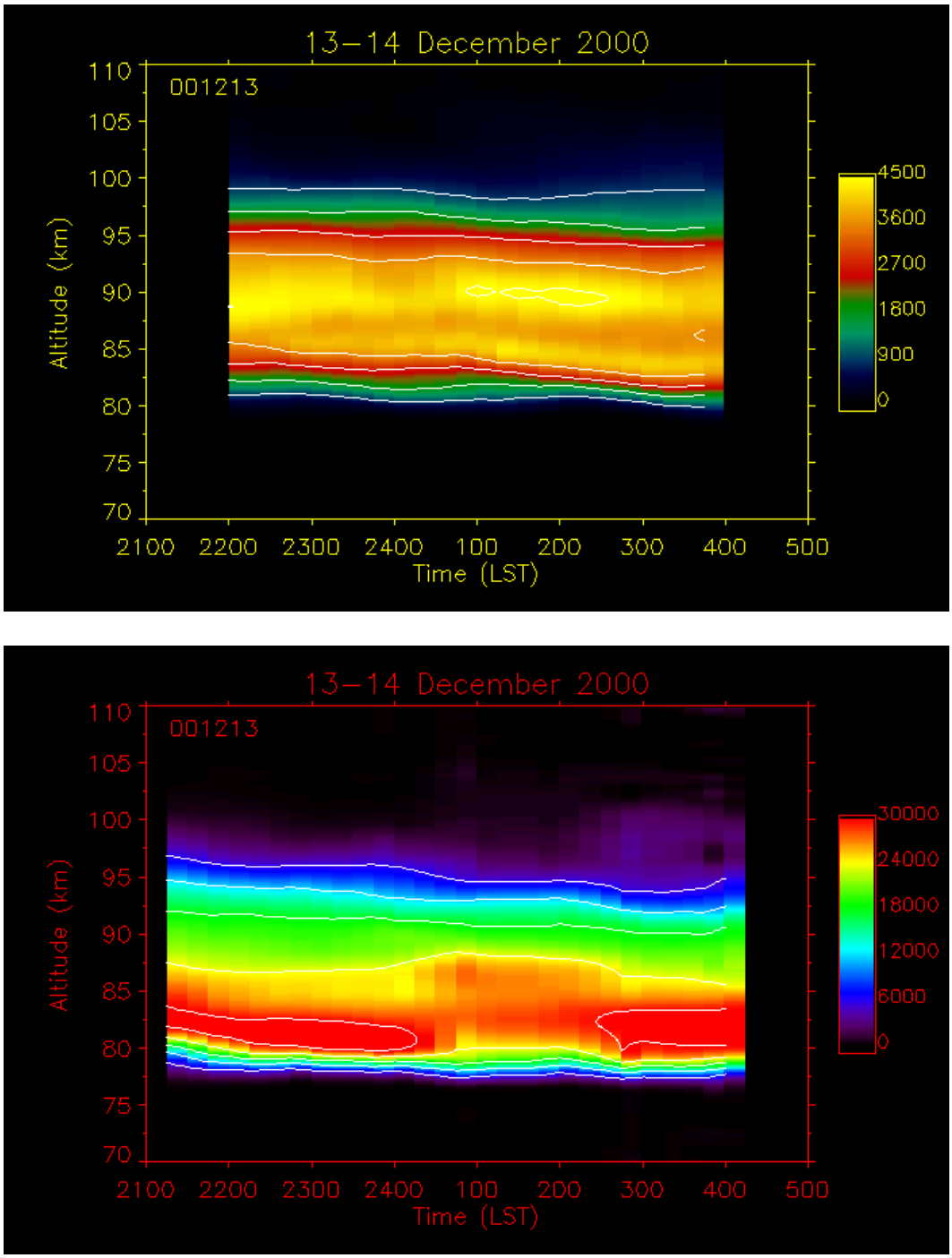

Figure A.1 False color contour plots of Na (top) and Fe (bottom) on the night of 13-14 December 2000. Densities given in atoms cm^{-3}.

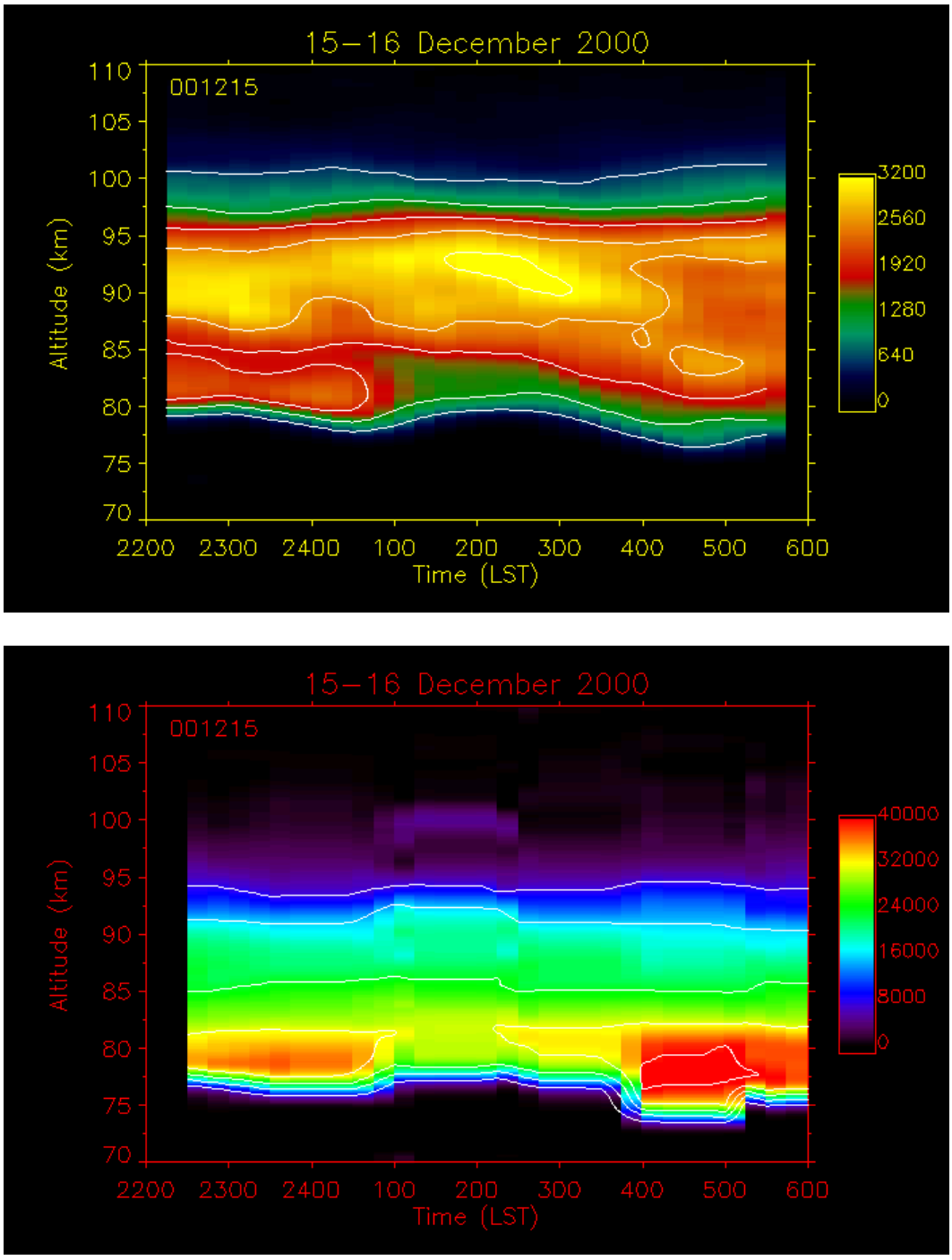

Figure A.2 False color contour plots of Na (top) and Fe (bottom) on the night of 15-16 December 2000. Densities given in atoms cm^{-3}.

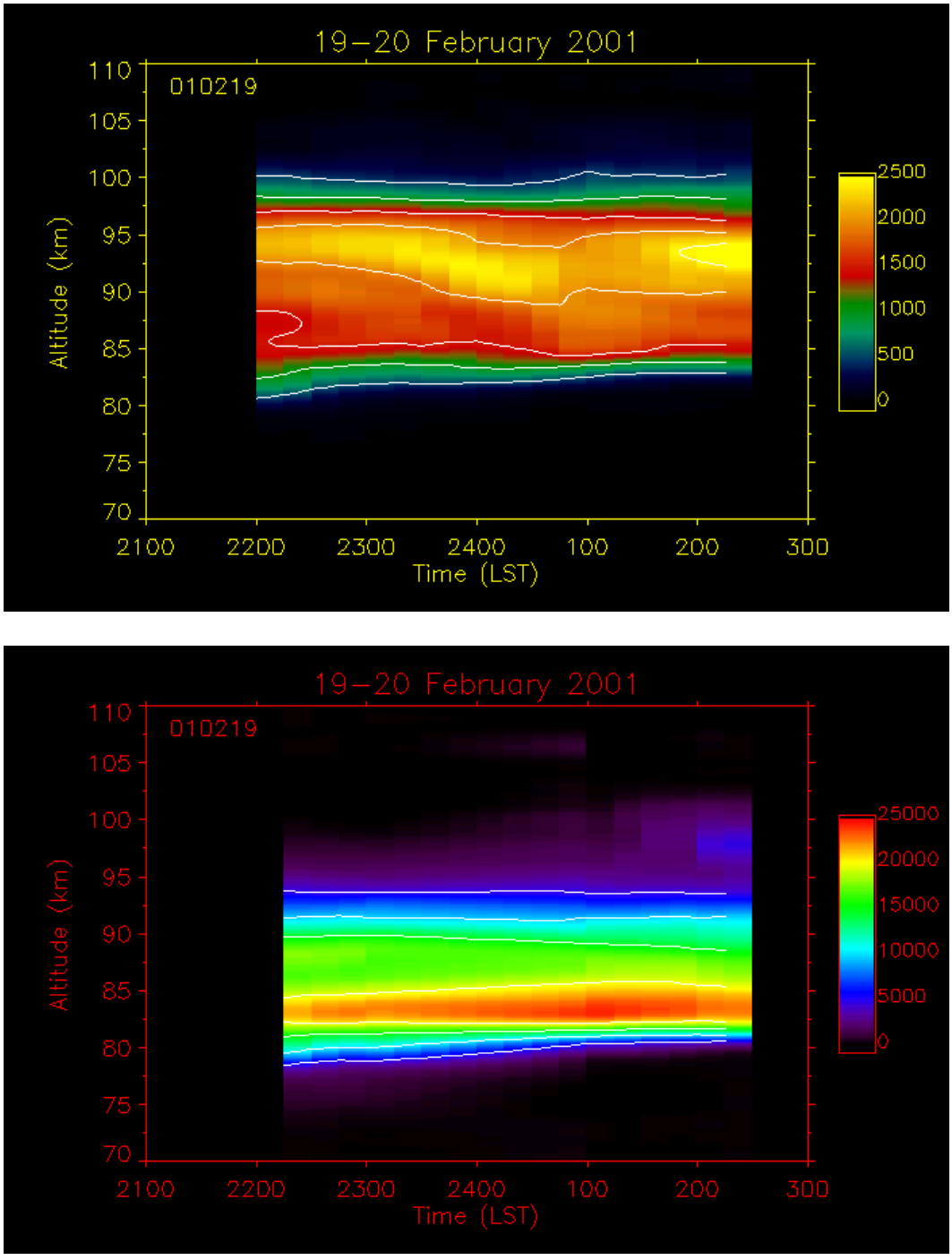

Figure A.3 False color contour plots of Na (top) and Fe (bottom) on the night of 19-20 February 2001. Densities given in atoms cm^{-3}.

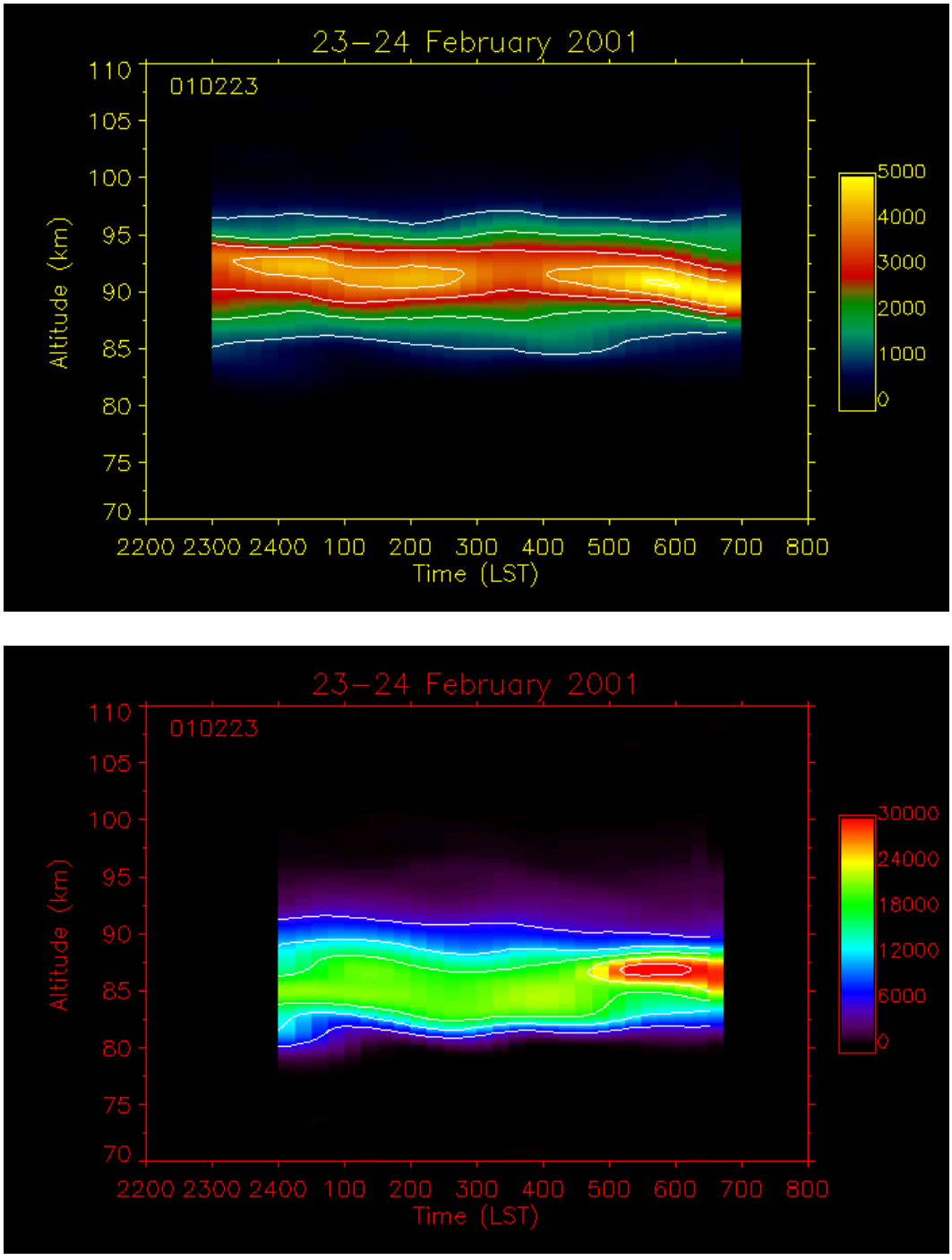

Figure A.4 False color contour plots of Na (top) and Fe (bottom) on the night of 23-24 February 2001. Densities given in atoms cm^{-3}.

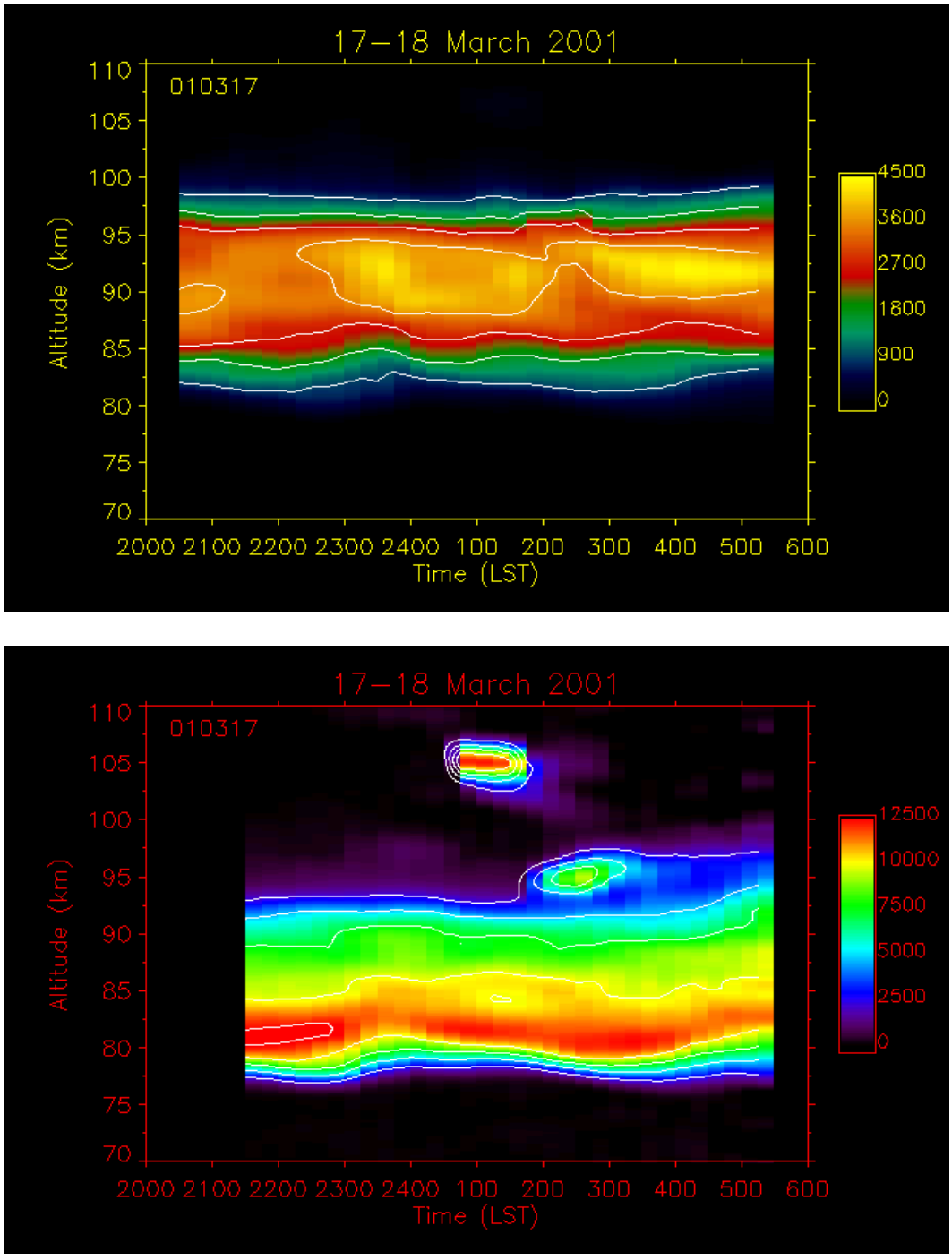

Figure A.5 False color contour plots of Na (top) and Fe (bottom) on the night of 17-18 March 2001. Densities given in atoms cm^{-3}.

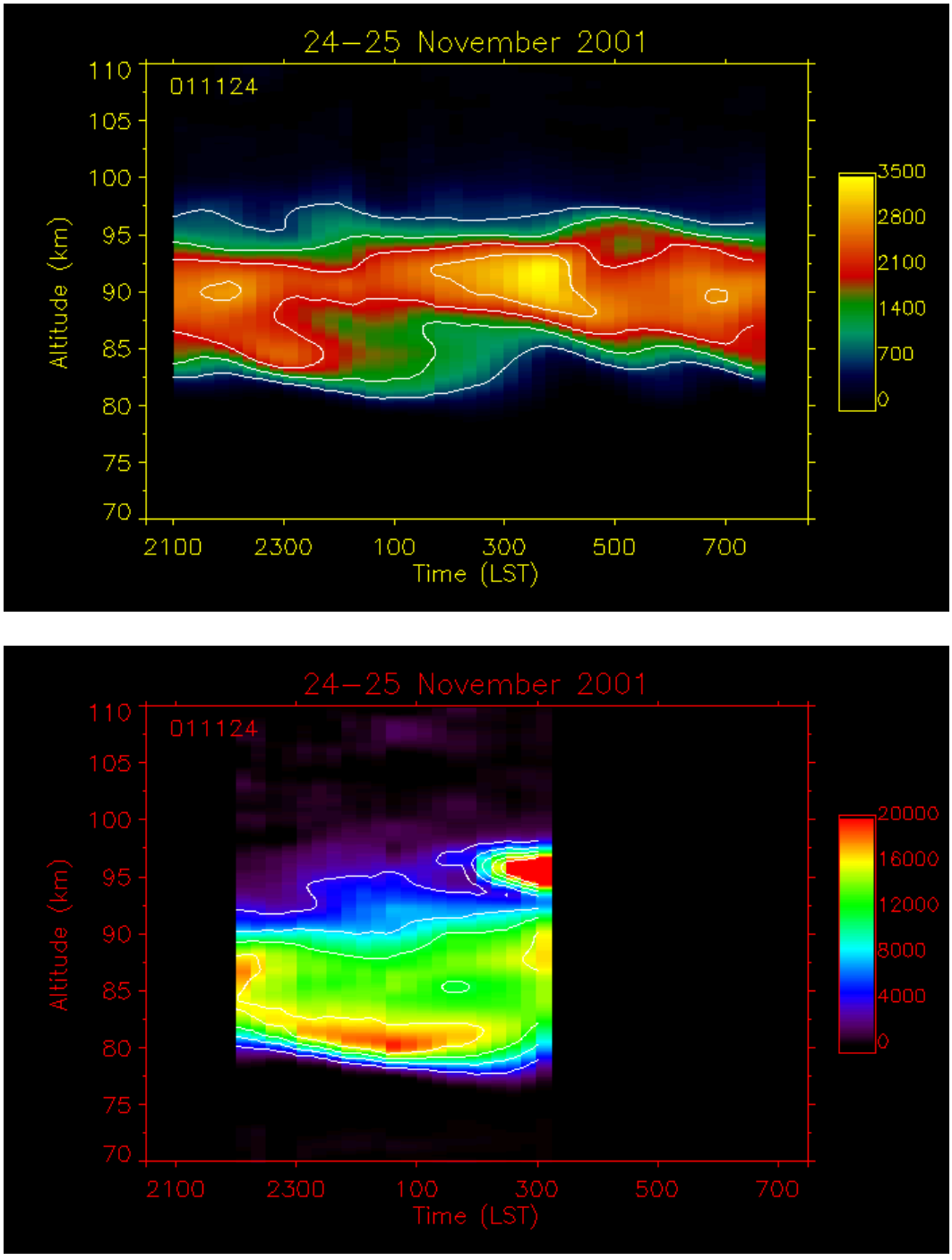

Figure A.6 False color contour plots of Na (top) and Fe (bottom) on the night of 24-25 November 2001. Densities given in atoms cm^{-3}.

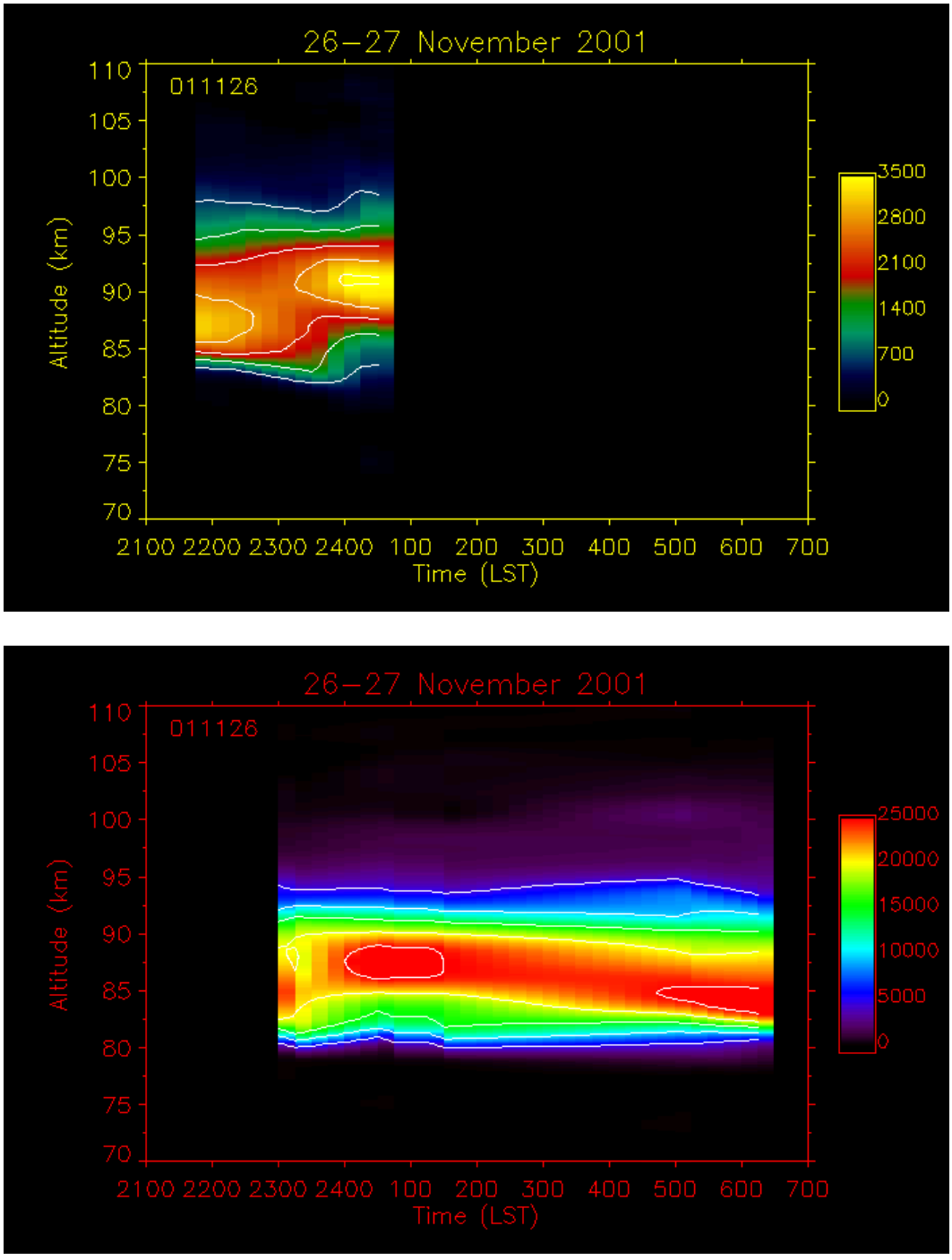

Figure A.7 False color contour plots of Na (top) and Fe (bottom) on the night of 26-27 November 2001. Densities given in atoms cm^{-3}.

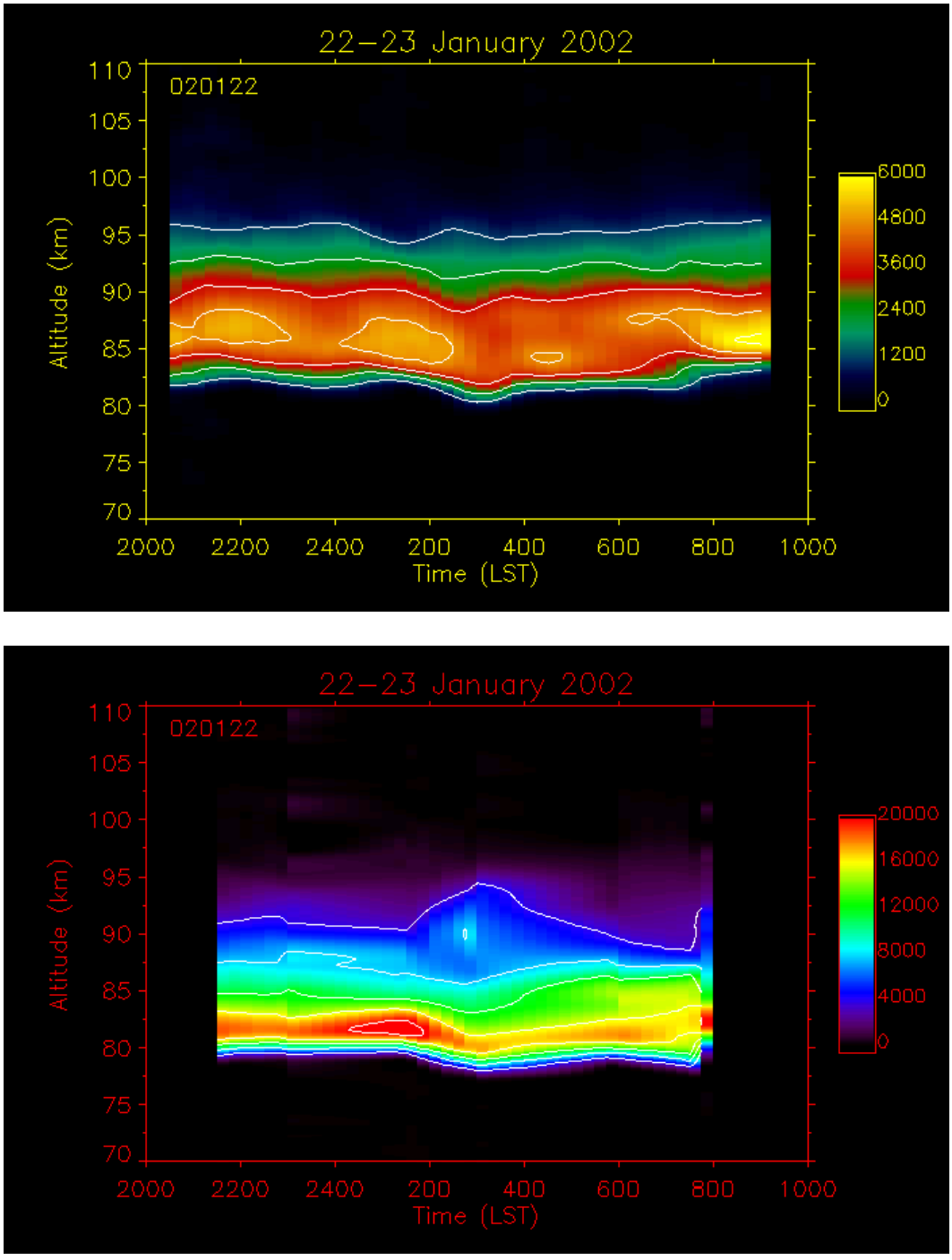

Figure A.8 False color contour plots of Na (top) and Fe (bottom) on the night of 22-23 January 2002. Densities given in atoms cm^{-3}.

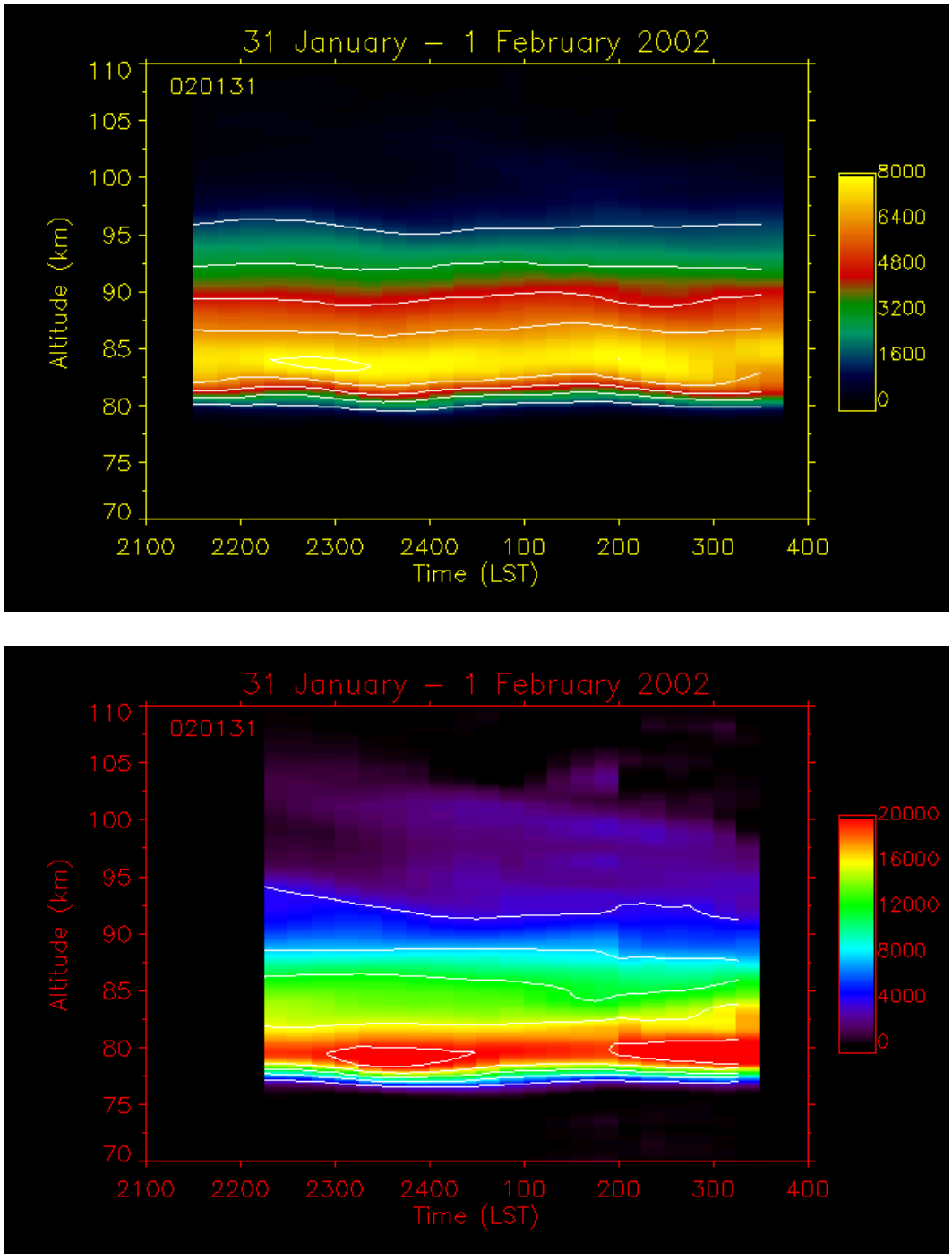

Figure A.9 False color contour plots of Na (top) and Fe (bottom) on the night of 31 January – 1 February 2002. Densities given in atoms cm^{-3}.

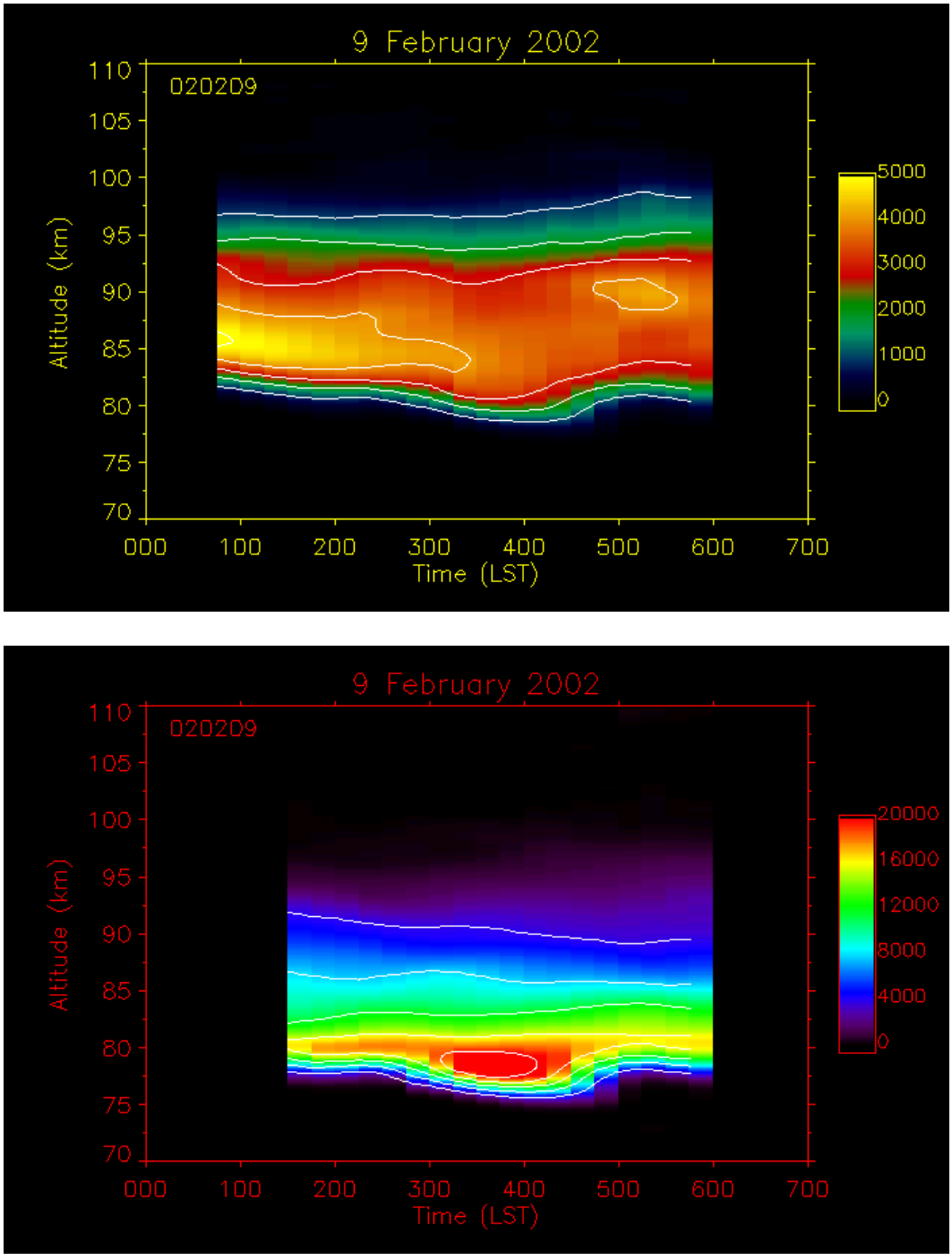

Figure A.10 False color contour plots of Na (top) and Fe (bottom) on the night of 9 February 2002. Densities given in atoms cm^{-3}.

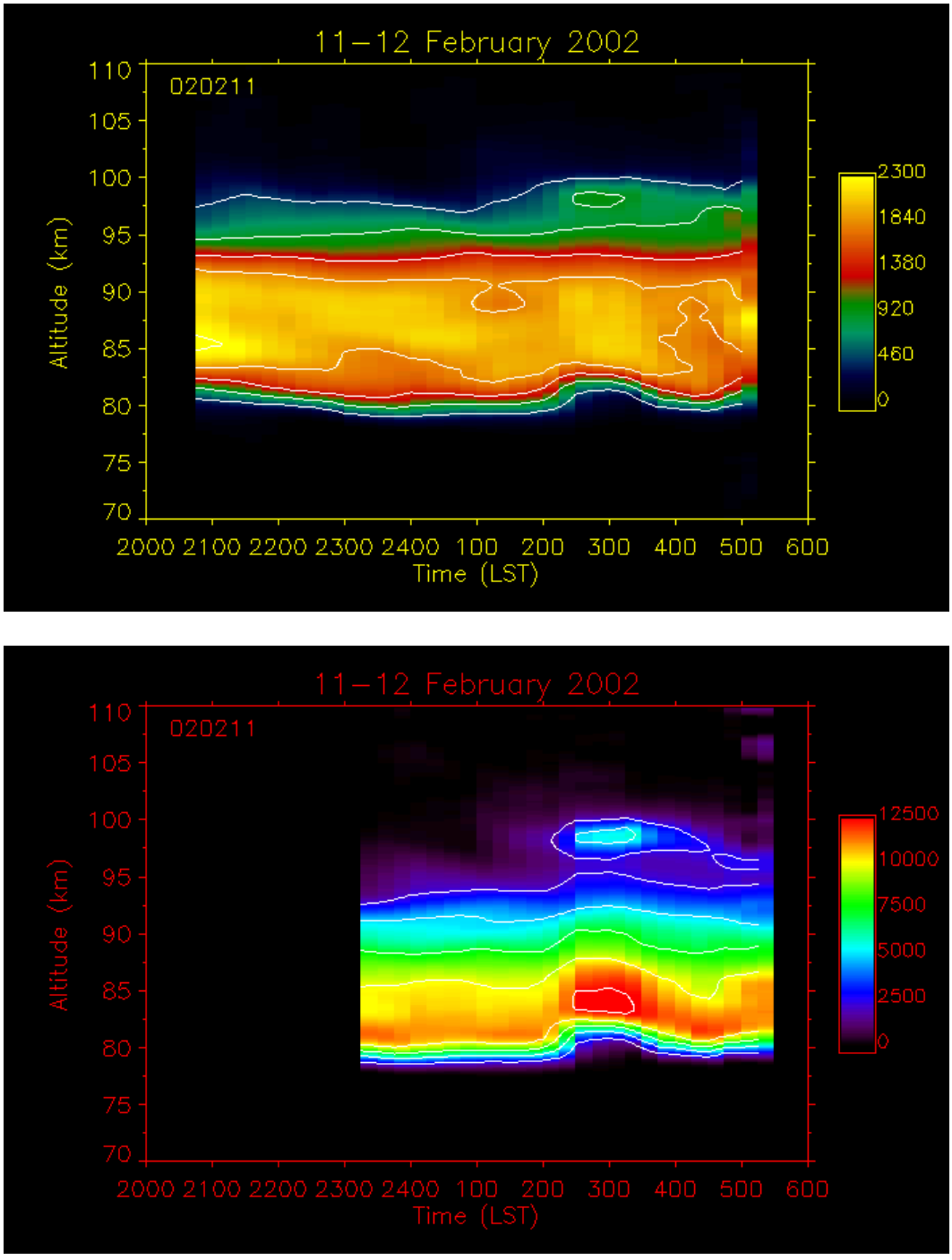

Figure A.11 False color contour plots of Na (top) and Fe (bottom) on the night of 11-12 February 2002. Densities given in atoms cm^{-3}.

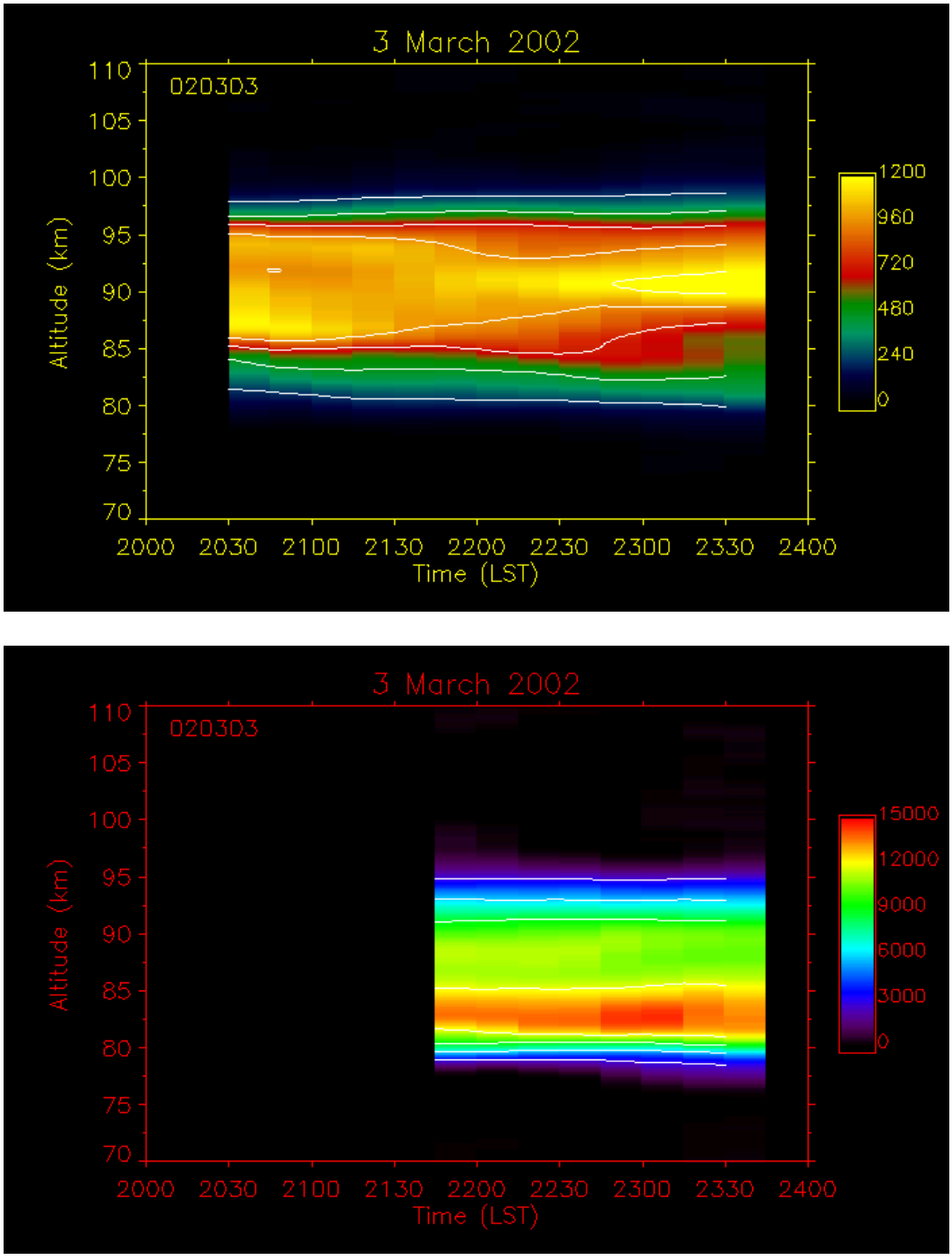

Figure A.12 False color contour plots of Na (top) and Fe (bottom) on the night of 3 March 2002. Densities given in atoms cm^{-3}.

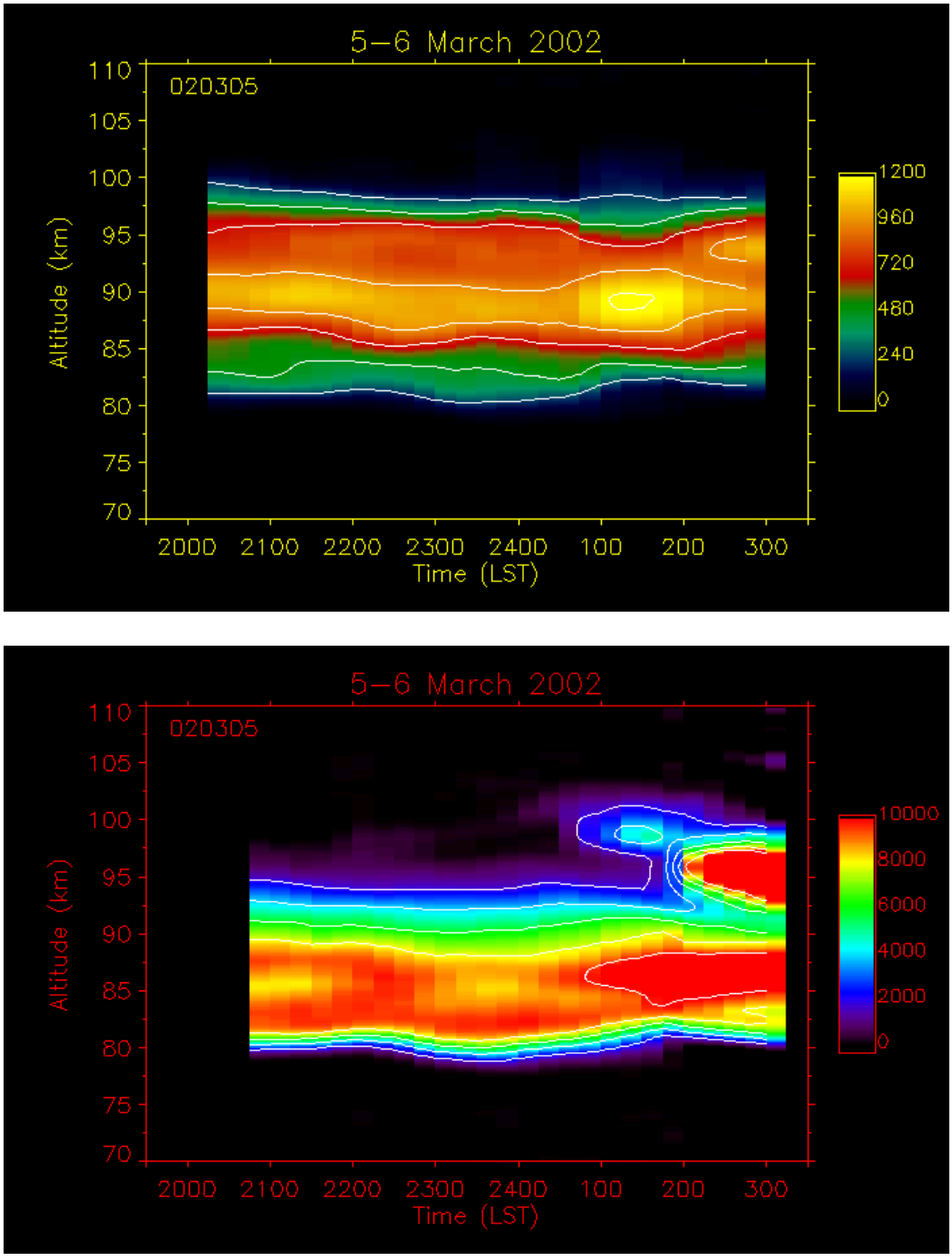

Figure A.13 False color contour plots of Na (top) and Fe (bottom) on the night of 5-6 March 2002. Densities given in atoms cm^{-3}.

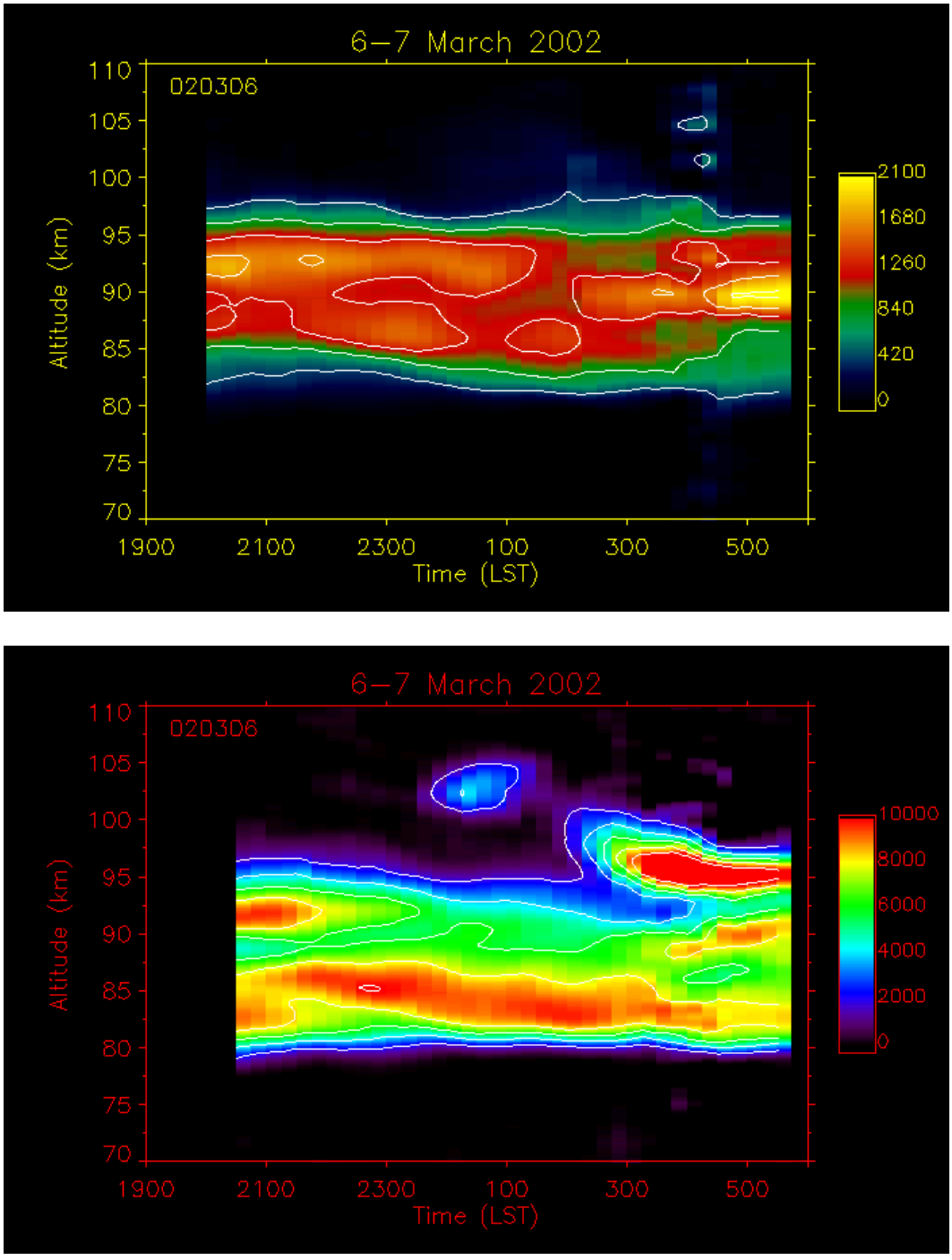

Figure A.14 False color contour plots of Na (top) and Fe (bottom) on the night of 6-7 March 2002. Densities given in atoms cm^{-3}.

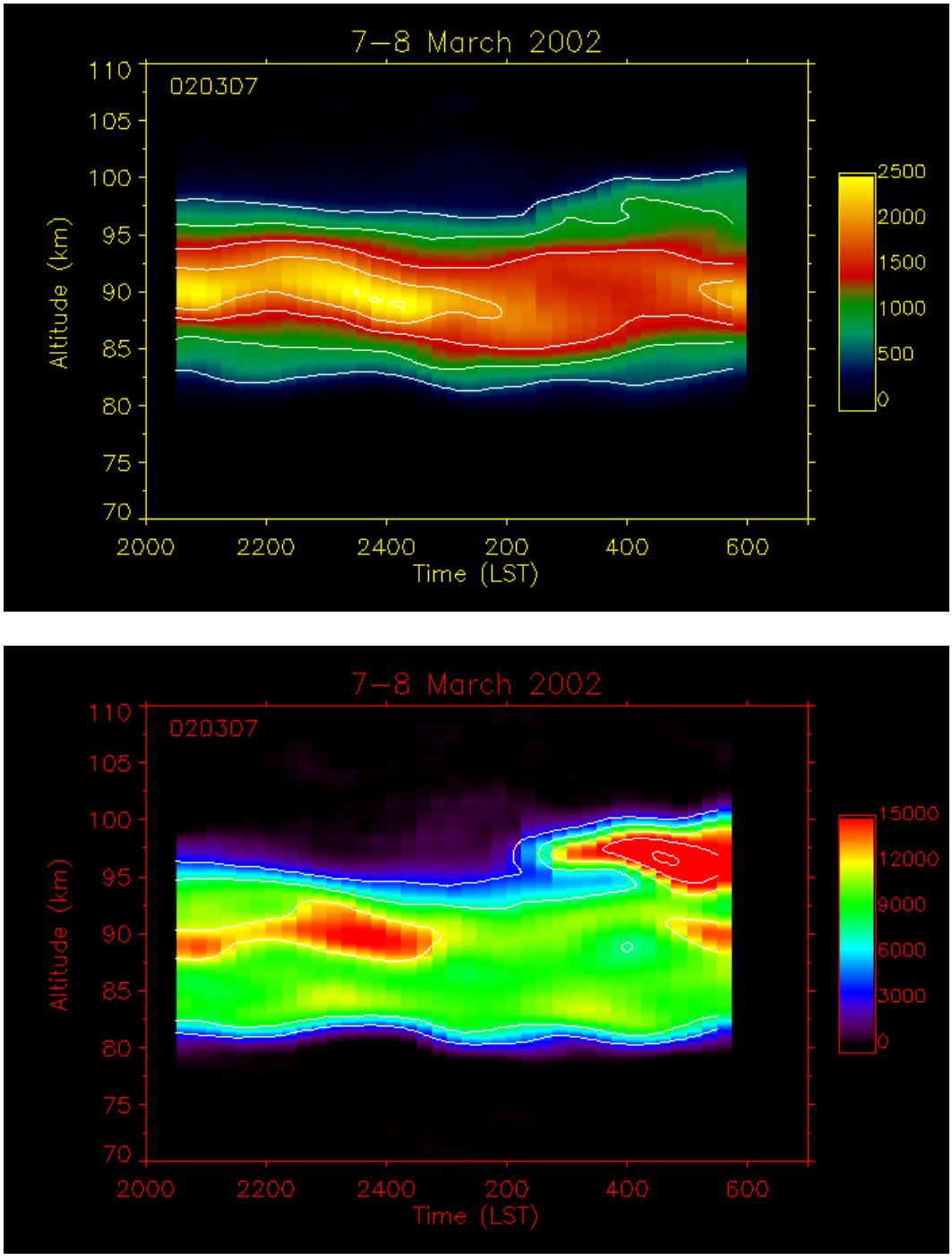

Figure A.15 False color contour plots of Na (top) and Fe (bottom) on the night of 7-8 March 2002. Densities given in atoms cm^{-3}.

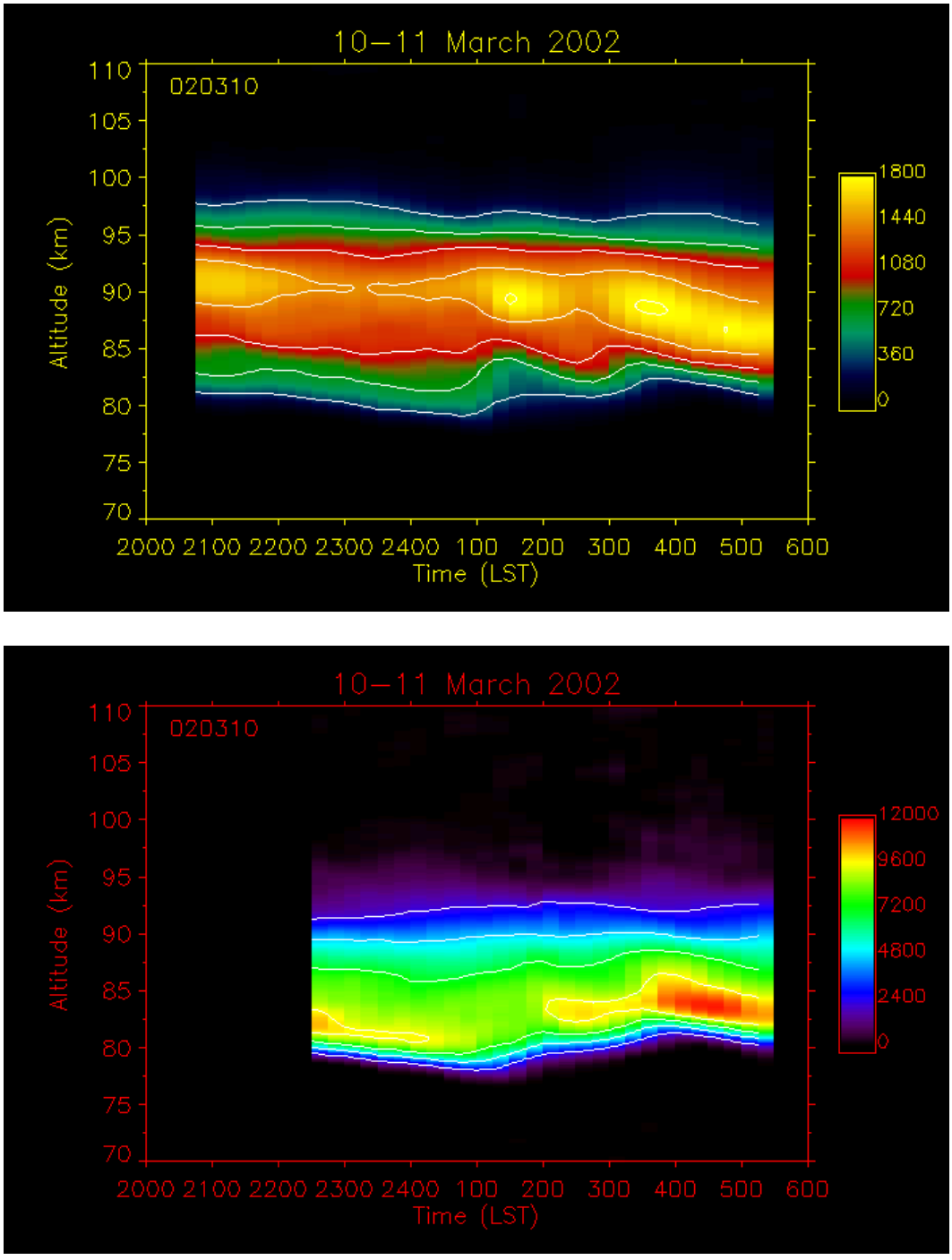

Figure A.16 False color contour plots of Na (top) and Fe (bottom) on the night of 10-11 March 2002. Densities given in atoms cm^{-3}.

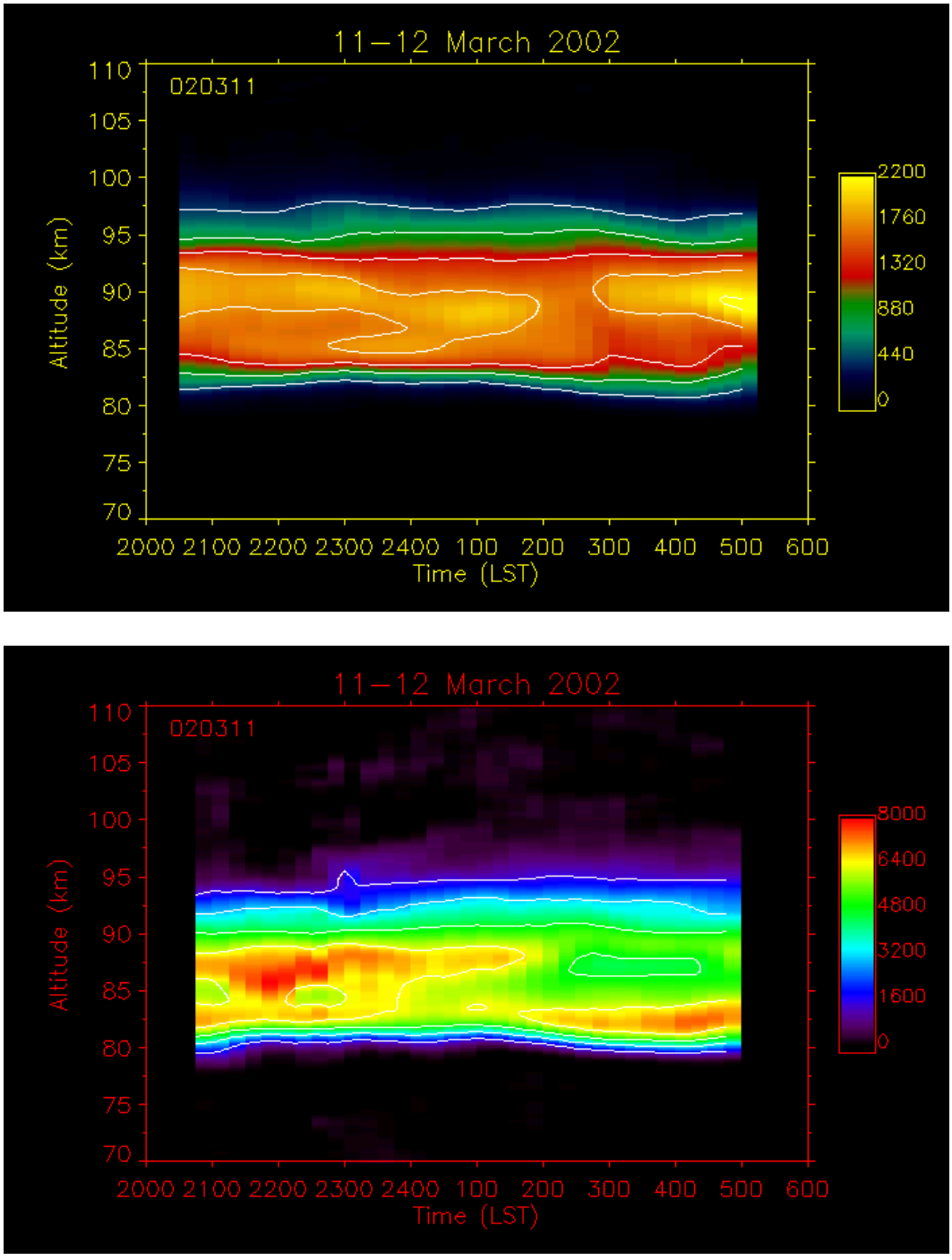

Figure A.17 False color contour plots of Na (top) and Fe (bottom) on the night of 11-12 March 2002. Densities given in atoms cm^{-3}.

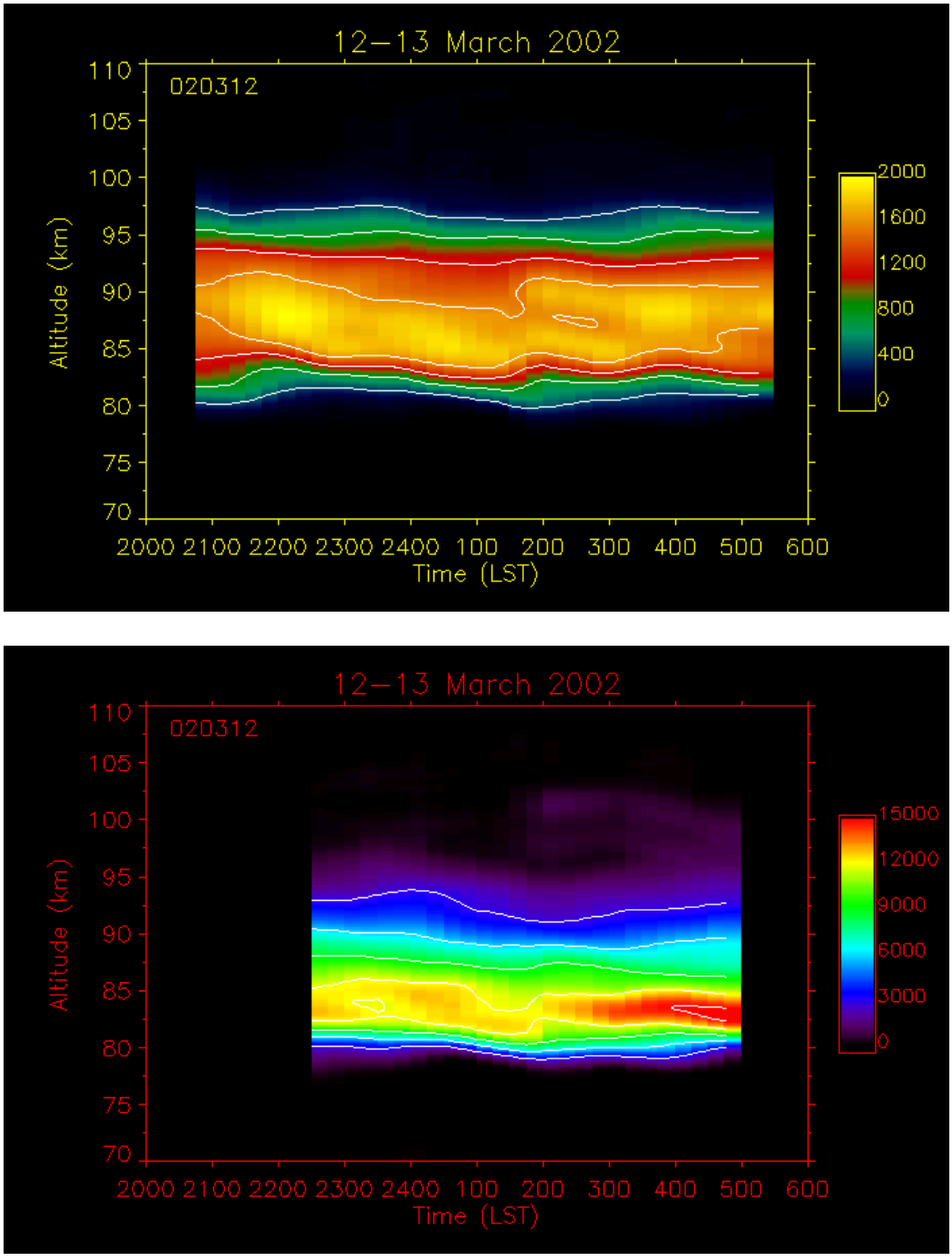

Figure A.18 False color contour plots of Na (top) and Fe (bottom) on the night of 12-13 March 2002. Densities given in atoms cm^{-3}.

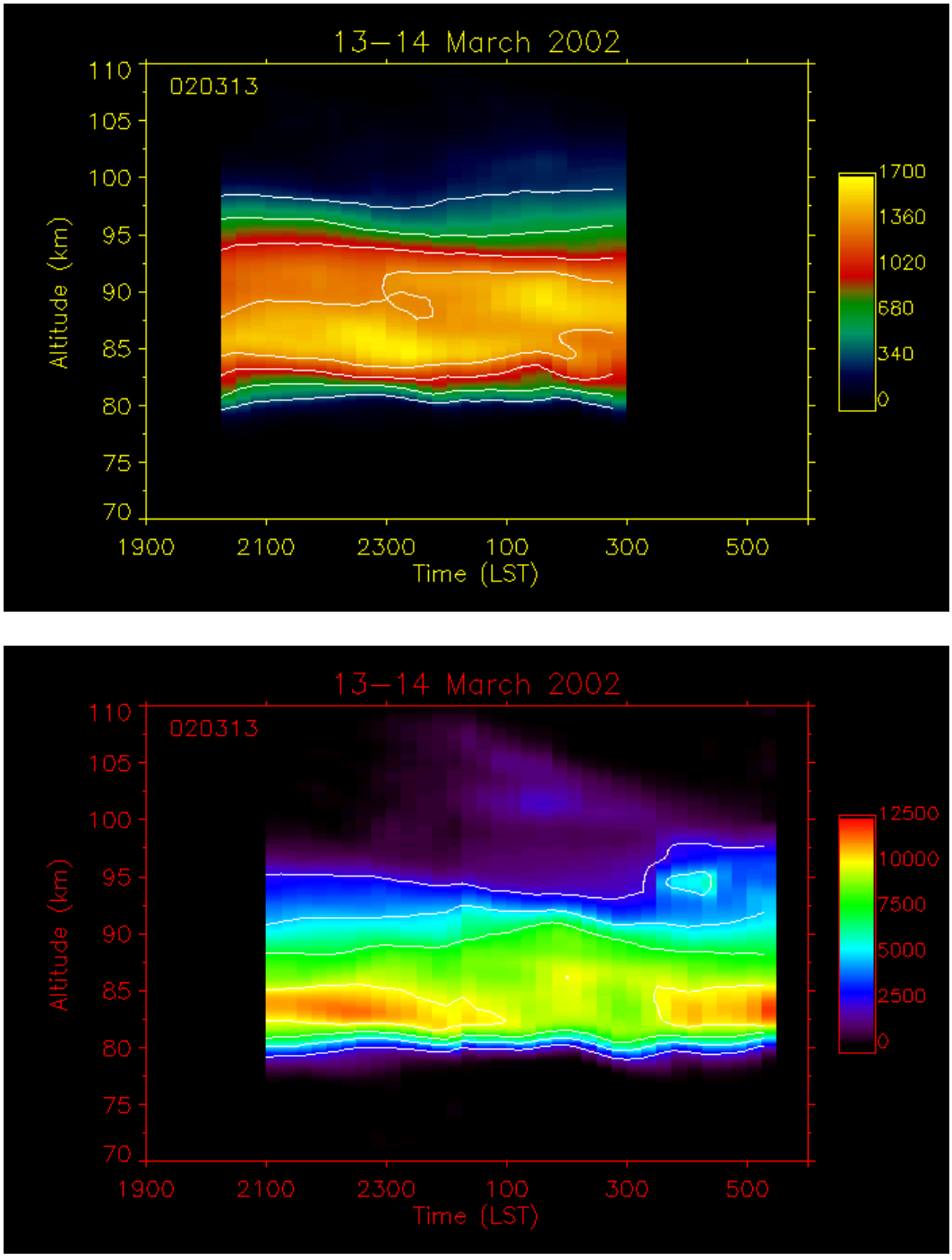

Figure A.19 False color contour plots of Na (top) and Fe (bottom) on the night of 13-14 March 2002. Densities given in atoms cm^{-3}.

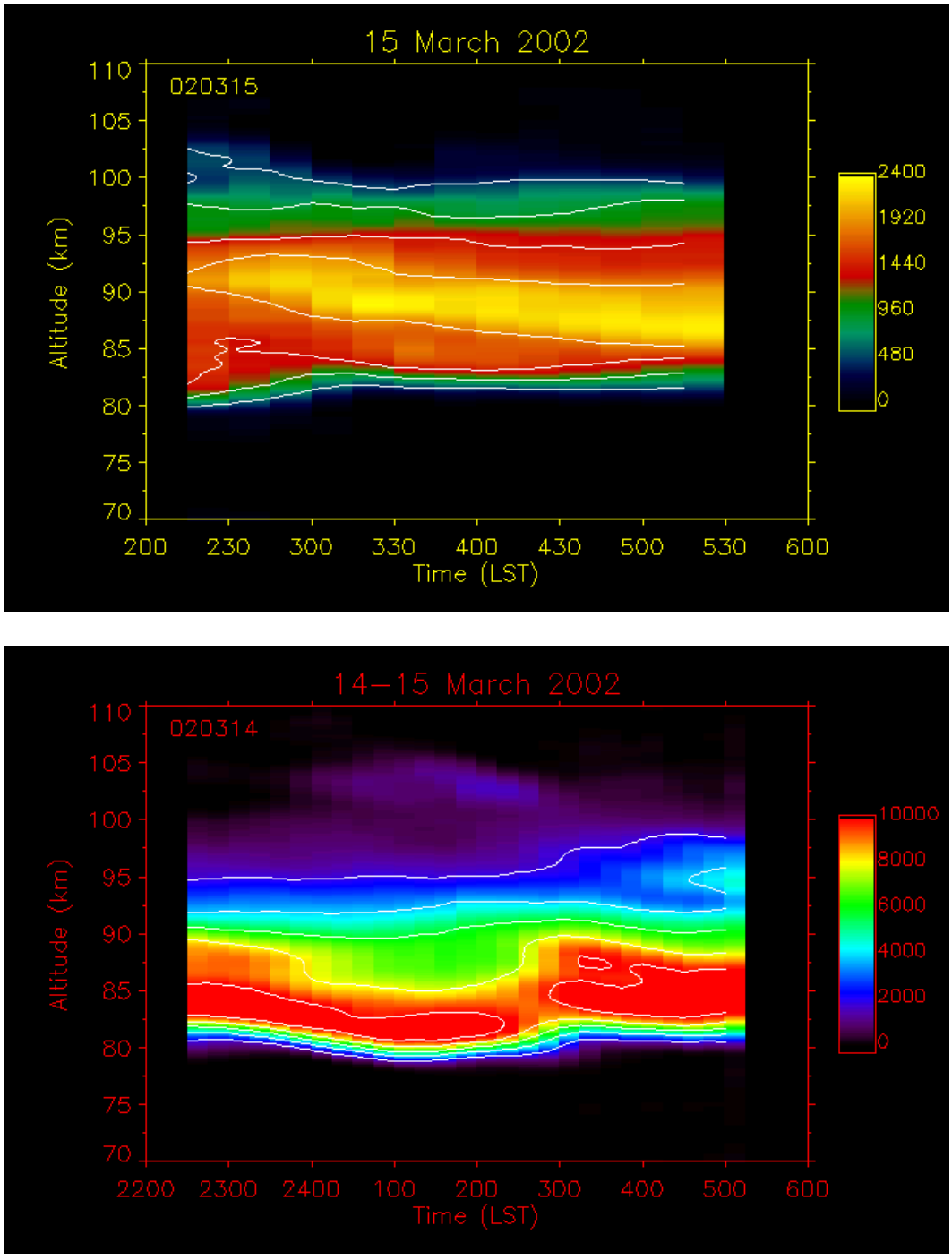

Figure A.20 False color contour plots of Na (top) and Fe (bottom) on the night of 14-15 March 2002. Densities given in atoms cm^{-3}.

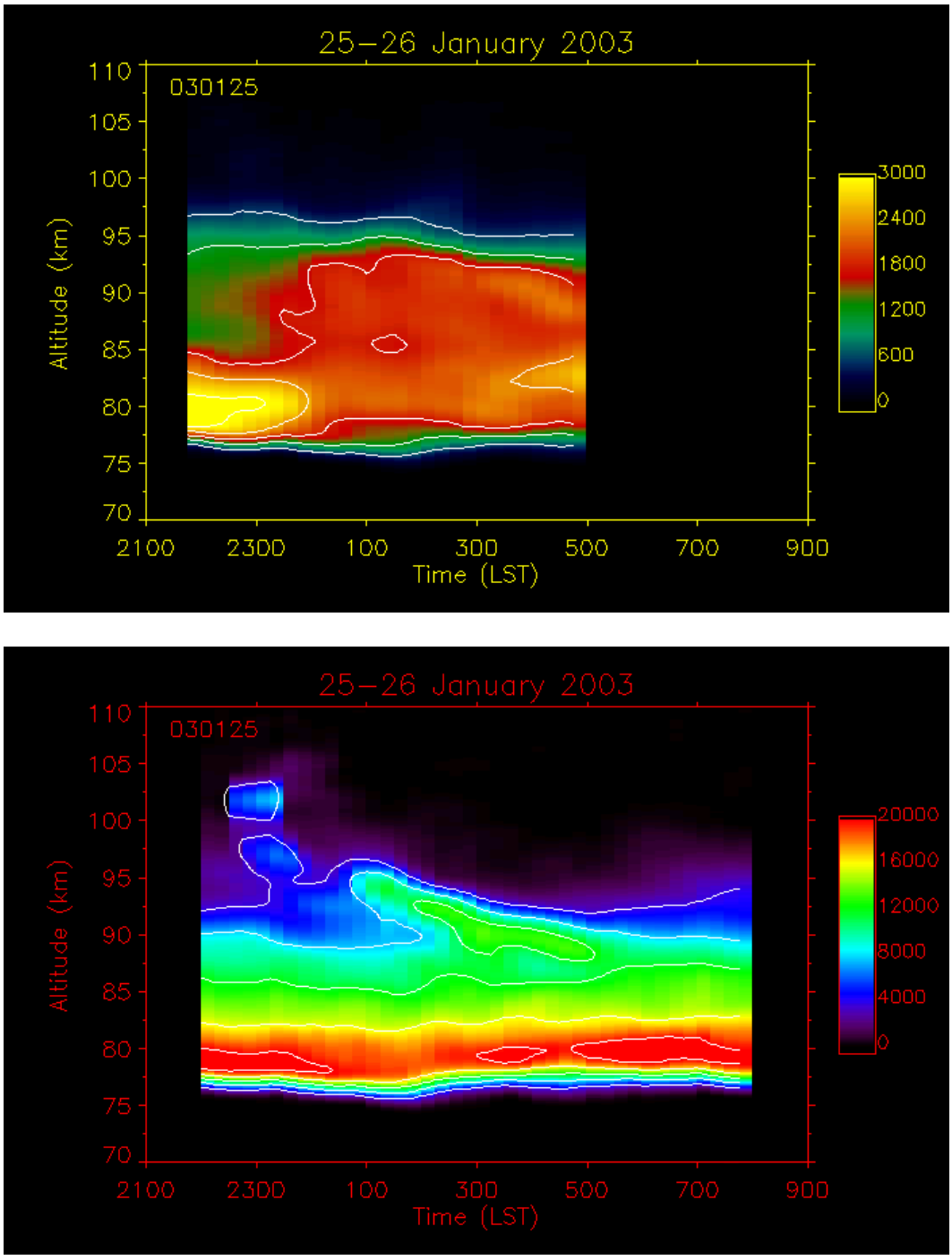

Figure A.21 False color contour plots of Na (top) and Fe (bottom) on the night of 25-26 January 2003. Densities given in atoms cm^{-3}.